Forschungszentrum Jülich

Institut für Sicherheitsforschung
und Reaktortechnik

Limit Analysis of Defects

M. Staat M. Heitzer A.-M. Yan V.D. Khoi
D.-H. Nguyen F. Voldoire A. Lahousse

Jül-3746

Limit Analysis of Defects

Manfred Staat[1] *Michael Heitzer*[2] *Ai-Min Yan*[3] *Vu Duc Khoi*[3]
Dang Hung Nguyen[3] *Francois Voldoire*[4] *Alexandre Lahousse*[4]

[1] Fachhochschule Aachen, Germany
[2] Forschungszentrum Jülich GmbH, Germany
[3] University of Liège, Belgium
[4] Electricité de France, France

Project funded by the European Commission under the Industrial & Materials Technologies Programme (Brite-EuRam III) Contract n°: BRPR-CT97-059, Project n°: BE 97-4547
Title: FEM-Based Limit and Shakedown Analysis for Design and Integrity Assessment in European Industry – LISA

Berichte des Forschungszentrums Jülich ; 3746
ISSN 0944-2952
Institut für Sicherheitsforschung und Reaktortechnik Jül-3746

Zu beziehen durch: Forschungszentrum Jülich GmbH · Zentralbibliothek
D-52425 Jülich · Bundesrepublik Deutschland
☎ 02461/61-6102 · Telefax: 02461/61-6103 · e-mail: zb-publikation@fz-juelich.de

Traglastanalyse von Defekten

von M. Staat, M. Heitzer, A.-M. Yan, V. D. Khoi, D.-H. Nguyen, F. Voldoire, A. Lahousse

Die Traglastanalyse ist eine strukturmechanische Methode, welche zunehmend in bruchmechanischen Bewertungskonzepten angewandt wird. Dieser Bericht gibt eine Einführung in die numerische Traglastanalyse in der Bruchmechanik duktiler Werkstoffe. Durch die Verbindung dieser Theorie mit Finite-Element Methoden (FEM) können Verbesserungen in der Bewertung rißbehafteter Bauteile erreicht werden. Zahlreiche Anwendungen und Beispiele zur numerischen und experimentellen Validierung werden vorgestellt.

Dieser Bericht beschreibt die neuen Konzepte, die im LISA-Projekt im Rahmen der bruchmechanischen Bewertung erzielt wurden. Das Brite-EuRam III Projekt *LISA: FEM-Based Limit and Shakedown Analysis for Design and Integrity Assessment in European Industry* zielt auf die Erweiterung und Verallgemeinerung sogenannter direkter numerischer Methoden zur Berechnung von maximal tragbaren monotonen und zyklischen Belastungen (Trag- und Einspiellasten).

Limit analysis of defects

by M. Staat, M. Heitzer, A.-M. Yan, V. D. Khoi, D.-H. Nguyen, F. Voldoire, A. Lahousse

The present report introduces the use of numerical limit analysis in ductile fracture mechanics. Limit analysis is a structural mechanics method, which finds increasing application in engineering fracture mechanics. Emphasis is put on possible improvements in the integrity assessment of crack containing components which may be achieved by combining the approach with the Finite Element Method (FEM). Several applications and examples for numerical and experimental validations are presented.

This report describes the LISA developments in connection with current practice of defect assessment and material testing. The Brite-EuRam III project *LISA: FEM-Based Limit and Shakedown Analysis for Design and Integrity Assessment in European Industry* is planned to extend and generalize the numerical methods of the so-called direct approach for the assessment of maximum load carrying capacity due to monotonic and cyclic loading (limit and shakedown load).

Contents

1 **Preface** **1**

2 **Introduction** **3**

2.1 Limit Analysis in Engineering Fracture Mechanics 4

2.1.1 Two-Criteria Assessment Method 4

2.1.2 Engineering Treatment Method (ETM) 9

2.1.3 Experimental J-integral estimation 10

2.2 Shakedown analysis 10

2.3 Economic relevance 10

3 **The concepts of limit analysis** **13**

4 **Singularity simulation for elastic-perfectly plastic fracture analysis** **15**

4.1 Double-edge cracked plate under tension (DENT) 17

5 **Numerical and experimental validation** **19**

5.1 η– factor for fracture toughness estimation for Circumferentially Cracked Round Bars (CRB) 19

5.1.1 Limit load function of CRB specimen 19

5.1.2 η–factor formulation by limit load function 20

5.1.3 Experiments using CRB specimens 22

5.2 Compact tension specimens CT25 23

5.2.1 Direct application of limit analysis 23

5.2.2 R6–method 28

6 **Benchmarks** **31**

6.1 LA3 – Plate with mis-matched weld and a centered crack under tension 32

6.2 LA4 – Axisymmetrical tube with a circumferential crack under pressure and tension 37

6.3 LA5 – Pressurized tube with a semi-elliptical flaw 39

7 **Elastic-plastic J-Integral and the failure assessment diagram (R6 FAD curve) of mis-matched welded plate** **41**

7.1 Elastic plastic J–integral and its path–independence 41

7.2 R6 Curves by elastic perfectly plastic finite element calculation 46

7.3 The load-dependence of η–factor of center cracked plate with mis-matched model 46

8 Plastic limit and safety assessment of axially cracked cylinder 51

8.1 Limit pressure of axially cracked cylinder 51

8.2 R6 curve of axially cracked cylinder under pressure 55

8.3 R6 curve of axially cracked cylinder under pressure and radial temperature gradient 56

9 Conclusions 61

References 63

A Appendix: The singularity of strain singular elements A 1

B Appendix: Analytical lower bound for benchmark LA4 B 1

List of Figures

2.1 FAD curves for revisions 2 and 3 of R6 method 8

4.1 (a) Isoparametric degenerated element; (b) Parent element (c) Model proposed in [12]: quarter-point degenerated element 16

4.2 Finite element meshing of type C 17

4.3 Crack tip and von Mises field in plastic limit state 17

4.6 Plastic limit of DENT specimen (note: $\alpha = \bar{\sigma}_c/\sigma_y$ where $\bar{\sigma}_c$ is mean limit stress in net section 2c; PS-Plane stress; PD-Plane strain; T-Tresca; M-von Mises criterion) 18

5.1 Circumferentially-cracked round bar (CRB) under tension (L=55mm, R=5mm) 19

5.2 Non-dimensional limit load of CRB specimen, (triaxiality factor) $\left(\alpha_l = \frac{F_l}{\pi b^2 \sigma_y}\right)$ 20

5.3 η–factor derived from limit load function 22

5.4 FE-model dimensions similar to CT25 specimens in $[mm]$ (see [52]) 24

5.5 FEM meshes for the different 2D and 3D models 26

5.6 Comparison of limit loads of CT3D1 calculated by LISA with analytical solutions and the experiments AB15, AC18, AC19, AC20 (from [52]) 27

5.7 Comparison of FAD Rev. 2 and FAD Rev. 3 Opt. 1 (2.13), (2.15) 28

6.1 FE mesh of benchmark LA3 32

6.2 Comparison of numerical and analytical results (eq. (6.2) of limit load for different crack length and mismatch factors $M = \sigma_y^W/\sigma_y^B$ for plane stress, $h/W = 0.3$ 34

6.3 Comparison of numerical and analytical results for different values of weld thickness, mismatch factors $M = \sigma_y^W/\sigma_y^B$, and crack lengths factors a/W, plane stress. 35

6.4 Yield contour line for overmatched material case $\sigma_y^W/\sigma_y^B = 1.5$, [26] 36

6.5 Yield contour line for undermatched material case $\sigma_y^W/\sigma_y^B = 0.75$, [26] 36

6.6 FE–mesh and dimensions of LA4 37

6.7 FE mesh of benchmark LA5 39

7.1 a) Path independence of J (loading up to 30% of limit load) 42

7.1 b) Path independence of J (last loading steps at nearly limit load) 43

7.2 Maximum relative difference Δ of J integral on contours in all loading levels (homogeneous material $\sigma_y^W/\sigma_y^B = 1$) 43

7.3 Maximum relative difference Δ of J integral on contours in all loading levels (undermatched material $\sigma_y^W/\sigma_y^B = 0.5$) 44

7.4 Maximum relative difference Δ of J integral on contours in all loading levels (overmatched material $\sigma_y^W/\sigma_y^B = 1.5$) 44

7.5 Integral J as function of load level (CCP-Plane stress state) 45

7.6 Integral J as function of load level (CCP-Plane strain state) 45

7.7 FAD of CCP specimen with different material models, for hardening material taken from [36], $M = 1$ 47

7.8 FAD of CCP specimen in plane stress or plane strain, curves for hardening material taken from [36], $M = 1$ 47

7.9 FAD of CCP weld plate (plane stress)- mismatched material model 48

7.10 FAD of CCP weld plate (plane strain)- mismatched material model 48

7.11 η_{pl} factor as function of loading level (homogeneous material $M = \sigma_y^W/\sigma_y^B = 1$) 49

7.12 η_{pl} factor as function of loading level (undermatched model: $M = \sigma_y^W/\sigma_y^B = 0.5$) 50

7.13 η_{pl} factor as function of loading level (overmatched model: $M = \sigma_y^W/\sigma_y^B = 1.5$) 50

8.1 Assumed plastic slip mechanism of axially cracked cylinder under internal pressure 51

8.2 Slip angle of axially cracked cylinder under internal pressure 52

8.3 Finite element meshing and fictitious von Mises stress field in limit state (σ_{eq}/σ_y) (direct upper bound analysis) 54

8.4 Finite element meshing and fictitious von Mises strain field in limit state ($\varepsilon_{eq}/\varepsilon_y$) (incremental elastic-perfectly plastic analysis) 54

8.5 Limit pressure of axially-cracked cylinder ($R_0/R_i = 1.2$) 55

8.6 Independence of contour of J (axially cracked cylinder under pressure) 56

8.7 Maximum relative difference Δ of J integral on contours (axially cracked cylinder) 57

8.8 R6 curve of axially cracked cylinder under internal pressure (similar results are obtained for two material) 57

8.9 R6 curve of axially cracked cylinder under internal pressure and thermal loading ($R_i = 50mm, R_0 = 60mm, a = 4mm. \sigma_y = 200$ Mpa, $E = 2.1 \times 10^5$ Mpa, $\nu = 0.3$, $\alpha_t = 1.2 \times 10^{-5}/K$) 58

8.10 Plastic interaction parameter of axially cracked cylinder under internal pressure and thermal loading (temperature difference along thickness) 59

8.11 The values of ρ_1 for the defining K_r^s 60

B1 Statical approach for the LA4 test . . . . B 1

B2 Comparison of (F, P) curves for the LA4 test, analytical solution by F.Voldoire. . . . . . . B 3

B3 Collapse mode for the La4 test in pure tension (limit analysis computation with Code_Aster®). B 3

List of Tables

4.1 Comparison of limit load solutions with different crack-tip elements 18

5.1 Limit load of CRB specimen by ELSA 20

5.2 Material data of CRB specimens at ambient temperature [49]. 23

5.3 Results of limit analyses for different FEM-models and experiments computed from $F_{exp.}/F_f$ in [49]. 23

5.4 η–factor from experiments and from limit analysis [49]. 23

5.5 Material data of CT25 specimens [52], [53] at $80\,^\circ C$ 24

5.6 Results of limit analyses for different FEM-models and experiments 27

5.7 Comparison of analytical limit loads with numerical results of limit analyses for specimens $B = 20$, without side grooves with $R_m = 513N/mm^2$ instead of $R_{p0.2} = 379N/mm^2$ and $\sigma_f = 446N/mm^2$ 27

6.1 Comparison of limit loads (in N/mm^2) for LA3 34

6.2 Comparison of limit analysis results (in N/mm^2) for LA4 38

6.3 Comparison of collapse pressures (in N/mm^2) for LA5 40

7.1 Limit load solution of mis-matched welded plate (plane strain) $(a/W = 0.5)$ 42

8.1 Comparison of limit pressure and slip angle, $a/h = 0.4$ 53

Abbreviations and Nomenclature

2D, 3D	Two-dimensional, three-dimensional
ASTM	American Society for Testing and Materials, Philadelphia, USA
CDF	Crack Driving Force
CEGB	Central Electricity Generating Board, UK
Code_Aster®	FEM software by EDF, France
CRB	Circumferentially Cracked Round Bar
CT	Compact Tension specimen
CTOD	Crack Tip Opening Displacement
DENT	Double–Edge Notched Tension specimen
DOFs	Degrees of Freedoms
EDF	Electricité de France
EDI	Equivalent Domain Integral
ELSA	FEM based LISA software by ULg, Belgium
EPRI	Electric Power Research Institute, USA
ETM	Engineering Treatment Method
FAD	Failure Assessment Diagram
FEM	Finite Element Method
FZJ	Forschungszentrum Jülich GmbH
GKSS	GKSS-Foschungszentrum Geesthacht
HRR	Hutchinson-Rice-Rosengren plastic stress field
INTES	Ingenieurgesellschaft für technische Software mbH, Stuttgart
LA3, LA4, La5	Limit analysis test cases in the benchmark
LCF	Low Cycle Fatigue
LISA	Limit and Shakedown Analysis, acronym of the Brite-EuRam project BE 97-4547, and of its software
NDT	Non Destructive Testing
NRB	circumferentially-Notched Round Bar
PERMAS	FEM software by INTES, Stuttgart, Germany
R6	Two-Criteria Assessment Method
SAMCEF	FEM software by SAMTECH, Liège, Belgium
SIF	Stress Intensity Factor
SINTAP	Structural Integrity Assessment Procedures for European Industry, Brite-EuRam project BE95-1426
SQP	Sequential Quadratic Programming
ULg	University of Liège
V4, V7	PERMAS Version 4, Version 7
VCE	Virtual Crack Extension

$a, 2a$	Crack length
A_g	total elongation at R_m
A_5	total elongation at rupture
$\mathbf{b}, \mathbf{b}_0$	body force
E	Young's modulus
f_{R6}	R6 failure assessment curve
F	Applied load
F_f, F_u, F_y	Limit loads for $\sigma_f, \sigma_u, \sigma_y$
J	J-integral, Rice integral
J_{Ic}	Critical J-value according to ASTM E-813
$J_{0.2}$	J-value at $0.2mm$ crack extension (blunting initiation)
K_I	SIF for mode I fracture
K_{Ic}	Fracture toughness according to ASTM E-399
K_{Ieff}	Plasticity corrected SIF
K_r	Fracture parameter
L	Plastic constraint factor
L_r	Limit load parameter for F_y
$\mathcal{L}$	Load domain
$\mathbf{n}, n_i$	Outer normal vector
N, n	Strain-hardening exponent
M	Mis-match factor
$\mathbf{p}, \mathbf{p}_0$	Surface traction
R_{eL}	Lower yield strength
R_m	Ultimate strength
$R_{p0.2}$	0.2% Plastic elongation stress
S_m	Allowable design stress
S_r	Limit load parameter for F_f
$V, \partial V$	Structure and its boundary
$\dot{U}_{pl}$	Dissipated plastic strain energy
$\dot{W}_{ex}$	External power of loading
$\dot{W}_{in}$	Internally dissipated energy
Y	Quantity at incipient (net section) yielding
Z	area reduction at rupture
α	Limit load factor
α_t	Thermal expansion coefficient
δ	COTD
δ_5	COTD defined for a gauge length of 5mm
δ_{pl}	plastic part of load point displacement
κ	Loading direction parameter
$\boldsymbol{\varepsilon}, \varepsilon_{ij}$	Actual strain
Φ	Yield function
ν	Poisson's constant
η	η-factor
η_{el}, η_{pl}	Elastic, plastic η-factor
ρ	Parameter for plastic interaction between primary and secondary stress
$\boldsymbol{\sigma}, \sigma_{ij}$	Actual stress, stress tensor
σ_f	flow stress
σ^p, σ^s	Primary, secondary stress
σ_u	Ultimate tensile strength, R_m
σ_y	Yield strength, R_{eL} or R_{p02}
σ_y^B, σ_y^W	Yield strength of base and weld material

1 Preface

The present report introduces the use of limit analysis in ductile fracture mechanics. Limit analysis is a structural mechanics method, which finds increasing application in engineering fracture mechanics. Emphasis is put on examples demonstrating possible improvements which may be achieved by combining the approach with the Finite Element Method (FEM).

This report describes the LISA developments in connection with current practice of defect assessment and material testing. The new SINTAP procedures for materials with yield plateau and the new V-factor route in R6 code for treatment of secondary stresses are not considered. The LISA project is planned to extend and generalize the numerical methods of the so-called direct approach. This first LISA report does not express final conclusions, but it discusses what could be achieved through improved limit analyses. It is expected that more evidence for better advise to the engineering community will be obtained in the course of the present research.

The report was edited by M. Staat, who wrote with M. Heitzer Sections 1, 2, 3, 5.2, 6, and 9. A.M. Yan, V.D. Khoi and D.H. Nguyen are responsible for Sections 4, 5.1.1, 5.1.2, 7, 8, and Appendix A. F. Voldoire developed Appendix B. All authors provided input to Section 6 among others. INTES, Stuttgart, performed some incremental FEM analyses for Section 6. Some of the considered problem cases have been suggested by R.A. Ainsworth (British Energy formerly Nuclear Electric) from the view of the Brite-EuRam project SINTAP (Project N°: BE95-1426, Contract N°: BRPR-CT95-0024).

The editor has revised the report introducing minor corrections, extensions and the additional Section 5.1.3. At the time of the revision the SINTAP background documentation was available on a CD-ROM. However, no effort was made to introduce all the SINTAP achievements.

Acknowledgement: The research was performed for the European Commission as part of the Brite-EuRam III project LISA: FEM-Based Limit and Shakedown Analysis for Design and Integrity Assessment in European Industry (Project N°: BE 97-4547, Contract N°: BRPR-CT97-0595).

2 Introduction

Limit analysis as a structural mechanics tool has become indispensable for the engineering approach to ductile fracture mechanics. Limit analysis is either used directly for assessment purpose or in connection with some fracture mechanics concept in order to cover all possible failure modes of crack-like defects. Such defects have three (major) adverse effects on structural integrity:

- They reduce the load carrying structural section to the so-called ligament.
- They constrain deformation thus increasing stress triaxiality.
- Generally they generate additional bending stress.
- They are local stress raisers (stress singularity in elasticity).

The last effect is considered by fracture mechanics concepts like stress intensity factor (SIF). But the effect is limited by plastic yielding. For ductile material only the three other effects persist and may be treated by limit analysis.

Two-Criteria Assessment Methods consider the possibility of failure of a structure through two mechanisms: brittle fracture, crack-tip controlled by SIF reaching the material's fracture toughness value and plastic collapse at limit load. Two-Criteria Assessment Methods are widely used in design codes and assessment rules for metallic structures (pressure vessels and piping, steel structures). The Engineering Treatment Method (ETM) uses limit analysis to extent fracture mechanics concepts like J-integral or Crack Tip Opening Displacement (CTOD) beyond their conceptual limits into the fully plastic domain. If the material behaves sufficiently ductile limit analysis alone may give the correct answer, because the crack may fail by plastic collapse of the remaining ligament. The American Society for Testing and Materials (ASTM) suggests J-integral estimation formulae that use the limit loads of ASTM standard test specimens.

Todays engineering fracture mechanics has a strong practical, economic and safety need for limit loads of standard crack configurations. Collections of available limit loads have been compiled in [9], [10], [11], [37], [36], [39], [46], [47], [72], and Appendix F of [1] (to be replaced by [5]). It is good practice, that most documents provide SIFs and limit loads at the same time. The following may be observed:

- Limit analysis is applicable in a way similar to SIFs.
- Material strength data for limit analysis is generally available for engineering materials, whereas fracture mechanics data must be obtained from specialized testing (which is often impossible because of the required size of test specimens).
- The fracture mechanics concepts (SIF, J-integral or CTOD) have the problem of transferability of fracture properties from test specimen to component.
- Limit loads are often given in a more restricted parameter range and some are less reliable as compared to SIFs.
- Classical fracture mechanics concepts are not directly applicable to interface cracks but limit analysis applies without changes.
- There are more solutions for SIFs than for limit loads (except for the weld mis-match problem).

- Limit loads are often given as simple functions of the relevant parameters, which provides direct information for engineering decision.
- The application of limit analysis seems to be not always straight forward with respect to material hardening and secondary stress.

Among others the following fracture mechanics computer programs contain SIFs and limit load solutions:

Deterministic fracture assessment: R6-Code by British Energy (formely Nuclear Electric and CEGB, UK) [3], CrackWise by The Welding Institute (TWI, UK), SACC by Det Norske Veritas (DNV) Sweden (formerly The Swedish Plant Inspectorate (SAQ)) [15], and PREFIS for the petrochemical industry.

Probabilistic fracture mechanics: PARIS, ZERBERUS by Forschungszentrum Karlsruhe (Germany) [17], [21], CRACKS by Forschungszentrum Jülich (Germany) [57], and PC-PRAISE by Lawrence Livermore National Lab. (CA, USA) [25], ProSINTAP by DNV Sweden.

Limit loads have been obtained by:

Analytical methods: For plane strain the plasticity boundary value problem is decribed by hyperbolic partial differential equations. Their characteristics are slip lines. Upper bound values for plastic collapse loads of specimens can be obtained by finding the slip-line field pattern which minimises the amount of energy dissipated along the loading path. In plane stress it is easier to suggest stress fields at collpase for lower bound analysis.

Numerical methods: The Finite Element Method (FEM) is particularly well suited for limit analyses. It is the objective of the present project to make it available for direct analyses of complex problems of crack-containing structures.

Experimental methods: Some limit load solution have been obtained as a fit to experimental collapse loads of defect structures. These solutions include the effect of hardening and possibly some crack-tip influences. They may not yield realistic limit loads in the regime of strong SIF influence.

The present report shows how limit loads for arbitrary crack configurations may be obtained from limit analyses based on Finite Element Methods (FEM). This is the most appropriate approach to overcome all the above problems observed for limit loads of cracks. Limit loads are compared to experiments, analytical solutions and alternative methods. Application in connection with the R6-Method in engineering fracture mechanics is performed for some examples.

2.1 Limit Analysis in Engineering Fracture Mechanics

2.1.1 Two-Criteria Assessment Method

The R6-Method is a Two-Criteria Assessment Method for the integrity assessment of structures containing defects [4]. It is internationally accepted by industry and inspection authorities [11]. It is used in NDT based flaw assessment (CEC Study Contract RA1-0115-I, [18]), in probabilistic Leak-Before-Break (LBB) analyses [57], and is adopted for British Standards Institute PD6493 [1]. In principle the method can be used for all metallic materials. It is, however, more extensively verified for steel alloys only. It is not intended for use in temperature regions where creep deformation is of importance. Similar methods have been developed in the USA [36].

The basic assumption of the R6-Method is, that fracture initiated by a crack can be described by the variables fracture parameter (proximity to brittle fracture parameter) K_r and limit load parameter (proximity to plastic collapse parameter) L_r, defined by

$$K_r = \frac{\text{SIF resulting from primary and secondary loads}}{\text{fracture toughness i.e. critical value of SIF}} \tag{2.1}$$

and

$$L_r = \frac{\text{current primary load}}{\text{limit load of the crack-containing perfectly plastic component}} \tag{2.2}$$

Here collapse of a perfectly plastic structure at yield stress σ_y is assumed to obtain the limit load F_Y. Hardening is partly taken into account by use of the so-called flow stress σ_f defined as the mean value of yield strength σ_y (i.e. R_{eL} or $R_{p0.2}$) and ultimate tensile strength σ_u

$$\sigma_f = \frac{\sigma_y + \sigma_u}{2} \tag{2.3}$$

and by S_r,

$$S_r = L_r \frac{\sigma_y}{\sigma_f} = L_r \frac{2\sigma_y}{\sigma_y + \sigma_u} \tag{2.4}$$

replacing L_r. Deformation is limited by assuming collapse at the load F_f obtained for σ_f. Clearly,

$$F_y = F_u \frac{\sigma_y}{\sigma_u}, \qquad F_f = F_u \frac{\sigma_f}{\sigma_u} \tag{2.5}$$

and

$$L_r = F/F_y, \qquad S_r = F/F_f. \tag{2.6}$$

More confusing, limit load is sometimes computed with allowable design stress S_m. All these are conservative assumptions for assessment purpose. Limit analysis with two-surface plasticiy predicts that plastic collapse of sufficiently ductile, hardening material occurs at the ultimate (limit) load F_u defined for perfectly plastic material with some limiting stress such as σ_u [74]. The same holds for the overlay model of limited kinematic hardening. Also experimental results propose that F_u could be used for best estimate purpose.

The so-called stress intensity factor (SIF) K_I measures the intensity of the elastic stress singularity at the crack-tip. It could be compared with a critical material value fracture toughness K_{Ic}. The index I denotes the most critical mode I crack opening. The limit load F_f is the load assumed to cause a local collapse of the ligament or a global collapse.

The pair of values of these variables (K_r, S_r) or (K_r, L_r) is used as coordinates of a so-called Failure Assessment Diagram (FAD). The assessment curve seperates critical failure region in which unstable crack growth and fracture may occur from the non-critical region in which fracture is assumed not to occur.

The two-criteria method is inspired by Dugdale's strip yielding model [10], [24]. In this model the plastic zones at the tips of a through crack of length $2a$ in an infinite plate of perfectly plastic material in plane stress is assumed in the form of yielding strips and the CTOD is given by [24]

$$\delta = \frac{8\sigma_f}{\pi E} a \ln\left(\sec\left(\frac{\pi}{2}\frac{\sigma}{\sigma_f}\right)\right). \tag{2.7}$$

Then the J-integral is obtained as

$$J = \sigma_f \delta = \frac{8{\sigma_f}^2}{\pi E} a \ln\left(\sec\left(\frac{\pi}{2}\frac{\sigma}{\sigma_f}\right)\right). \tag{2.8}$$

For $\sigma \to \sigma_f$ the fully plastic ligament is assumed with $\delta \to \infty$ and $J \to \infty$. This means that plastic collapse occurs at limit load F_f. At the other extreme, for $\sigma \ll \sigma_f$ small scale yielding is assumed. With $\sigma\sqrt{\pi a} = K_I$ equations (2.7), (2.8) become in the small stress limit

$$\delta = \frac{K_I^2}{E\sigma_f}, \qquad J = \frac{K_I^2}{E}. \tag{2.9}$$

Therefore, in the SIF-concept of linearly elastic fracture mechanics is obtained.

For $\sigma_{lin}\sqrt{\pi a} = K_{Ic}$ critical material values δ_c and J_c are assumed

$$\delta_c = \frac{K_{Ic}^2}{E\sigma_f}, \qquad J_c = \frac{K_{Ic}^2}{E}. \tag{2.10}$$

Equating (2.7) or (2.8) to (2.10) both give the same assessment curve

$$K_{Ic} = \sigma_{lin}\sqrt{\pi a} = \sigma_f\sqrt{\pi a}\left\{\frac{8}{\pi^2}\ln\left[\sec\left(\frac{\pi}{2}\frac{\sigma}{\sigma_f}\right)\right]\right\}^{1/2}. \tag{2.11}$$

Division by $\sigma\sqrt{\pi a}$, introducing

$$K_r = K_I/K_{Ic}, \qquad S_r = \sigma/\sigma_f, \tag{2.12}$$

noting that $K_r = \sigma/\sigma_{lin}$, and reorganizing gives

$$K_r = f_{R6} = S_r\left\{\frac{8}{\pi^2}\ln\left[\sec\left(\frac{\pi}{2}S_r\right)\right]\right\}^{-1/2}. \tag{2.13}$$

Obviously this equation removes the dependence on crack length a. The simple model decribes the dominating aspects of elasto-plastic fracture. Today it is successfully used in engineering fracture mechanics, although it is only derived strictly for plane stress in thin plates. For application to real structures the assessment equation (2.13) is used with the limit load F_f of a perfect plastic structure, i.e. S_r is set to

$$S_r = \sigma/\sigma_f = F/F_f. \tag{2.14}$$

This establishes a geometry independent interaction curve between the effective SIF and plastic collapse load (limit load) of a structure. It also represents the crack driving force (δ or J) in a dimensionless form.

Equation (2.13) represents a FAD constructed in the K_r–S_r plane. This corresponds to a failure stress of structures: $\sigma = \sigma_f$. It means that failure is associated with any combination of loading and crack size giving rise to a point (K_r, S_r) falling on or outside of this curve; and conversely, the combination will be safe if the point lies inside the curve.

The applicability of the above model for different structures of hardening material has been investigated by finite element analyses at CEGB [4] and at EPRI [36]. From the obtained results, it is concluded that despite the difference of geometry and material, R6 curve generally gives reasonable lower bounds. However, some exceptions are found in a cylinder of 304 stainless steel and also in our calculation of a cylinder with perfectly plastic material. Currently several types of FAD curves are identified for use with different kinds of material. Besides, advice is given in [4] for the computation material dependent assessment curves in the more involved R6 option 3 analyses.

- For low work hardening material the above equation (2.13) is used.
- For strongly work hardening materials, the R6 Revision 3 option 1 type assessment curve ([4], Garwood (1996) could be used to limit the non-critical region according to

$$K_r \leq f_{R6} = (1 - 0.14L_r^2)[0.3 + 0.7\exp(-0.65L_r^6)], \tag{2.15}$$
$$0 \leq L_r \leq L_r^{max} \tag{2.16}$$

For perfect plastic materials which exhibit a yield plateau the upper limit is $L_r^{max} = 1$. For other materials it is defined by use of allowable design stress S_m or by

$$\begin{aligned} L_r^{max} &= 1.15 \text{ for typical low alloy steels and welds} \\ L_r^{max} &= 1.25 \text{ for typical mild steel and austenitic welds} \\ L_r^{max} &= 1.8 \text{ for austenitic parent steels.} \end{aligned}$$

Another typical advice is to use

$$L_r^{max} = \frac{\sigma_f}{\sigma_y} = \frac{\sigma_y + \sigma_u}{2\sigma_y}. \tag{2.17}$$

That means, the curve is cut-off at different flow limits of the material. Hardening is only partly taken into account by use of the σ_f. As noted above, a less conservative proposal could be to use

$$L_r^{max} = \frac{\sigma_u}{\sigma_y} \tag{2.18}$$

for sufficiently ductile materials.

- For C-Mn (Mild) type steel operating in the strain aging regime the non-critical region could be defined by

$$K_r \leq f_{R6} = (1 - 0.1S_r^2 + 0.1S_r^4)/(1 + 3S_r^4), \qquad 0 \leq S_r < 1 \tag{2.19}$$

where the flow limit is used instead of the yield limit in the definition of L_r.

A comparison between these two curves is shown in Fig. 2.1. The initial R6 Rev.2 curve (2.13) (using S_r instead of L_r) may be not safe with respect to the strongly hardening model (2.15) for the example of the steel 20 MnMoNi 55 (comparable to A533 B Cl.1). In the following calculation however, the FEM results will usually be compared with R6 Rev.2 (2.13) for the sake of simplicity.

From the above statement, the establishment of the R6 curve for a real structure may be realized by an incremental elastic plastic fracture mechanics analysis. That is to establish a relation of K_{eff} (through elastic plastic integral J) in function of the applied stress or load level. Large numerical work has been done at CEGB [4]. Alternatively at EPRI, a J estimation procedure and also J-based FADs have been established [36]. In most published works, the numerical calculations consider a Ramberg-Osgood's power hardening material model

$$\frac{\varepsilon_{ij}}{\varepsilon_y} = \frac{\sigma_{ij}}{\sigma_y} + \beta\left(\frac{\sigma_{ij}}{\sigma_y}\right)^n, \qquad \beta \geq 0, \quad n \geq 1. \tag{2.20}$$

$\varepsilon_y = \sigma_y/E$ is the yield strain and n is the strain-hardening exponent. As a result, a tail is always obtained in the diagrams where the assessment line approaches the S_r abscissa asymptotically, see Fig. 8.3. For

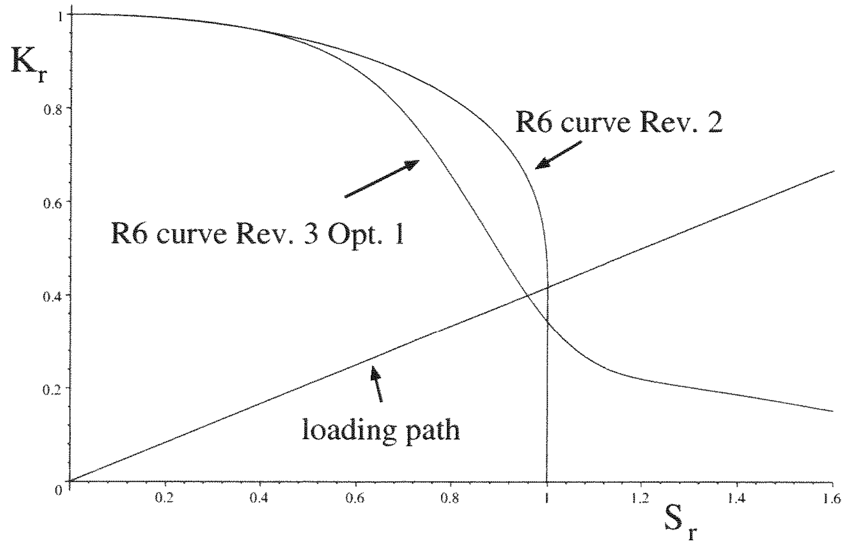

Figure 2.1: FAD curves for revisions 2 and 3 of R6 method

some materials whose hardening behaviour deviates considerably from a power law, [6] proposed a reference stress method as an improvement of the EPRI method. If only the yield stress σ_y is known the default level of the new SINTAP procedure suggests

$$K_r \leq f_{R6} = \frac{1}{\sqrt{1+0.5L_r^2}}[0.3 + 0.7\exp(-0.65L_r^6)], \tag{2.21}$$

$$0 \leq L_r \leq L_r^{max} \tag{2.22}$$

as a modification of (2.15). The new SINTAP procedures for materials with yield plateau are not considered here (see [73]).

In the presence of primary and secondary stress σ^p and σ^s SIFs K_I^p and K_I^s must respectively be computed [7]. Taking plastic interaction into account by a parameter $\rho(K_I^p, K_I^s, L_r)$ the fracture parameter K_r is obtained as

$$K_r = \frac{K_I^p + K_I^s}{K_{Ic}} + \rho. \tag{2.23}$$

For plane strain the equations (2.13),(2.15) or (2.19) can be stipulated to obtain an estimation of the J-integral (Rice integral)

$$J = \frac{(1-\nu^2)(K_I^p + K_I^s)^2}{E} \cdot \frac{1}{[f_{R6}(L_r) - \rho]^2}. \tag{2.24}$$

The second fraction on the right hand side may be interpreted as a plasticity correction function, based on the limit load, for the linear elastic value of J determined by the SIFs alone [11]. It is well known that J is only well-defined for nonlinearly elastic material. Strictly J is connected to flow theory of plasticity. But J proves a good approximation in many ductile fracture situations. It is compared to the critical material value for plane strain

$$J_c = \frac{(1-\nu^2)K_{Ic}^2}{E}. \tag{2.25}$$

The distinction between primary and secondary stress is left to engineering judgement in a sometimes obscure way. It is long known from geometrically linear limit analysis, that residual stresses may not lead to plastic collapse. They are therefore secondary. Residual stress is uniquely defined as the stress in a body in the absence of any mechanical load (no surface traction and no body forces). The new V-factor route in R6 code for treatment of secondary stresses is not considered [73].

Current techniques for the assessment of the likelihood of failure of a joint (such as the R6-Method or similar FAD approaches) are unable to cope explicitly with the presence of more than one material at a joint. These codes recommend that a safe analysis of a joint can be performed by assuming the joint to be homogeneous, and made from the weakest material at the joint. Although safe, this can lead to over-conservative estimates of the remaining lifetime of a structure. Therefore, the SINTAP project also considered the effect of strength mis-match (the base metal and welding metal have different strength) on R6 curve. Some finite element limit load analyses have been performed for this report. The centre-cracked welding plate model [35], [46], is considered as an example in Section 6.1. Its limit load is computed by direct methods and also by incremental calculations.

2.1.2 Engineering Treatment Method (ETM)

The ETM97 procedures are documented in the GKSS Procedure "Engineering Flaw Assessment Method (EFAM)". They have a modular structure consisting of the two versions ETM97/1 and ETM97/2 [47]. ETM is a simplified mechanical model which utilizes the material stress-strain behaviour to estimate characteristic quantities for fracture mechanics, such as CTOD (crack tip opening displacement) δ_5 defined for a gauge length of 5mm, the J-integral J and the load line displacement. The stress-strain curve of the material is assumed to be represented by Ludwik's piece-wise power hardening law [1], such that

$$\sigma = \begin{cases} E \cdot \varepsilon & \text{for} \quad \sigma \leq \sigma_y, \\ \sigma_y \left[\frac{\varepsilon}{\varepsilon_y}\right]^N & \text{for} \quad \sigma \geq \sigma_y, \end{cases} \tag{2.26}$$

which is a bilinear approximation in a log-log diagram. $\varepsilon_y = \sigma_y / E$ is the yield strain and $N, 0 \leq N \leq 1$, is the strain-hardening exponent. Plane stress is assumed. The limit load of the cracked component is termed yield load (load at net section yielding) F_y. At load F it is used to obtain

- For contained yielding ($F \leq F_y$):

$$\delta_5 = \frac{2.41}{E} \cdot K_I + \frac{K_{\text{Ieff}}^2}{E\sigma_y}\left[\frac{F}{F_y}\right], \qquad J = \frac{K_{\text{Ieff}}^2}{E} \tag{2.27}$$

- For the fully plastic state ($F \geq F_y$):

$$\frac{\delta_5}{\delta_{5Y}} = \left[\frac{F}{F_y}\right]^{1/N} = \left[\frac{J}{J_y}\right]^{1/(1+N)}. \tag{2.28}$$

where $\delta_{5Y} = \delta_5(F = F_y)$ and $J_y = J(F = F_y)$. K_{Ieff} is computed with the crack length virtually extended by Irwin's plane stress plastic zone correction. The version ETM97/2 is based on a more accurate determination of the yield load (limit load). It was one objective of SINTAP to unify the FAD and the crack driving force (CDF) route which follows the ETM approach [73].

[1] In metal forming Ludwik's piece-wise power hardening law is usually used with true stress and logarithmic strain measure

2.1.3 Experimental J-integral estimation

Today J-integral is mostly measured from the load-displacement curve in a standard specimen test. The area below the curve can be split into elastic and plastic energy U_{el} and U_{pl}, respectively. Consider the ASTM compact tension (CT) specimen with thickness B, crack length a and ligament $W - a$. Then J-integral split into elastic and plastic part may be written

$$J = J_{el} + J_{pl} = \frac{1}{B(W-a)}\left[\eta_{el}U_{el} + \eta_{pl}U_{pl}\right]. \tag{2.29}$$

For plane strain the elastic part may be obtained from the precise knowledge of SIF

$$J = \frac{K_{\mathrm{I}}^2(1-\nu^2)}{E} + \frac{1}{B(W-a)}\eta_{pl}U_{pl}. \tag{2.30}$$

The plastic η-factor may be determined if the limit load of the specimen is known. This is discussed in more detail for the CRB specimen in Section 5.1.2 below.

2.2 Shakedown analysis

Crack-like defects have been assumed to present infinitely sharp notches with associated singular elastic stress fields. Then shakedown of the crack containing structure is impossible. However, this singularity can be avoided if a blunted crack-tip is assumed. Then the question of crack propagation may be answered by shakedown analysis [13], [31]. This fairly new research is not considered in the current report.

2.3 Economic relevance

During manufacture of structures different processes like welding, shrinking and large deformation introduce crack-like defects. During operation of structures defects may grow or new defects may be created by loading, aging, and environmental influence. Fracture mechanics ensures the integrity of engineering structures which may contain cracks or defects. Apart from ensuring the safety of human lives and the protection of environment, this results in major financial savings.

In 1982 the USA estimated that the cost of fracture was of the order of 120 billion dollars per year, (4% of the gross national product). The annual costs could be reduced by 30 billion dollars by implementing the best available practice, including fracture control, defect assessment, inspection, maintenance and repair strategies. Education and training of informed personnel are key aspects of the transfer of technology into industrial practice. Research directed towards fracture related problems could further reduce the costs of fracture by 30 billion dollars per annum.

Although current engineering practice in fracture mechanics is safe, it is often too conservative, and may lead to the imposition of prohibitive repair and inspection policies. Economic pressure demands that plant down-time be minimized by avoiding unnecessary repairs and shutdowns. To achieve this goal it is essential that structural integrity methodologies minimize defects being prematurely sentenced as critical. Unnecessary levels of conservatism must therefore be avoided as they entail expensive and unnecessary inspections, outages, and repairs. An over conservative approach also penalizes life extension procedures on existing plants[2]. An over conservative approach also penalises life extension procedures on existing plants.

Research in defect assessment can be thought of under two sub-headings:

- Improved lifetime and performance predictions.
- Improved design through better stress analysis.

Current limit load solutions have been identified as a source of strong conservatism. This may originate from non-optimum limit load formulae, uncertain material data or inadequate theory [61]. The combination of the exact theory of limit analysis with the flexibility and precision of FEM analysis may help to identify conservative assumptions and to generate closer predictions. This will promote more economic defect assessments.

[2]There is also doubt about some handbook formulae. In 1998 the study concerning a defect observed in a component of the nuclear power plant of Fessenheim, which used the simplified method based on R6 method and handbooks to determine the crack nocivity, was not convincing for the Safety Authorities. Therefore, EDF had to perform a 3D calculation. This induced a certain delay of the restart of the nuclear plant that costed some 6 millions Euro.

3 The concepts of limit analysis

Static theorems are formulated in terms of stress and define safe structural states giving an optimization problem for safe loads. The maximum safe load is the limit load avoiding collapse. Alternatively, kinematic theorems are formulated in terms of kinematic quantities and define unsafe structural states yielding a dual optimization problem for the minimum of limit loads. Any admissible solution to the static or kinematic theorem is a true lower or upper bound to the safe load, respectively. Both can be made as close as desired to the exact solution. The limit load factor is defined in (3.1) and (3.2) by $\alpha = \mathbf{P}_l/\mathbf{P}_0$, where $\mathbf{P}_l = (\mathbf{b}_l, \mathbf{p}_l)$ and $\mathbf{P}_0 = (\mathbf{b}_0, \mathbf{p}_0)$ are the plastic limit load and the chosen reference load, respectively. Here we have supposed that all loads (**b** body forces and **p** surface loads) are applied in a monotonic and proportional way. We will first state the theorems.

1. *Static or lower bound theorem:* Find the maximum load factor for which the structure is safe. The structure is safe against plastic collapse if there is a stress field $\boldsymbol{\sigma}$ such that the equilibrium equations are satisfied and the yield condition is nowhere violated. We could then formulate a maximum problem:

$$\begin{aligned} \max \quad & \alpha \\ \text{s. t.} \quad & \Phi(\boldsymbol{\sigma}) \leq \sigma_y \quad \text{in } V \\ & \operatorname{div}\boldsymbol{\sigma} = -\alpha \mathbf{b}_0 \quad \text{in } V \\ & \boldsymbol{\sigma}\, \mathbf{n} = \alpha \mathbf{p}_0 \quad \text{on } \partial V_\sigma \end{aligned} \tag{3.1}$$

for the structure V, traction boundary ∂V_σ (with outer normal $\mathbf{n}$), yield function Φ, body forces $\alpha\mathbf{b}_0$ and surface loads $\alpha\mathbf{p}_0$.

The maximum problem (3.1) is solved by splitting the actual stresses $\boldsymbol{\sigma}$ into fictitious elastic stresses and residual stresses and solving the deduced problem by a basis reduction technique in the residual stress space and by Sequential Quadratic Programming (SQP) (see [26], [54], [59], [74]).

2. *Kinematic or upper bound theorem:* Find the minimum load factor for which the structure fails. The structure fails by plastic collapse if there is a (kinematically admissible) velocity field such that the power of the external loads is higher than the power which can be dissipated within the structure.

$$\begin{aligned} \min \quad & \alpha_k \\ \text{with} \quad & \alpha_k = \dot{W}_{in} = \int_V \dot{\varepsilon_{eq}}^P \sigma_y dV \\ \text{s. t.} \quad & 1 = \dot{W}_{ex} = \int_V \mathbf{b}_0^T \dot{\mathbf{u}} dV + \int_{\partial V_\sigma} \mathbf{p}_0^T \dot{\mathbf{u}} dA \geq 0, \\ & \dot{\varepsilon} = \frac{1}{2}(\nabla \dot{\mathbf{u}} + (\nabla \dot{\mathbf{u}})^T) \quad \text{in } V, \\ & \dot{\mathbf{u}}(t) = \dot{\mathbf{u}}^0(t) \qquad \text{on} \quad \partial V_u, \end{aligned} \tag{3.2}$$

for the structure V, boundary $\partial V = \partial V_p \cup \partial V_u$ with σ_y is the yield limit of the material, $\dot{\varepsilon_{eq}}^P = \sqrt{2/3\dot{\varepsilon}^P : \dot{\varepsilon}^P}$ the effective, plastic strain rate. The objective function is non-smooth. Different regulrizations are used in [68], [71], [63]). To solve the minimization problem (3.2), the method of the reduced-gradient algorithm in conjunction with a quasi-Newton algorithm [41] is used in [68], [71].

Upper and lower bound converge to the same solution, if all conditions of the theorems are exactly satisfied. This may be difficult in a FEM discretisation. However, computing both bounds the numerical errors may be monitored.

For limited kinematic hardening material the limit load factor is obtained by the same optimization problems with σ_y replacing σ_u. For homogeneous material the computed limit load is a linear function of the chosen failure stress. From the theorems it is clear that the larger lower bound is always the better choice of two limit load formulae. Similarly the lower one should be chosen of two upper bounds. It would help such decisions, if handbooks would indicate which theorem was used to generate a limit load formula. If upper and lower bound coincide, one could state that the true solution has been found.

Consider a perfect structure in plane or axisymmetric stress. A defect generates a local triaxial stress field, because local high strains are constrained by the surrounding field. The uncracked structure with one dimension reduced to ligament (net section) size is used to measure the plastic constraint factor L,

$$L = \frac{\text{limit load of the cracked component}}{\text{limit load of uncracked net section}}. \tag{3.3}$$

This is also the definition of the limit load factor α i.e. $\alpha = L$. The maximum plastic constraint factor, which can be achieved for e.g. double-edge cracked tension plates (DENT) is

$$L = \frac{2}{\sqrt{3}}\left(1 + \frac{\pi}{2}\right) = 2.9685 \tag{3.4}$$

for von Mises material (by first eq. (4.8)).

The deeper the crack the more the constrained field tends towards plane strain with limit load increased by the increase of L. For respectively shallow and deep cracks the plane stress and plane strain limit load solution is more appropriate. Few of the cited handbooks give recommendations for a proper choice of the constraint. A high L may not be achieved due to prior brittle failure if the material is not sufficiently ductile (Charpy impact energy below $60J$ [34]). Therefore, plane stress should be chosen as a lower bound solution for assessment purpose. The corresponding plane strain solution is an upper bound.

4 Singularity simulation for elastic-perfectly plastic fracture analysis

It is well known that the stresses and strains in the crack-tip region of an elastic plastic material, defined by the Ramberg-Osgood material equation (2.20), are controlled by the so-called HRR field (4.1) in 2D case [33], [44].

$$\sigma_{ij} = \sigma_y \left(\frac{EJ}{\sigma_y I_n r}\right)^{\frac{1}{n+1}} \tilde{\sigma}_{ij}(\theta, n), \qquad \varepsilon_{ij} = \varepsilon_y \left(\frac{EJ}{\sigma_y I_n r}\right)^{\frac{n}{n+1}} \tilde{\varepsilon}_{ij}(\theta, n) \tag{4.1}$$

where σ_0, ε_0 and n are yield stress, yield strain and hardening power of material, respectively. β is material constant, J is J-integral of Rice; E Young's modulus; θ, r co-ordinates at crack tip, I_n n-depending constant; $\tilde{\sigma}_{ij}$ and $\tilde{\varepsilon}_{ij}$ non-dimensional function. When $n = 1$ it is the case of linear elasticity

$$\sigma_{ij} \to r^{-1/2}\tilde{\sigma}_{ij}(\theta), \qquad \varepsilon_{ij} \to r^{-1/2}\tilde{\varepsilon}_{ij}(\theta) \tag{4.2}$$

and $n \to \infty$ corresponds to the case of perfect plasticity, i.e. we arrive at

$$\sigma_{ij} \to r^{0}\tilde{\sigma}_{ij}(\theta), \qquad \varepsilon_{ij} \to r^{-1}\tilde{\varepsilon}_{ij}(\theta) \tag{4.3}$$

We see that the stress has no longer a singularity while the strain field near crack tip presents a strong singularity of $(1/r)$ for a perfectly plastic analysis. It is important to simulate this singularity in upper bound limit analysis of cracked structures. Following a work of Barsoum [12], we recommend here a simple technique to use special degenerated elements in upper bound calculation. An independent proof for this technique is given for element model of Fig. 4.1a). We note that the model of Fig. 4.1c) was proposed and demonstrated in [12]. The geometry of a 8-noded plane isoparametric element is mapped into the normalized square space (ξ, η), $(-1 \le \xi \le 1, -1 \le \eta \le 1)$ through the transformations:

$$x = \sum_{i=1}^{8} N_i(\xi,\eta)x_i \qquad y = \sum_{i=1}^{8} N_i(\xi,\eta)y_i \qquad \text{where} \tag{4.4}$$

$$\begin{aligned} N_i(\xi,\eta) &= \Big[(1+\xi\xi_i)(1+\eta\eta_i) - (1-\xi^2)(1+\eta\eta_i) - (1-\eta^2)(1+\xi\xi_i)\Big]\xi_i^2\eta_i^2/4 \\ &+ (1-\xi^2)(1+\eta\eta_i)(1-\xi_i^2)\eta_i^2/2 + (1-\eta^2)(1+\xi\xi_i)(1-\eta_i^2)\xi_i^2/2 \end{aligned}$$

$\xi_i\,\eta_i = \pm 1$ for the corner nodes and zero for mid-side nodes. x_i, y_i are the nodal co-ordinates of the element. For the element shown in Fig. 4.1a), we have

$$\begin{aligned} x_1 &= x_4 = x_8 = 0,\ \ x_2 = x_3 = x_6 = h,\ \ x_5 = x_7 = h/2 \\ y_1 &= y_2 = y_4 = y_5 = y_8 = 0,\ \ y_3 = l,\ \ y_6 = y_7 = l/2 \end{aligned} \tag{4.5}$$

Using these relations we can finally deduce strain components as below. A detailed description is given in Appendix A.

$$\begin{aligned} \frac{\partial u}{\partial x} &= A_0 + A_1 r + \frac{A_2}{r}, & \frac{\partial u}{\partial y} &= B_0 + B_1 r + \frac{B_2}{r}, \\ \frac{\partial v}{\partial x} &= C_0 + C_1 r + \frac{C_2}{r}, & \frac{\partial v}{\partial y} &= D_0 + D_1 r + \frac{D_2}{r} \end{aligned} \tag{4.6}$$

A_i, B_i, C_i, D_i $(i = 0, 2)$ are all constants independent of r. It is clear that as $r \to 0$, all strain component express a singularity of $1/r$. This singularity just satisfies the requirement of perfectly plastic analysis. At

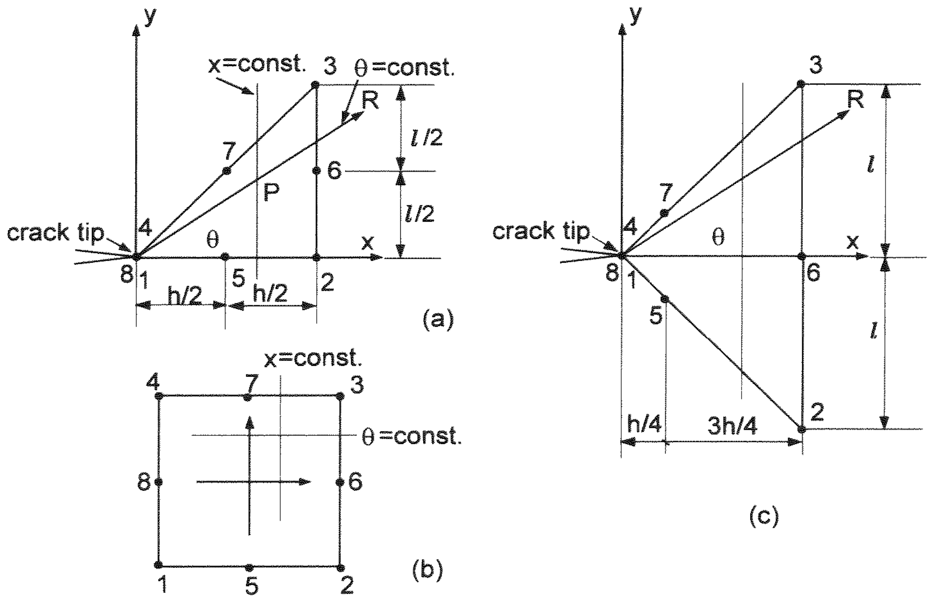

Figure 4.1: (a) Isoparametric degenerated element; (b) Parent element (c) Model proposed in [12]: quarter-point degenerated element

the same time a constant term and a linear one represent the constant strain and linear-varying strain terms, which are essential when dealing with thermal loads and when connecting to other normal isoparametric elements out of crack tip. This numerical technique, used already in incremental elastic plastic calculation by Kumar et al. [36] and others, will be proved useful in the present upper bound analysis.

We note here that the term b_0 and d_0 in Eq. A.9 will be identically zero if we impose the constraints as $u_1 = u_4 = u_8$ and $v_1 = v_4 = v_8$ (see eq. (*) in Appendix A). In this case, A_2, B_2, C_2, D_2 in (4.6) are null. Therefore we will lose the strain singularity at crack tip.

Using the model shown by Fig. 4.1c), Barsoum has demonstrated in [12] a similar singularity for strain components:

$$\begin{aligned} \frac{\partial u}{\partial x} &= A_0' + \frac{A_1'}{\sqrt{r}} + \frac{A_2'}{r} & \qquad \frac{\partial u}{\partial y} &= B_0' + \frac{B_1'}{\sqrt{r}} + \frac{B_2'}{r} \\ \frac{\partial v}{\partial x} &= C_0' + \frac{C_1'}{\sqrt{r}} + \frac{C_2'}{r} & \qquad \frac{\partial v}{\partial y} &= D_0' + \frac{D_1'}{\sqrt{r}} + \frac{D_2'}{r} \end{aligned} \tag{4.7}$$

The strain components show the $(1/\sqrt{r} + 1/r)$ singularity. However, no linear varying term is given. If the nodes 1,4 and 8 are constrained to have the same displacement, only the inverse square root singularity remains, which is suited to linear elastic fracture analysis. Obviously the singularity $1/r$ is obtained only by the separation of crack tip nodes and this singularity is dominant at crack tip. The quartered-node technique is not necessary.

By contrary, stresses are the principal variables in static lower bound theorem instead of kinematic ones. So the above strain singular element is not necessary. However, Barsum's quartered-node stress singular element should be applied to simulate the fictitious elastic stress, because it can simulate a singularity of $(1/\sqrt{r})$.

We will present various numerical examples to show the efficiency of the present upper bound method and the usefulness of strain singular element.

4.1 Double-edge cracked plate under tension (DENT)

We consider a double-edge cracked plate under traction, cf. Fig. 4.6, in both plane stress and plane strain states. Owing to symmetry, only one quarter of structure is modelled with 30 elements. Four types of elements around crack tip are examined to make a comparison. The result of limit loading factor is shown in Table 4.1. We see clearly that with almost same element mesh, strain singular element (Fig. 4.2) indeed give best result which is in excellent agreement with the analytic solution [29], because it has been proved being $1/r$ singular at crack tip and suitable for plastic fracture analysis. The limit load results of various crack length are shown in Fig. 4.6 in both plane stress (PS) and plane strain (PD) condition. Present solutions in plane stress condition are almost exactly identical to the analytic solution in [29]. In plane strain condition, the results also accord well with the analytic solution of Ewing & Hill [22] with the maximum error less than 3.8%. This is due to the fact that the incompressibility is considered in a weak form in present formulation in eq. (3.2).

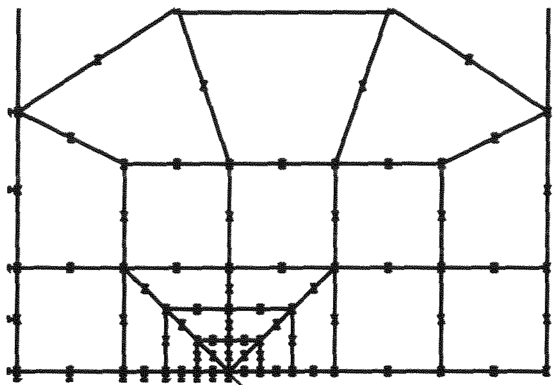

Figure 4.2: Finite element meshing of type C

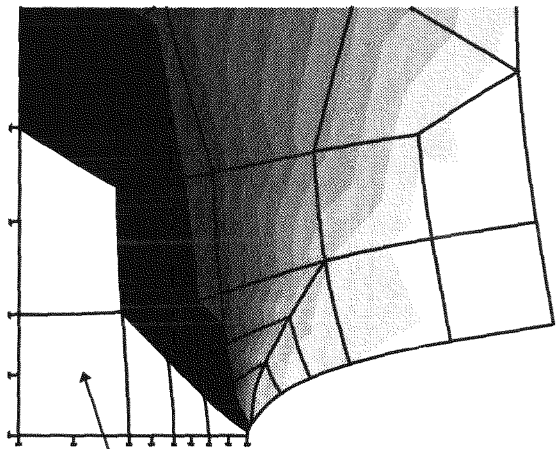

Figure 4.3: Crack tip and von Mises field in plastic limit state

- Plane strain, Ewing & Hill [22]

$$\alpha = \frac{2}{\sqrt{3}}\left(1+\frac{\pi}{2}\right) \qquad \text{for } a/b \geq 0.884$$
$$\alpha = \frac{2}{\sqrt{3}}\left[1+\ln\left(\frac{1}{2}+\frac{b}{2c}\right)\right] \qquad \text{for } a/b \leq 0.884 \tag{4.8}$$

where $\alpha = \bar{\sigma}_c/\sigma_y$, $\bar{\sigma}_c$ is mean limit stress in net section $2cT$, σ_y is the yield limit of the material. The limit load of the DENT specimen of thickness T is obtained by

$$F_y = \alpha 2cT\sigma_y. \tag{4.9}$$

- Plane strain, Kumar [36]

$$\alpha = (0.72b/c + 1.82)/2 \tag{4.10}$$

- Plane stress (deep crack), Hill [29]

$$\alpha = 2/\sqrt{3} \qquad \text{for } a/b \geq 0.261 \tag{4.11}$$

Constraint	Analytic	used crack tip elements			
Factor	solution	Element A	Element B	Element C	Element D
α_M	1.1547	1.216	1.186	1.156	1.209
Error %	-	5.3	2.7	0.1	4.7

Table 4.1: Comparison of limit load solutions with different crack-tip elements

Element A: ordinary isoparametric element locally refined; B: Barsoum's quarter point singular element; C: separating-point degenerated element (Fig. 4.1a); D has same form as element C but having only one node at crack tip.

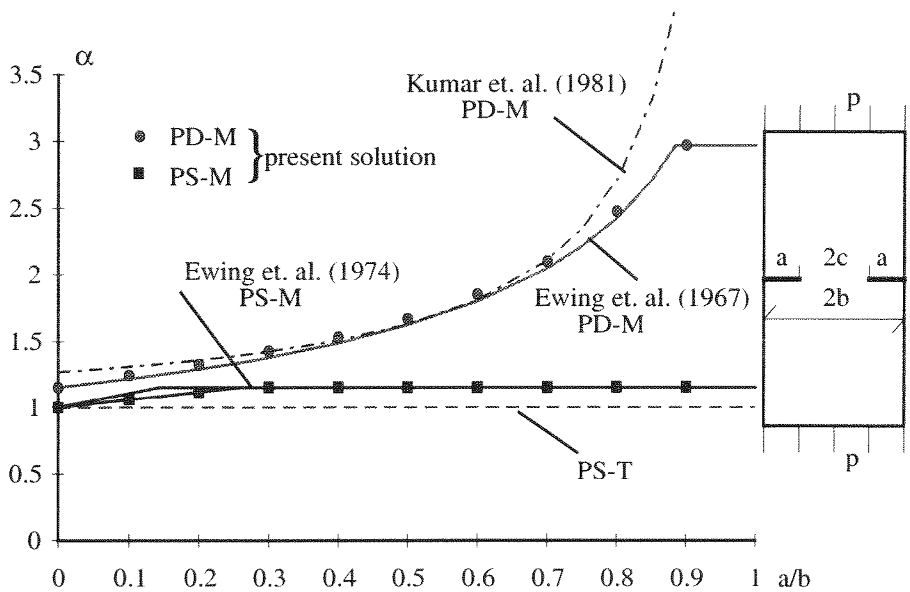

Figure 4.6: Plastic limit of DENT specimen (note: $\alpha = \bar{\sigma}_c/\sigma_y$ where $\bar{\sigma}_c$ is mean limit stress in net section 2c; PS-Plane stress; PD-Plane strain; T-Tresca; M-von Mises criterion)

5 Numerical and experimental validation

5.1 η– factor for fracture toughness estimation for Circumferentially Cracked Round Bars (CRB)

The geometry of the CRB specimen is shown by Fig. 5.1. This cylindrical geometry is of increasing interest in fracture mechanics experiments [55], as it is easy to test on a usual tensile machine, and especially it requires small amount of material. We take this example to illustrate an application of limit load in the estimation of fracture toughness of material.

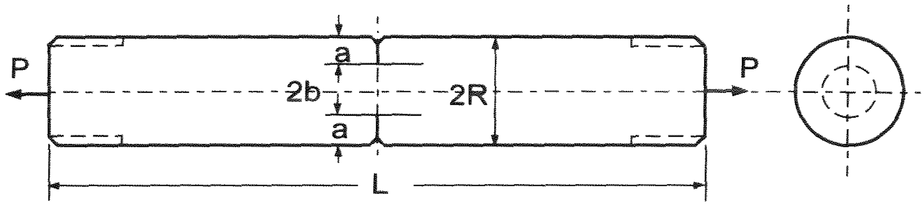

Figure 5.1: Circumferentially-cracked round bar (CRB) under tension (L=55mm, R=5mm)

The estimating procedure of elastic plastic fracture toughness by some standard specimens have been documented in ASME standard. Similar estimating procedure for CRB specimen is still under investigation and seems to be promising. The present work will show how to apply limit load function of CRB to derive elastic plastic fracture toughness.

5.1.1 Limit load function of CRB specimen

• Miller's presentation with Tresca's criterion

In a review paper, Miller [37] summaries a solution from the literature:

$$\alpha_l = \frac{F_l}{\pi b^2 \sigma_y} = \begin{cases} 2.85 & \text{for } a/R > 0.65 \\ \frac{R}{b} & \text{for } a/R < 0.65 \end{cases} \tag{5.1}$$

α_l represents really the constraint factor L. The solution of deep crack ($a/R > 0.65$) is exact with Tresca's criterion and it is an approximate linear interpolation for $a/R < 0.65$ (5.1) given by Akhurst & Ewing. However, the deep crack solution obtained initially by Shield was defined for $a/R > 0.69$, [37].

• Present solution with von Mises' criterion

In order to improve the quality of limit load function, a series of finite element calculations have been performed with present mathematical programming method. About 30 axisymmetric isoparametric elements are used (4 special crack-tip elements have been used). The calculation with more element showed that the results obtained by the coarse meshes have enough precision. The results are summarized in Table 5.1

The numerical results are presented in Fig. 5.2, where we see that a perfect platform forms in $b/R = 0 \sim 0.3$ (deep crack). This is characteristic of cracked structures, which demonstrates good precision of the present results.

The limit load results of ELSA have been fitted into explicit formula (5.2) imposing the continuity of derivatives at $a/R = 0.7$, which corresponds to the transformation of two different plastic modes: one is

b/R	0.1	0.2	0.3	0.35	0.4	0.5	0.6	0.7	0.8	0.9	1.0
F_l/F_c	3.00	3.00	2.989	2.9306	2.7688	2.416	2.0528	1.7306	1.4422	1.2062	1.0

* reference: F_c- the limit load of net-section of cracked bar; $F_c = \pi b^2 \sigma_y$

Table 5.1: Limit load of CRB specimen by ELSA

confined plasticity in the ligament for very deep cracks and another spread plasticity for a shallow crack. The transition point $a/R = 0.7$ also approaches the one of Shield ($a/R = 0.69$, [37])

$$\alpha_l = \frac{F_l}{\pi b^2 \sigma_y} = \begin{cases} 3 & a/R \geq 0.7 \\ -1.497 + 3.11352\frac{R}{b} - 0.6539\left(\frac{R}{b}\right)^2 + 0.03738\left(\frac{R}{b}\right)^3 & a/R < 0.7 \end{cases} \tag{5.2}$$

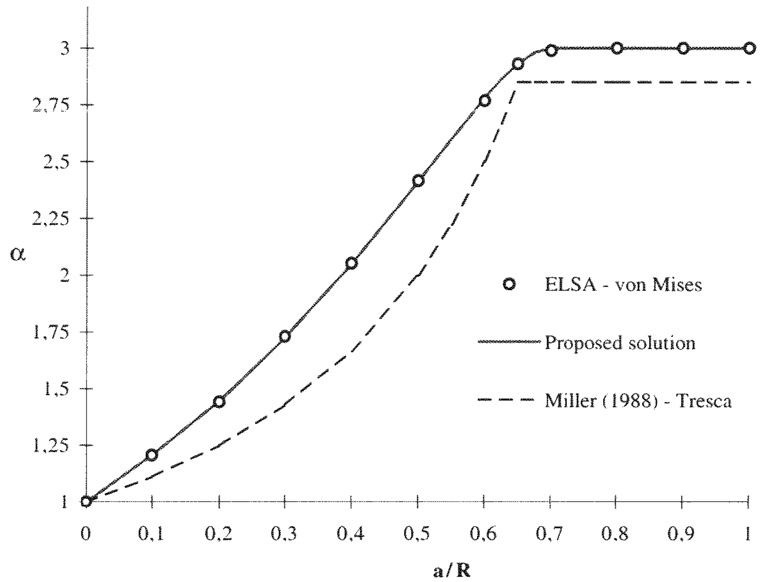

Figure 5.2: Non-dimensional limit load of CRB specimen, (triaxiality factor) $\left(\alpha_l = \frac{F_l}{\pi b^2 \sigma_y}\right)$

In comparison with the previous solution presented by Miller [37], the difference of 5% for deep cracks is due to the different criteria. Von Mises' criterion is adopted in present calculation while Tresca's criterion is used in Miller's solution. It is also interesting to notice that the constraint factor for the deeply-cracked CRB specimen is 2.85 for Tresca material and 3 for von Mises material, which are much higher than for centre cracked plate. For the shallow crack problem, the present results show that the linear interpolation presented by Miller is too simple. The proposed solution (5.2) should be used when an accurate estimation of limit load with von Mises criterion is required.

The limit load solution has also been obtained by Down [43], by a incremental iterative calculation. A comparison between present solution and the curve of Down shows a good agreement.

5.1.2 η–factor formulation by limit load function

J-integral formula introduced in [44] requires the knowledge of stress and strain field on a path around the crack tip. It usually involves time-consuming finite element calculation. On the other hand, J-integral is also interpreted as an energy released rate per unit of crack area. For the present CRB specimen, we can write:

$$J = \frac{K_I^2(1-\nu^2)}{E} + \frac{1}{2\pi b}\frac{\partial U_{pl}}{\partial b} \tag{5.3}$$

with

$$U_{pl} = \int_0^{\delta_{pl}} F\, d\delta_{pl} \tag{5.4}$$

where U_{pl} the dissipated plastic strain energy during the loading by F and δ_{pl} the plastic part of the displacement of loading point. K_I could be evaluated through the formula of Benthem & Koiter [14],

$$K_I = K_o\left(1-\frac{a}{R}\right)^{(-3/2)} 0.5\left[1+0.5\left(\frac{b}{R}\right)+0.375\left(\frac{b}{R}\right)^2-0.363\left(\frac{b}{R}\right)^3+0.731\left(\frac{b}{R}\right)^4\right] \tag{5.5}$$

with

$$K_o = \frac{F}{\pi b^2}\sqrt{\pi a\frac{b}{R}} = F\sqrt{\frac{a}{\pi R}} \tag{5.6}$$

Introducing a so-called η–factor [43], [48]

$$\eta = \frac{b}{2U_{pl}}\frac{\partial U_{pl}}{\partial b} = \frac{1}{2}\frac{\partial \ln(U_{pl})}{\partial \ln(b)} \tag{5.7}$$

(5.3) becomes

$$J = \frac{K^2(1-\nu^2)}{E} + \eta\frac{U_{pl}}{\pi b^2} \tag{5.8}$$

The concept of η–factor, already adopted by ASTM E813 standard for some standard specimens, represents here the ratio of the plastic part of J-integral and plastic energy per unit of ligament area. It has been largely used for compact tension and three-point bending specimens and leads to very simple and useful approximate formulae for J-integral estimate. The determination of η–factor for centre cracked weld plate was reported in [35] and will be discussed in next section. For the CRB specimen, the application of η–factor is promising. The η–factor could be determined by a series of experiments using (5.7), or by a known limit load function because one has the following relation for a rigid perfectly plastic material:

$$\eta = \frac{1}{2}\frac{b}{F_l}\frac{\partial F_l}{\partial b} \tag{5.9}$$

This could be deduced from the definition (5.7). It appears that if we have obtained the limit load function F_l of CRB specimen, we may find the elastic-plastic fracture toughness of material through a simple traction test by means of (5.4) and (5.8). This process has been applied in the ASTM code for some standard specimens.

Therefore, by using limit load function of Miller (5.1), one can deduce the following approximate solution from (5.9)

$$\eta = \begin{cases} 1 & \text{for } a/R > 0.65 \\ 0.5 & \text{for } a/R < 0.65 \end{cases} \tag{5.10}$$

It is constant in two regions but discontinuous at $a/R = 0.65$. Only shallow crack solution was initially suggested to apply by Neale [43]. However, it is based on a simple linear interpolation.

On the other hand, with the proposed limit load function (5.2), we may derive a new η–factor by using (5.9), which is represented as a continuous function of R/b :

$$\eta = \begin{cases} 1 & a/R \geq 0.7 \\ \dfrac{-1.497 + 1.55676\dfrac{R}{b} - 0.01869\left(\dfrac{R}{b}\right)^3}{-1.497 + 3.11352\dfrac{R}{b} - 0.6539\left(\dfrac{R}{b}\right)^2 + 0.03738\left(\dfrac{R}{b}\right)^3} & a/R < 0.7 \end{cases} \tag{5.11}$$

When $a/R < 0.6$ for shallow crack, (5.11) may be approximated by a linear relation:

$$\eta = 0.045 + 1.1583\frac{a}{R} \qquad \text{for } a/R < 0.6 \tag{5.12}$$

The results (5.11), (5.12), with Neale's approximation (5.10), are shown in Fig. 5.3. It should be noticed

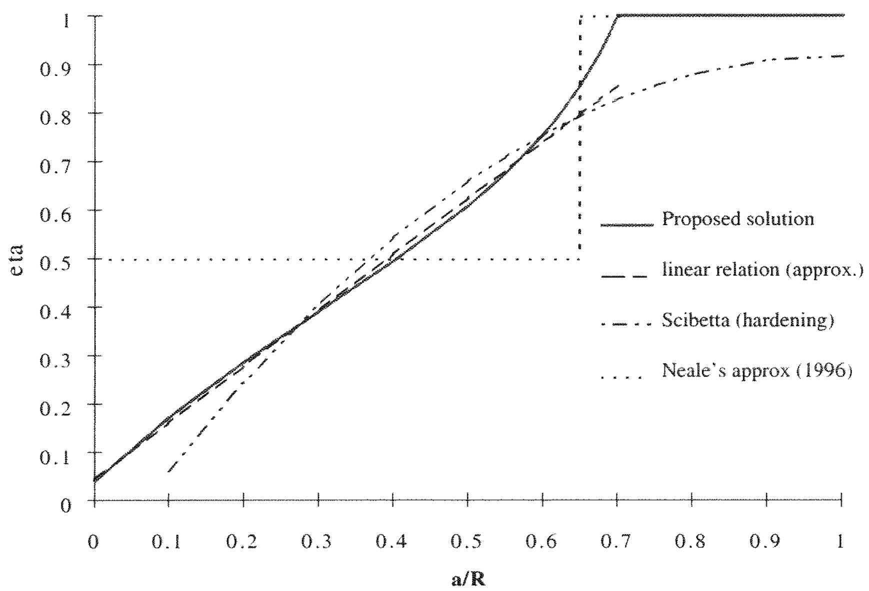

Figure 5.3: η–factor derived from limit load function

that (5.11) or (5.12) is deduced with an ideal plastic material model. It is necessary to examine it for an usual strain hardening material. Therefore we give in Fig. 5.3 the finite element solution of Scibetta [48] with a special strain hardening power $n = 10$, defined in (5.1). In Fig. 5.3 we see that this elastic plastic finite element solution is near to present solution (perfectly plastic material) in the interested region ($0.3 < a/R < 0.7$). However, it was noticed that the load level has an effect on the η–factor for shallow crack problem. That means, only for deeply cracked problem the η–factor is constant. This is due to the change of the plastic zone shape by the geometrical effect. In order to consider these effects, it has been suggested to introduce a plastic displacement δ_{pl} (loading point) into the η–factor formula as a correction [51]. Alternatively it can be expressed as function of load level.

5.1.3 Experiments using CRB specimens

The experimental estimation of the η–factor in [49] provides experiments for comparison with (5.2). The tensile properties of the typical French pressure vessel steel 18MND5 (AFNOR standard) were measured

R_{p02}	R_m	A_g	A_5	Z	$J_{0.2}$
518 N/mm^2	661 N/mm^2	12%	24%	76%	270 kJ/m^2

Table 5.2: Material data of CRB specimens at ambient temperature [49].

at ambient temperature. No Lüder's bands were observed. The strain hardening exponent was $n = 0.093$. Due to the very low brittle to ductile transition temperature (T_0 about $-80\,^\circ C$) the tests did not show any cleavage fracture behaviour at room temperature [50]. Therefore, K_{Ic} is not defined. $J_{0.2}$ for $0.2mm$ blunting initiation is about $270kJ/m^2$.

Specimen	1	2	3	4	5
a/R	0.767	0.677	0.588	0.520	0.443
$F_{exper.}/F_u$	0.98	0.93	0.89	0.95	1.00

Table 5.3: Results of limit analyses for different FEM-models and experiments computed from $F_{exp.}/F_f$ in [49].

From FAD the experimental rupture loads $F_{exper.}$ must be expected to be lower than the numerical limit loads F_u. Obviously, the values $F_{exper.}$ come close to the numerical upper bounds limit loads F_u which would be obtained with R_m from (5.2). Save predictions may be achieved in a FAD. Note, that [49] uses σ_F with (5.2). Further experimental validations for circumferentially-Notched Round Bars (NRB) are presented in [28].

a/R	δ_{pl}	η
0.599	0.16	0.79
0.599	0.05	0.77
0.600	eqn (5.11)	0.755

Table 5.4: η–factor from experiments and from limit analysis [49].

According to (5.7) the η–factor is derived experimentally as the slope of a straight line fitted by least squares method to the experimental data in a log-log presentation of $2ln(b)$ v.s. $ln(U_{pl})$. The average crack length to bar radius of all five experiments is $a/R = 0.599$. For further discussion see [49].

5.2 Compact tension specimens CT25

5.2.1 Direct application of limit analysis

In predicting the failure pressure for 134 longitudinally flawed pipes and vessels with four engineering methods the "best" method was within ± 10 % (± 20 %) in only ± 40 % (± 60 %) of all cases [61]. This result can partly be attributed to the used failure concepts and their mathematical formulations and to the uncertain material data and crack geometries. The majority of the tested formulae were obtained by some kind of limit analysis, although the authors used different names for them. Therefore, a need of an exact formulation of limit loads for cracked structures is evident. We will compare different solutions for Compact Tension (CT) specimens for which Seidenfuß has performed very careful experimental and numerical investigations [52].

Seidenfuß analysed four different ASTM standard CT25 specimens made of 20 MnMoNi 5 5 (comparable to the steel A533 B Class 1 or to the French steel 16MND5) [52]. The specimens have the dimensions shown in Table 5.4 with the crack length a, the length L, thickness B, height H and a reference length W. The different crack–lengths were generated by a fatigue crack propagation test. The specimens are grooved (20 %) on both sides so that a plane strain state is reached in the interior of the specimens. The experiments were performed at a temperature of $80\,^{\circ}C$ at the beginning upper shelf of the Charpy V-notch impact energy (some 200 J).

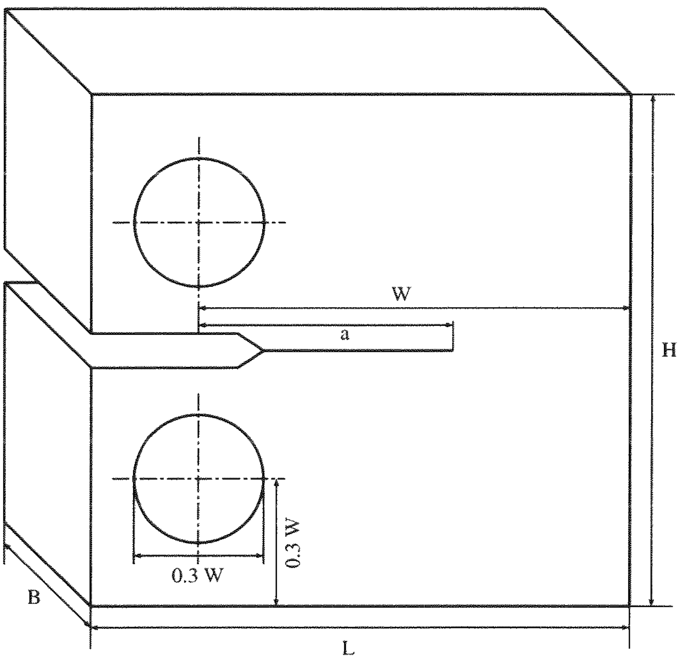

	AB15	AC18	AC19	AC20
W	50.00	50.00	50.00	50.10
a	39.50	34.80	29.30	28.96
a/W	0.790	0.696	0.586	0.578
L	62.50	62.50	62.50	62.50
B	25.00	25.00	25.00	24.71
H	60.00	60.00	60.00	60.00

Figure 5.4: FE-model dimensions similar to CT25 specimens in $[mm]$ (see [52])

The measured material data at $80\,^{\circ}C$ are shown in Table 5.5 (see [52]). Instead of using the measured strength data in the analyses, Seidenfuß used the strength data ($R_{p02} = 393\ N/mm^2$, $R_m = 533\ N/mm^2$) from a fit to data at different temperatures [53] for different specimen orientations. This gives a first indication of isotropy and of expected experimental uncertainty. The material toughness K_{IC} is generated from the $J-R$-curve [53].

R_{p02}	R_m	Young's modulus E	Poisson's ratio ν	Material toughness K_{IC}
379 N/mm^2	513 N/mm^2	207000 N/mm^2	0.3	7851 $N/mm^{1.5}$

Table 5.5: Material data of CT25 specimens [52], [53] at $80\,^{\circ}C$

With the measured critical value $J_c = 271 N/mm$ and the values from Table 5.5, the material toughness K_{IC} is estimated for plane strain:

$$K_{IC} = \sqrt{\frac{J \cdot E}{1-\nu^2}} = 7851 N/mm^{1.5} \tag{5.13}$$

The results of the limit load F_{lim} of the CT25 specimens are compared with the following approximations. For the approximation formulae the thickness B has to be reduced by 20 % to $B = 20\ mm$.

- HOLLSTEIN, SCHMITT:
  Ungrooved plane strain model, experimental fit [30].

$$F_{lim} = 0.68 \frac{(W-a)^2}{W+a} B \cdot R_{p02}, \tag{5.14}$$

- KUMAR, SHIH:
  Ungrooved plane strain model, perfectly plastic material, [36].

$$F_{lim} = 1.455 \left(\sqrt{2(W^2 + a^2)} - (W+a) \right) \cdot B \cdot R_{p02}, \tag{5.15}$$

- EWING, RICHARDS:
  Ungrooved plane strain model with $\sigma_f = 0.5 \cdot (R_{p02} + R_m)$, [23], [45].

$$F_{lim} = \frac{2}{\sqrt{3}} \left(\sqrt{2.702W^2 + 4.599a^2} - W - 1.702a \right) \cdot B \cdot \sigma_f. \tag{5.16}$$

Different FE models were generated for the limit analysis of the experiment AC19. Because of symmetry only one quarter of the specimens is modelled. The FEM meshes for the model–types of AC19 are shown in Figure 5.5. The other experiments AC18, AC20 and AB15 were analyzed by similar 2D plane strain and 3D meshes.

- CT2D1:
  2-D model with 210 triangular 6–node plane strain elements (TRIMP6) and 484 nodal points, $B = 20$

- CT2D2:
  2-D model with 210 triangular 6–node plane stress elements (TRIM6) and 484 nodal points, $B = 20$

- CT3D1:
  3-D model with 1060 pentahedron 18–node elements (PENTAC18) and 5324 nodal points, with modelling of the side grooves, $B = 25$

- CT3D2:
  3-D model with 1060 pentahedron 18–node elements (PENTAC18) and 5324 nodal points, without modelling of the side grooves, $B = 20$

A lower bound LISA software implemented into the FE-code PERMAS was used to compute ultimate loads F_u i.e. limit loads for failure stress σ_u. The results of these limit analyses are compared in Table 5.2.1 with the experimental collapse loads. It should be expected that the load is higher for experiment AC20 than for AC19, because the load-carrying capacity increases with decreasing crack length a. Obviously, all computed limit loads are well within the experimental scatter for the most realistic 3D model CT3D1 with side grooves. There is strong experimental support for the choice of σ_u for realistic limit analyses of the experiments.

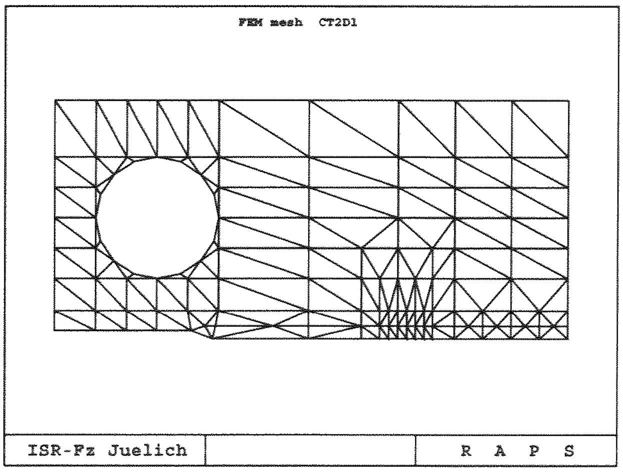

(a) Models CT2D1 and CT2D2

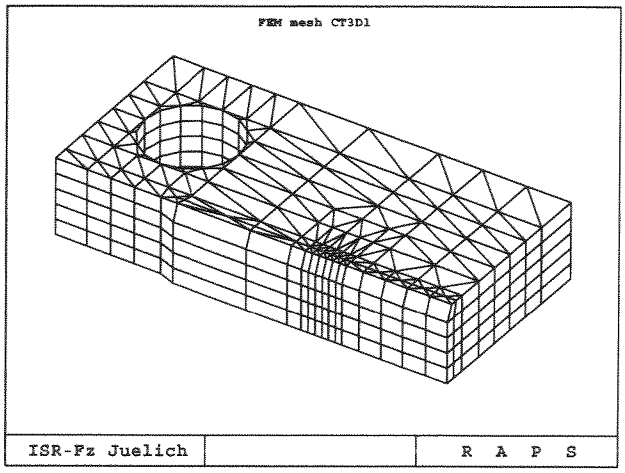

(b) Model CT3D1

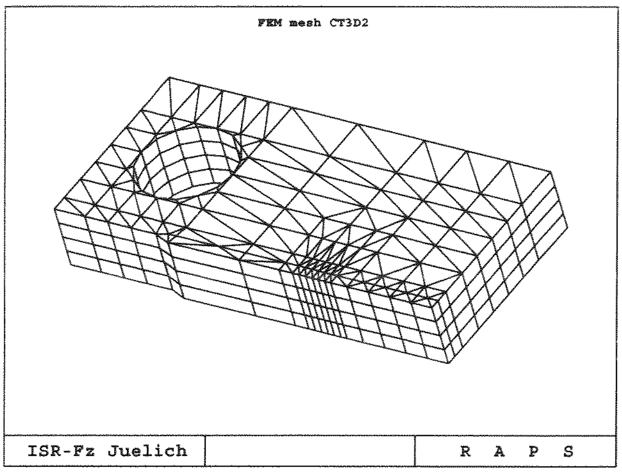

(c) Model CT3D2

Figure 5.5: FEM meshes for the different 2D and 3D models

Figure 5.6 pictures the comparison of the analytical solutions (5.14), (5.16), numerical solutions for model CT3D1, and experiments. Particularly (5.14) appears to be much to low. This is surprising, because (5.14) was obtained in this form as a fit to a series of experiments (with 20 MnMoNi 5 5 and with other steels) [30]. Eq. (5.14) make a close prediction for an ungrooved CT100 specimen [30]. Obviously, the simple eq. (5.14) cannot be matched to a larger parameter range. The discrepancy can be best addressed to the poor approximation of the side grooves by the thickness reduction for 2D formulae and by the choice of lower failure stresses. The comparison with FEM computations for FE-models CT2D1 and CT3D2 without side groove in Table 5.2.1 demonstrates that the formulae make reasonable estimations if R_{p02} and σ_f are replaced by R_m. However, this simple modification is not possible for the experimentally obtained eq. (5.14), because it would then give unsafe predictions for the above CT100 specimen if R_m is used instead of R_{p02}. The computational advantages of the direct LISA approach may support the extended use of realistic 3D modelling with a tendency to increase the number of nodal points and the number of degrees of freedoms (DOFs). Further experimental validations for CT15 and CT100 specimens are presented in [28].

Model	CT2D1	CT2D2	CT3D1	CT3D2	Experiment
AB15	$9880N$	$7020N$	$10210N$	$9130N$	$10700N$
AC18	$21450N$	$15070N$	$21060N$	$18970N$	$22200N$
AC19	$39620N$	$28750N$	$41170N$	$35710N$	$41400N$
AC20	$40100N$	$29100N$	$41100N$	$36600N$	$40200N$

Table 5.6: Results of limit analyses for different FEM-models and experiments

Model	CT2D1	CT3D2	eq. (5.15)	eq. (5.16)
AB15	$9880N$	$9130N$	$9160N$	$8230N$
AC18	$21450N$	$18970N$	$20180N$	$18400N$
AC19	$39620N$	$35710N$	$39670N$	$36950N$
AC20	$40530N$	$37040N$	$41130N$	$38700N$

Table 5.7: Comparison of analytical limit loads with numerical results of limit analyses for specimens $B = 20$, without side grooves with $R_m = 513N/mm^2$ instead of $R_{p0.2} = 379N/mm^2$ and $\sigma_f = 446N/mm^2$

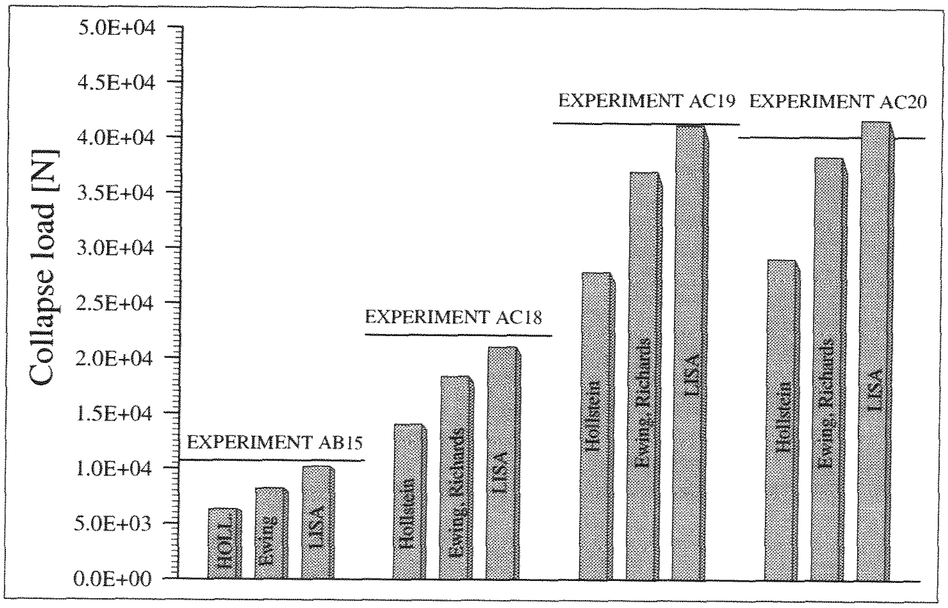

Figure 5.6: Comparison of limit loads of CT3D1 calculated by LISA with analytical solutions and the experiments AB15, AC18, AC19, AC20 (from [52])

5.2.2 R6–method

The specimen AC19 is analyzed exemplary with the R6-method. The stress–intensity factor K_I is given by (see [56]):

$$K_I = F\frac{(2+\frac{a}{W})\left(0.886+4.64\frac{a}{W}-13.32\left(\frac{a}{W}\right)^2+14.72\left(\frac{a}{W}\right)^3-5.6\left(\frac{a}{W}\right)^4\right)}{B\sqrt{W(1-\frac{a}{W})^3}}. \qquad (5.17)$$

The dimensions of the specimen AC19 yield the stress intensity factor K_I:

$$K_I = 0.0914878\, mm^{-3/2}\, F. \qquad (5.18)$$

The material toughness K_{IC} for 20 MnMoNi 5 5 is given by equation (5.13) The plastic limit load calculated with LISA is $F_f = 35790N$ (for $\sigma_f = 0.5(\sigma_y + \sigma_u) = 446N/mm^2$) so that with the definitions (2.6) and (2.12) it holds:

$$\begin{aligned} S_r &= \frac{F}{F_f} = 2.7940\,10^{-5}N^{-1}F \\ K_r &= \frac{K_I}{K_{IC}} = \frac{0.0915}{7851N}F = 1.1655\,10^{-5}N^{-1}F. \end{aligned} \qquad (5.19)$$

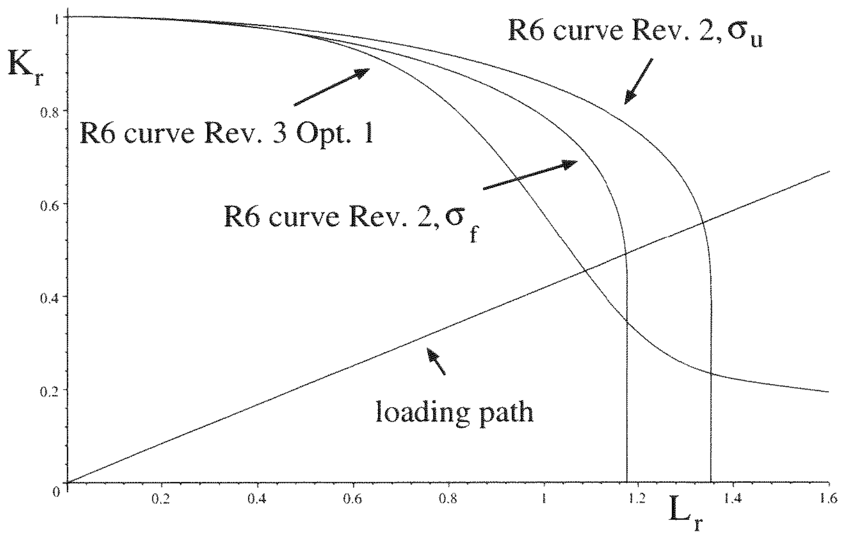

Figure 5.7: Comparison of FAD Rev. 2 and FAD Rev. 3 Opt. 1 (2.13), (2.15)

The assessment-curve (2.13) and the line

$$K_r = \frac{1.1655\,10^{-5}}{2.7940\,10^{-5}}S_r = 0.4171S_r = pS_r, \qquad (5.20)$$

have the intersection S^*

$$S^* = \frac{2}{\pi}\arccos\left(e^{-0.125(\pi/p)^2}\right) = 0.9995, \qquad (5.21)$$

so that the failure load $F_{failure}$ analyzed by the FAD is

$$F_{failure} = S^* F_f = 35772N. \qquad (5.22)$$

The assessment curve with $L_r = 1.1768S_r$ defined by eq. (2.15) and the line

$$K_r = 0.4171S_r = \frac{0.4171}{1.1768}L_r = 0.3545L_r, \tag{5.23}$$

have the intersection $L^* = 1.1264$ (see Fig. 5.7(b)), so that the failure load $F_{failure}$ is

$$F_{failure} = L^* F_y = 34258N. \tag{5.24}$$

Obviously, both assessment curves make over-conservative predictions. This could be changed if hardening was taken fully into account by use of a failure stress $\sigma = \sigma_u$. The derivation of (2.13) suggests that then S_r may simply be replaced by F/F_u. A similar replacement of L_r would need a transformation of the curve (2.15). However, much more experimental and numerical support should be sought, before such changes of FAD are proposed. Current practice may be mis-leading, if limit loads of unknown origin are selected from handbooks and from literature.

6 Benchmarks

The meshes for the following limit load tests [64] have been provided by EDF and ULg and are shared between the partners (FZJ, ULg, EDF and INTES):

LA3: A thick plate (plane strain) with mismatched weld and a centered crack under tension. The main parameter here is the mis-match ratio $M = \sigma_y^W / \sigma_y^B$ of yield stress values of base and weld material. The problem was suggested from the view of the Brite-EuRam project SINTAP [8].

LA4: An axisymmetrical tube with a circumferential crack under pressure and tension. The main loading parameter here is the ratio of tension T and pressure P.

LA5: A pressurized tube with a three-dimensional defect. The main geometrical parameter is the ratio of the mean value for the radius R_m and the thickness of the tube t.

It was decided that the computing times for the direct limit analyses should be compared, in order to learn about the performance of the different methods. The times were made independent on the computing environment by normalizing to the time for an elastic step. Numerical upper and lower bounds were obtained with different software and compared to analytical solutions.

EDF: The upper bound solutions of EDF were calculated with Code_Aster® which is also used for incremental plastic analyses (see [63]). Lower bounds are estimated by a post-processor from the computed upper bounds. By their nature, these estimations may not be close lower bounds.

FZJ: The lower bound solution of FZJ were calculated with a deterministic LISA software which was developped and implemented into PERMAS V4 (Version 4) (see [26], [58], [59]). Fully integrated finite elements are used.

ULg: The benchmark calculations of ULg are carried out by a direct upper bound programming method via the FEM code ELSA. The FEM code SAMCEF is also used for incremental plastic analyses. Under-integrated finite elements and singular crack-tip elements (see Appendix A) are used.

INTES: INTES has contributed some additional incremental analyses of the benchmark tests with PERMAS V7 (Version 7).

The calculations are performed on rectangular meshes. The numerical tests achieved some quite close results. Others exhibited differences which may be perhaps attributed to the used finite elements rather than to the different LISA software. The required computing time is given as multiples of the time for an elastic calculation. This number should be fairly machine independent. But it may contain different computational overheads e.g. from the data handling of the different FE-codes. Particularly the FZJ computations need to be repeated once the software will be implemented into the new PERMAS V7 code. Therefore, both the numerical errors and the relative computing time should be understood as first preliminary indicators.

6.1 LA3 – Plate with mis-matched weld and a centered crack under tension

One half of the thick plate (plane strain) with mis-matched weld has the length $L = 40mm$, the width $W = 4mm$, the crack length $2a = 4mm$, the thickness B and the weld height $h = 1.2mm$, so that $a/W = 0.5$, $h/W = 0.3$ holds (see Fig. 6.1). The different material data of the base material and the weld material are idealized by different yield stresses σ_y^B and σ_y^W, respectively. The main parameter here is the mismatch ratio $M = \sigma_y^W/\sigma_y^B$ of yield stress values of base and weld material. A reference value of the yield stress $\sigma_y^B = 100MPa$.

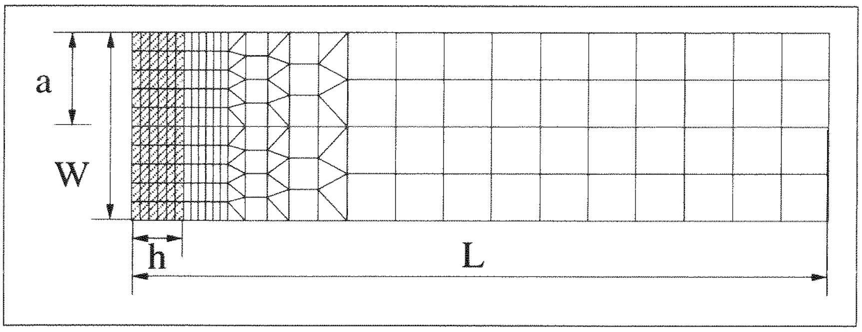

Figure 6.1: FE mesh of benchmark LA3

The test LA3 was quite sensitive and needed some remeshing to improve its numerical results. There are an exact plane stress solution F_{yb} and a plane strain upper bound to the matched situation ($M = \sigma_y^W/\sigma_y^B = 1$) (see ([36]))

$$\underline{\text{plane stress}}: \; F_{yb} = 2B(W-a)\sigma_y^B \qquad \underline{\text{plane strain}}: \; F_{yb} = \frac{4}{\sqrt{3}}B(W-a)\sigma_y^B \tag{6.1}$$

so that the applied line load is $50MPa$ and $57.74MPa$, respectively. Usually no information is given in handbooks when to assume plane stress or plane strain. The latter produces more constraint and thus leads to higher limit loads, which may not be achieved in case of insufficient material ductility. In doubt, the engineer should prefer the more conservative plane stress solution. For the mis-matched situation plane stress and plane strain approximations for limit load F_{ym} are given in [47]. With the abbreviation $\psi = (W-a)/h$ it holds:

1. **<u>Plane stress:</u>**

Undermatched ($M < 1$):

$$\frac{F_{ym}}{F_{yb}} = \begin{cases} M & \text{for } 0 \leq \psi \leq 1.43 \\ \min\left\{F^{(1)}, 1-(1-M)\frac{1.43}{\psi}\right\} & \text{for } \psi \geq 1.43 \end{cases} \tag{6.2}$$

$$F^{(1)} = M\left[\frac{2}{\sqrt{3}} - \left(\frac{2-\sqrt{3}}{\sqrt{3}}\right)\frac{1.43}{\psi}\right]$$

Overmatched $(M > 1)$:

$$\begin{aligned}
\frac{F_{ym}}{F_{yb}} &= \min\left\{F^{(2)}, \frac{W}{W-a}\right\} \\
F^{(2)} &= \begin{cases} M & \text{for } \psi \leq \psi_l \\ \frac{24(M-1)}{25}\frac{\psi_l}{\psi} + \frac{M+24}{25} & \text{for } \psi \geq \psi_l = \left[1 + 0.43e^{-5(M-1)}\right] e^{-(M-1)/5} \end{cases}
\end{aligned} \tag{6.3}$$

2. **Plane strain:**

Undermatched $(M < 1)$:

$$\begin{aligned}
\frac{F_{ym}}{F_{yb}} &= \begin{cases} M & \text{for } 0 \leq \psi \leq 1 \\ \min\left\{F^{(3)}, 1-(1-M)\frac{1}{\psi}\right\} & \text{for } \psi \geq 1 \end{cases} \\
F^{(3)} &= \begin{cases} M\left[1.0 + 0.462\frac{(\psi-1)^2}{\psi} - 0.044\frac{(\psi-1)^3}{\psi}\right] & \text{for } 1.0 \leq \psi \leq 3.6 \\ M\left[2.571 - \frac{3.254}{\psi}\right] & \text{for } 3.6 \leq \psi \leq 5.0 \\ M\left[0.125\psi + 1.291 + \frac{0.019}{\psi}\right] & \text{for } 5.0 \leq \psi \end{cases}
\end{aligned} \tag{6.4}$$

Overmatched $(M > 1)$:

$$\begin{aligned}
\frac{F_{ym}}{F_{yb}} &= \min\left\{F^{(4)}, \frac{W}{W-a}\right\} \\
F^{(4)} &= \begin{cases} M & \text{for } \psi \leq \psi_1 = e^{-(M-1)/5} \\ \frac{24(M-1)}{25}\frac{\psi_1}{\psi} + \frac{M+24}{25} & \text{for } \psi \geq \psi_1 = e^{-(M-1)/5} \end{cases}
\end{aligned} \tag{6.5}$$

The first incremental analyses by INTES showed a tendency to overestimate the limit loads for the rather sensitive LA3 plane strain problems. This tendency to generate unsafe solutions could be reduced to some extent by choosing underintegrated finite elements (by choosing 8 nodes elements with 2x2 instead of 3x3 Gaussian integration points). This is a well-known consequence of incompressibility for the fully plastic plane strain solution (see [42], [32], [67]). The fully integrated displacement finite elements cannot properly handle incompressible deformation. When plastic strains become extremely large and the response becomes nearly incompressible, numerical difficulties associated with locking of the elements can occur. Additionally, the elements behave too stiff in the fully plastic range and the limit load may be overestimated. Satisfactory analyses could be performed by using reduced integration in conventional elements, which relieve the excess constraint of fully integrated elements. However, the fully integrated elements are usually preferred, because they are often reported to be more reliable away from the collapse situation. For this FE model a need remains to discuss this sensitivity and the best recommendations to be given to end-users.

Because of the non–availability of rectangular plane strain elements in PERMAS V4 the FZJ calculations are done for plane stress by rectangular elements (and transformed by an approximation) and additionally for plane strain by triangular elements. Both are fully integrated elements. The tendency to overestimate

LA3: Thick plate with centered crack in mis-matched weld under tension					
$M = \sigma_y^W / \sigma_y^B$	0.50	0.75	1.00	1.25	1.50
analytic solution [47]	32.33	47.92	57.74	65.82	73.33
EDF lower bound	29.71	42.25	50.31	57.96	64.71
EDF upper bound	36.04	50.40	61.71	70.59	78.38
equiv. number of elast. calc.	100	89	62	52	55
10 steps FZJ rectangular	28.99	43.86	56.90	68.99	77.07
equiv. number of elast. calc.	43	45	47	47	48
FZJ triangular lower bound	33.16	49.74	60.38	68.21	75.55
ULg upper bound	35.68	49.48	59.79	69.05	77.89
equiv. number of elast. calc.	40	40	40	40	40
incr. INTES 3×3 Gauss P.	38.22	52.82	63.08	71.64	79.24
incr. INTES 2×2 Gauss P.	35.02	50.30	61.02	69.32	76.80

Table 6.1: Comparison of limit loads (in N/mm^2) for LA3

was smaller with the direct limit analysis. EDF uses a mixed finite element formulation for direct limit analysis and underintegrated elements for incremental analysis. The latter are also used by ULg.

For the test LA3 it is observed, that the main difficulty (of convergence) is not the heterogeneous aspect, but the localization of the collapse mode, because in 2D-plane strain situation shear bands appear. The lower bounds from the EDF post-processor tend to be somewhat low.

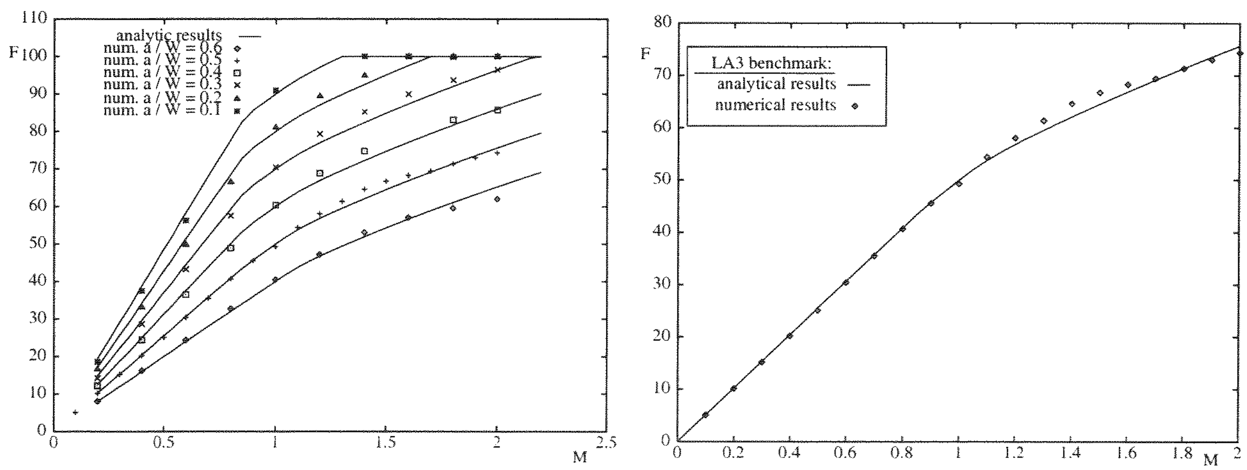

(a) $a/W = 0.1, \ldots, 0.6$, $h/W = 0.3$ (b) $a/W = 0.5$

Figure 6.2: Comparison of numerical and analytical results (eq. (6.2) of limit load for different crack length and mismatch factors $M = \sigma_y^W / \sigma_y^B$ for plane stress, $h/W = 0.3$

In Fig. 6.2(a) and (b) analytical (eq. (6.2), (6.3)) and numerical results for plane stress are compared. The limit load is calculated for different values of mismatch factor $M = \sigma_y^W / \sigma_y^B$. For undermatching the numerical and analytical results in Fig.6.2(b) are in very good agreement (at most 2 % error). In low overmatching case the numerical results differ from the analytical results at most by 4 %.

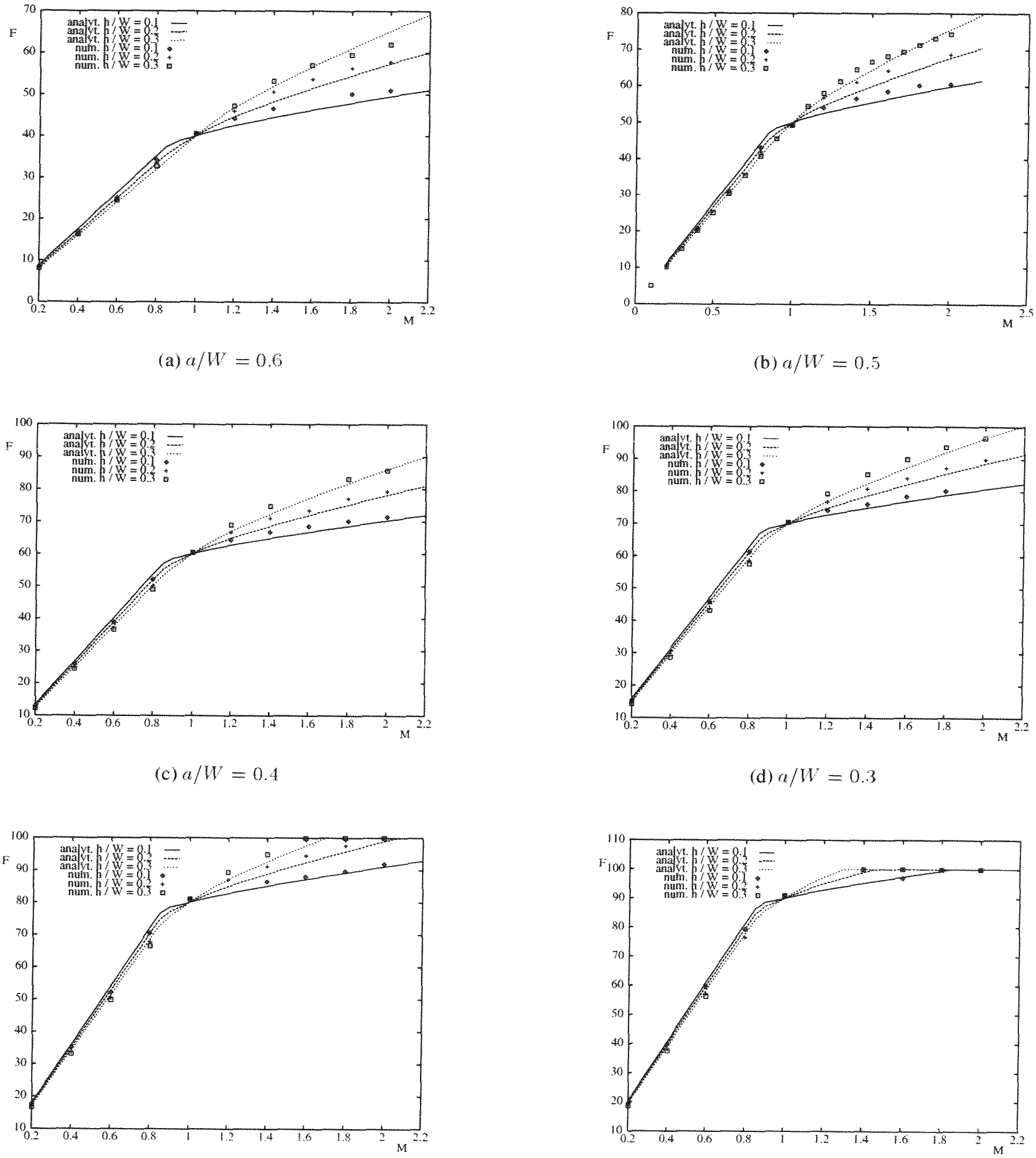

(a) $a/W = 0.6$

(b) $a/W = 0.5$

(c) $a/W = 0.4$

(d) $a/W = 0.3$

(e) $a/W = 0.2$

(f) $a/W = 0.1$

Figure 6.3: Comparison of numerical and analytical results for different values of weld thickness, mismatch factors $M = \sigma_y^W / \sigma_y^B$, and crack lengths factors a/W, plane stress.

In Fig. 6.4(a)–6.4(d) contour lines for the overmatched case in plane stress state are shown (see [26]). The plate fails by joining of the plastified regions in the base and the weld material. The pictures are generated by an incremental analysis. In the undermatched case Fig. 6.5(a)–6.5(d) the plate fails by plastification of

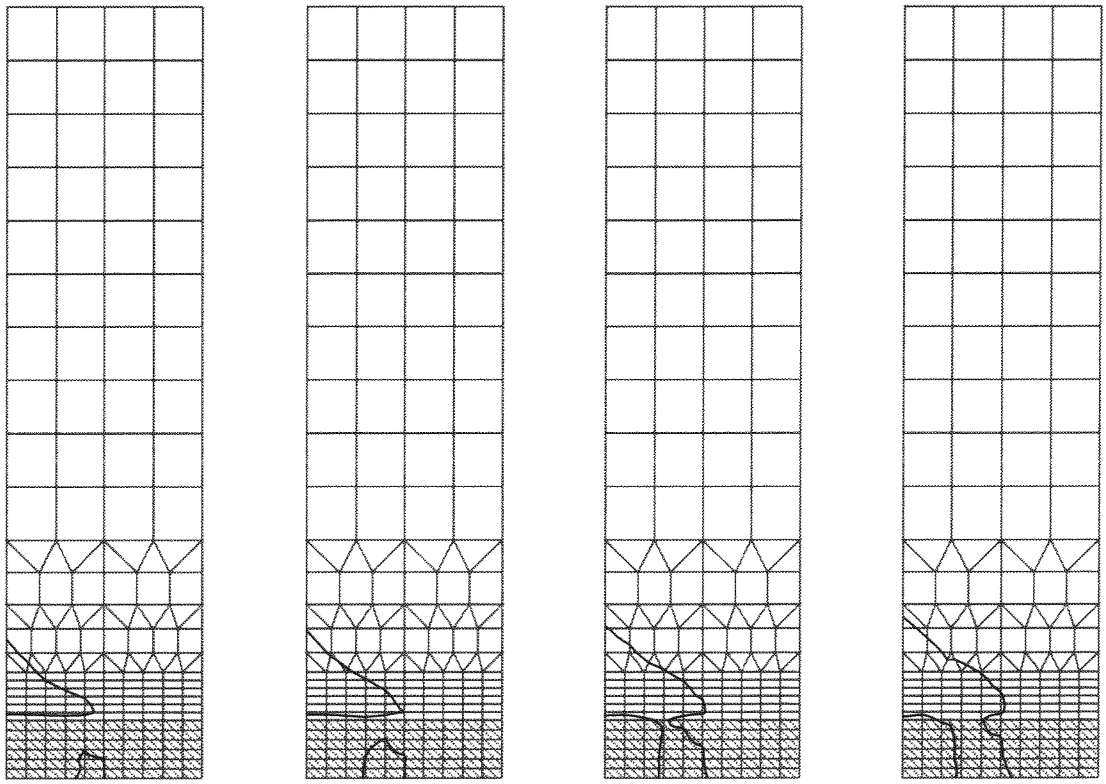

(a) $P/P_{elast} = 1.23$ (b) $P/P_{elast} = 1.27$ (c) $P/P_{elast} = 1.32$ (d) $P/P_{elast} = 1.36$

Figure 6.4: Yield contour line for overmatched material case $\sigma_y^W/\sigma_y^B = 1.5$, [26]

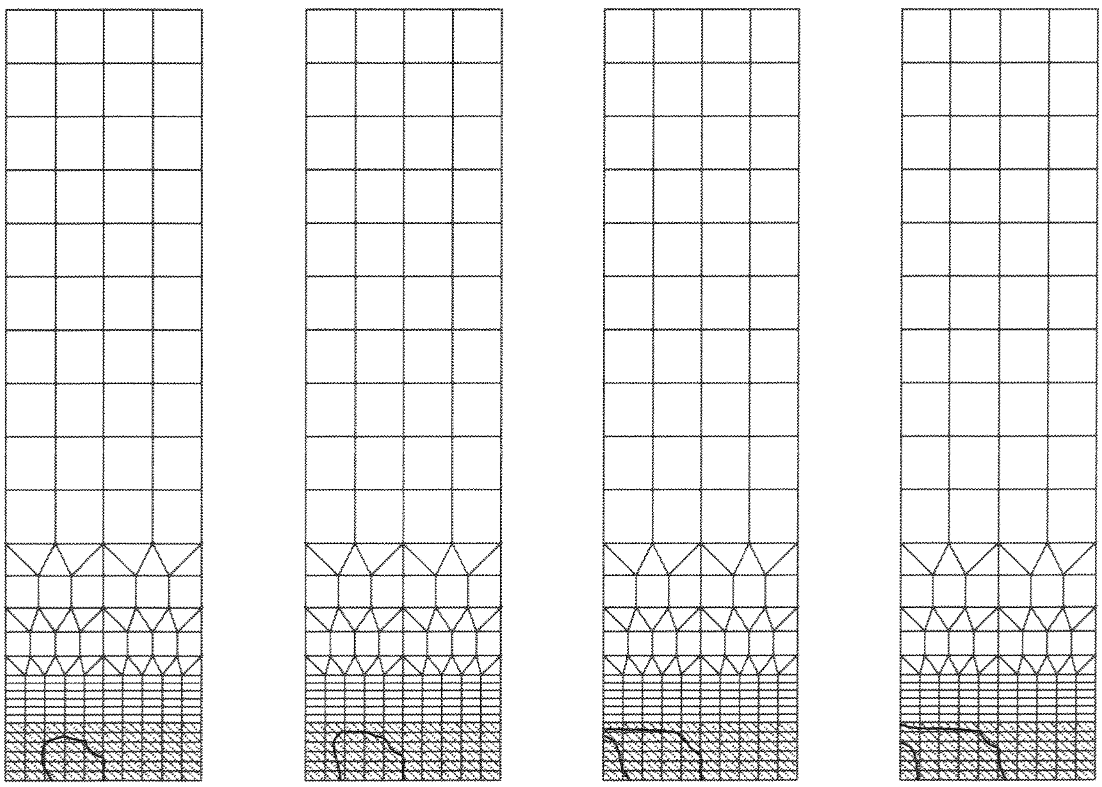

(a) $P/P_{elast} = 0.70$ (b) $P/P_{elast} = 0.73$ (c) $P/P_{elast} = 0.75$ (d) $P/P_{elast} = 0.77$

Figure 6.5: Yield contour line for undermatched material case $\sigma_y^W/\sigma_y^B = 0.75$, [26]

the ligament in the weld, so that the limit load is dominated by the yield stress of the weld material σ_y^W.

6.2 LA4 – Axisymmetrical tube with a circumferential crack under pressure and tension

An axisymmetrical tube with a circumferential internal crack subjected to pressure and tension is analyzed. The dimensions of the model are shown in Fig. 6.6. The outer radius is $R_o = R_i + t$. The axisymmetrical FE–mesh has 282 elements. With the loading direction parameter $\kappa, \kappa \in [0;1]$ the loading vector is defined by

$$\boldsymbol{F} = \alpha \begin{pmatrix} \kappa F \\ (1-\kappa)P \end{pmatrix}. \tag{6.6}$$

The limit load factor α is computed for different values κ to determine the admissible (F, P) domain. It is shown that there are no significant differences in the limit load results for the different boundary conditions for open or closed tubes. Pressurizing the crack surface has no significant influence on the limit load [26].

The obtained numerical results in come near to the analytical simplified lower bound, proposed by EDF (see Appendix B). If tension dominates the differences between the FEM solutions are very small. But the analytical solution seems to be too low for pure tension ($\kappa = 1$) if compared to FEM results.

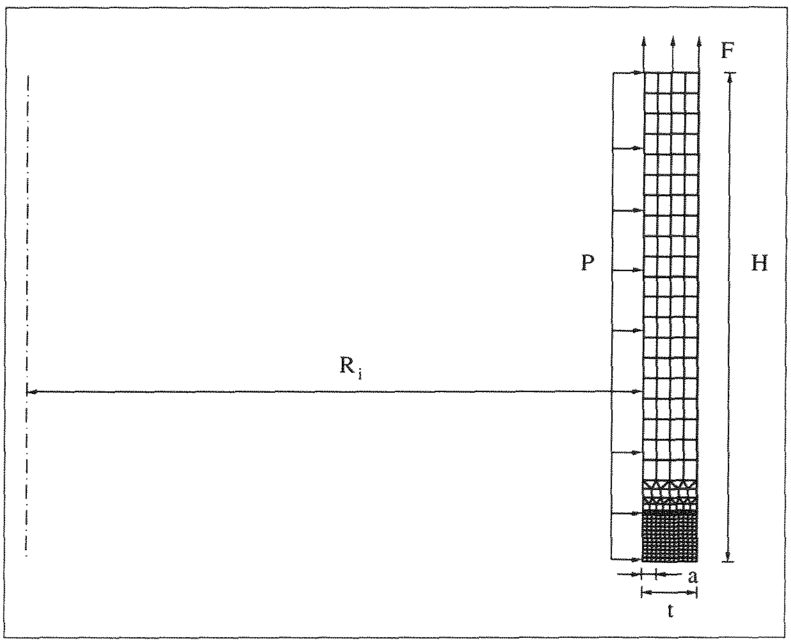

R_i	=	$400\ mm$
R_o	=	$440\ mm$
H	=	$378\ mm$
t	=	$40 mm$
a	=	$10\ mm$

Figure 6.6: FE–mesh and dimensions of LA4

In the pure tension case a simple analytical solution is obtained [36]. The cross-section of the uncracked pipe is $\pi(R_o^2 - R_i^2)$. For the cracked pipe the ligament area is $\pi(R_o^2 - (R_i + a)^2)$. With the constraint $L = \alpha = 2/\sqrt{3} = 1.1547$ a lower bound of the limit in pure tension F_y is

$$F_y = \frac{2}{\sqrt{3}} \frac{\text{ligament area}}{\text{pipe area}} \sigma_y = \frac{2}{\sqrt{3}} \frac{(R_o)^2 - (R_i + a)^2}{(R_o)^2 - R_i^2} \sigma_y. \tag{6.7}$$

This constrained solution may not be used for shallow cracks [9] with $a \leq t/(1 + \sqrt{3})$, because it does not converge to the uncracked limit $F_y = \sigma_y$ for $a \to 0$. Upper bound limit analysis may be approximated by [65]

$$F_y = \frac{(R_o)^2 - (R_i + a)^2}{(R_o)^2 - R_i^2} \sigma_y \begin{cases} 1 + 0.76\frac{a}{t} & \text{for } a/t < 0.25 \\ 1.19 & \text{for } a/t \geq 0.25 \end{cases} \tag{6.8}$$

With the contraint in (6.7) the analytical limit tension is $F_y \approx 0.8763\sigma_y$ for the dimensions shown in Figure 6.6. For the yield stress 100 N/mm^2 the limit tension is $F_y = 87.63 N/mm^2$.

Obviously, the proposed analytical solution is an unconstrained lower bound (see also Appendix B). No analytical solution for the tube under pressure with open end conditions, i.e. $F = 0$ is known for VON MISES material. Modifications of the EDF formula will be considered in future research.

LA4: Axisymmetrical tube with circumferential crack under combined tension and pressure								
	F/P	0.00	0.25	1.00	4.00	9.00	19.00	∞
	κ	0.00	0.20	0.50	0.80	0.90	0.95	1.00
anal. EDF	F_y	0.00	2.31	9.61	41.98	77.52	84.50	75.89
	P_{lim}	9.09	9.23	9.61	10.49	8.61	4.45	0.00
incr. EDF	F_y	0.00	–	10.17	–	86.43	87.40	86.27
	P_y	9.75	–	10.17	–	9.60	4.60	0.00
inf. EDF	F_y	0.00	2.46	9.82	41.33	78.70	80.17	85.79
	P_y	9.41	9.50	9.82	10.33	8.74	4.22	0.00
sup. EDF	F_y	0.00	2.37	10.17	43.82	88.81	94.48	90.34
	P_{lim}	9.75	9.86	10.17	10.96	9.87	4.97	0.00
equiv. number of elast. calc.		14	11	11	13	18	–	44
10 steps FZJ	F_y	0.00	2.46	10.13	43.42	86.33	89.80	87.09
	P_y	9.74	9.85	10.13	10.85	9.59	4.73	0.00
equiv. number of elast. calc.		44	51	56	61	58	58	56
incr. ULg	F_y	0.00	2.46	10.17	43.82	88.82	91.38	91.80
	P_y	9.75	9.86	10.17	10.95	9.87	4.81	0.00
sup. ULg	F_y	0.00	2.46	10.15	43.70	88.01	89.41	89.68
	P_y	9.74	9.84	10.15	10.93	9.78	4.71	0.00
equiv. number of elast. calc.		40	40	40	40	40	40	40
incr. INTES	F_y	0.00	2.46	10.11	43.72	88.04	91.22	90.25
	P_y	9.65	9.83	10.11	10.93	9.78	4.80	0.00

Table 6.2: Comparison of limit analysis results (in N/mm^2) for LA4

From the plane strain solution for the pressurized long tube one may deduce in the absence of cracks:

$$P_*^{lim} = \frac{2\sigma_y}{\sqrt{3}} \ln\frac{R_o}{R_i} = 11.00 N/mm^2. \tag{6.9}$$

Plane strain is maintained by a tension $F(R)$, which varies over the tube cross-section [62]. However, its mean value is equivalent to the tension F in a tube with closed ends, i.e.

$$F_*^{lim} = \frac{R_i^2}{R_o^2 + R_i^2} P_*^{lim} = 52.41 N/mm^2. \tag{6.10}$$

Therefore the LA4 results near

$$F_*^{lim}/P_*^{lim} = \frac{R_i^2}{R_o^2 + R_i^2} = 4.76 \tag{6.11}$$

could be compared to limit loads of cracked pressurized tubes with sealed cracks. The solution for the situation with crack face pressure in [9] is $P^{lim} = 9.50N/mm^2$.

6.3 LA5 – Pressurized tube with a semi-elliptical flaw

For the test LA5 the results of the partners are in good agreement for 3D cases ($\theta = \pi/4$) and for 2D ones ($\theta = 2\pi$), respectively. INTES observed a severe problem with the incremental analyses of the 3D models, because the aspect ratios of some elements reach 1/80, which destroys the accuracy of the solution. Therefore, no useful balance forces were available and no iteration could be performed.

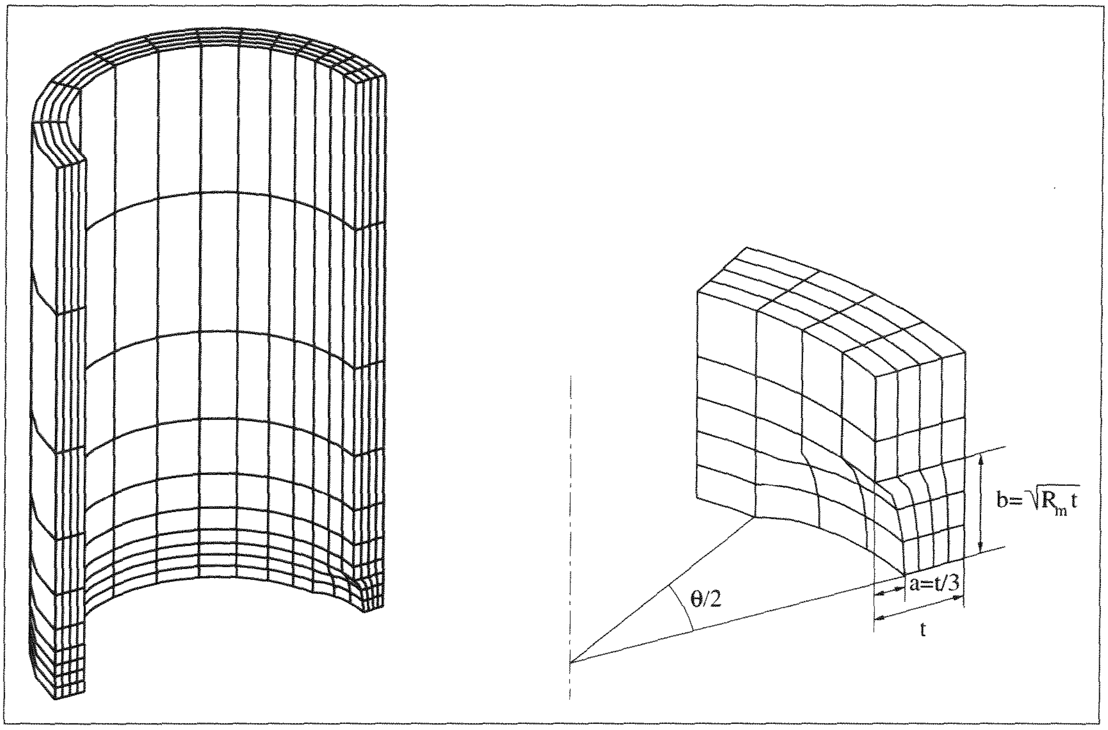

Figure 6.7: FE mesh of benchmark LA5

In 3D also ULg observed an one order of magnitude increase of computing time in incremental analyses. The incremental analyses by ULg were quite effective in 2D. There was no problem for the direct limit analyses by EDF (the calculations were extremely inexpensive), FZJ, and ULg. INTES suggests to make new meshes with aspect ratios of up to about 1/10, although this would increase the number of DOFs and thus the required computing resources.

LA5: Pressurized tube with a semi-elliptical flaw	3-dim. $R_m/t = 5$ $\theta = \pi/4$	3-dim. $R_m/t = 20$ $\theta = \pi/4$	2-dim. $R_m/t = 5$ $\theta = 2\pi$	2-dim. $R_m/t = 10$ $\theta = 2\pi$	2-dim. $R_m/t = 20$ $\theta = 2\pi$
anal. inf. EDF	20.99	5.12	20.99	10.51	5.12
inf. EDF	20.54	5.24	20.32	10.09	4.85
sup. EDF	22.98	5.75	21.12	10.66	5.13
equiv. number of elast. calc.	5	4	4	5	6
10 steps FZJ	21.02	5.32	21.30	10.50	5.33
equiv. number of elast. calc.	48	53	55	40	51
incr. ULg	22.65	5.66	21.62	10.82	5.42
equiv. number of elast. calc.	259	546	51	19	19
sup. ULg	–	–	21.52	10.64	5.13
equiv. number of elast. calc.	–	–	20	20	20
incr. INTES	–	–	21.40	10.62	5.23

Table 6.3: Comparison of collapse pressures (in N/mm^2) for LA5

7 Elastic-plastic J-Integral and the failure assessment diagram (R6 FAD curve) of mis-matched welded plate

We will use an elastic–perfectly plastic material model to establish R6 curve of a plate with mis-matched weld and centred crack by an incremental finite element analysis. $S_r = L_r$, because no hardening is assumed. This is to investigate the strength mis-match effect on the R6 curve in a perfectly plastic material model. This provides also a complementary to previous work with elastic plastic hardening model.

7.1 Elastic plastic J–integral and its path–independence

When the load–displacement curve displays a non-linear behaviour, the fracture toughness could be measured through the J-integral introduced in [44]. In 2D crack problem, it is represented as contour integral along the closed path Γ around the crack-tip:

$$J = \int_{\Gamma} (U n_1 - \sigma_{ij} n_j \partial u_1) d\Gamma \qquad \text{with} \qquad U = \int \sigma_{ij} d\varepsilon_{ij}. \tag{7.1}$$

The numerical implementation of elastic-plastic J-integral could be realized by different methods. Several J-calculating methods are available in software SAMCEF, such as the classical methods VCE (Virtual Crack Extension method) and EDI (Equivalent Domain Integral method, [38]). The EDI method is used in the present calculations because of its good precision and stability in both elastic and plastic fracture analysis. We chose different integral contours around the crack-tip to verify path-independence. The results from first layer of crack-tip elements are rejected due to their instability.

We investigate the homogeneous material model first. Fig. 7.1 shows the J-integral obtained by different contours for the structure near perfectly elastic, elastic plastic and near to plastic limit state, respectively. From the obtained numerical results, the J-integral on the second contour of first crack-tip element is unstable. However, beyond the first layer element it is almost path-independent. Specially in nearly elastic state ($P/P_l < 30\%$) and final plastic limit state, the difference among different contours is less than 2%. However, there is an unstable region near to the finial limit state. Beside this small unstable region, Fig. 7.1 shows the maximum relative difference with different contour arrives when the applied load approaches to 90% of load limit but always not important.

In mis-matched material models (see Fig. 7.3, 7.4) we have still good path-independence of the J integral. Small difference is that the maximum relative difference of J on various contours reaches at $P/P_l = 0.8$ for under-matched model but it is at $P/P_l = 0.97$ for overmatched model. So we know generally that mismatched material model has a path-independence of the J-integral similar to homogeneous material.

It is known that stress intensity factor K_I is proportional to applied load P (or σ). So equivalent J-integral is proportional to P^2. However, in fully plastic regime, J^p is proportional to P^{n+1} for a n-power hardening material. Specially for perfectly plastic material model ($n \to \infty$), J is very sensitive to load, as shown in Fig. 7.5. Accurate estimates of applied J at load-controlled model is virtually impossible when load approaches limit load. However, it may be well approximated in displacement-controlled loading situation.

Approximate limit load solutions for various mis-matched material models have been given in [35], [46]. Our finite element examination shows that this approximate solution has enough precision and no further correction is necessary. The comparison is presented in Table 7.1 where we take the following value as reference:

$$p_o^{1.0} = \frac{2\sigma_y^B}{\sqrt{3}} \frac{a}{W} \tag{7.2}$$

σ_y^W/σ_y^B	0.5	0.75	1.0	1.25	1.5	Note
$p_l/p_o^{1.0}$	0.56	0.83	1.0	1.14	1.27	Analytic [35]
$p_l/p_o^{1.0}$	0.566	0.8325	1.004	1.1496	1.277	887 Finite Elements*

* 4 special strain singular elements as stated in 4 are used around crack tip

Table 7.1: Limit load solution of mis-matched welded plate (plane strain) ($a/W = 0.5$)

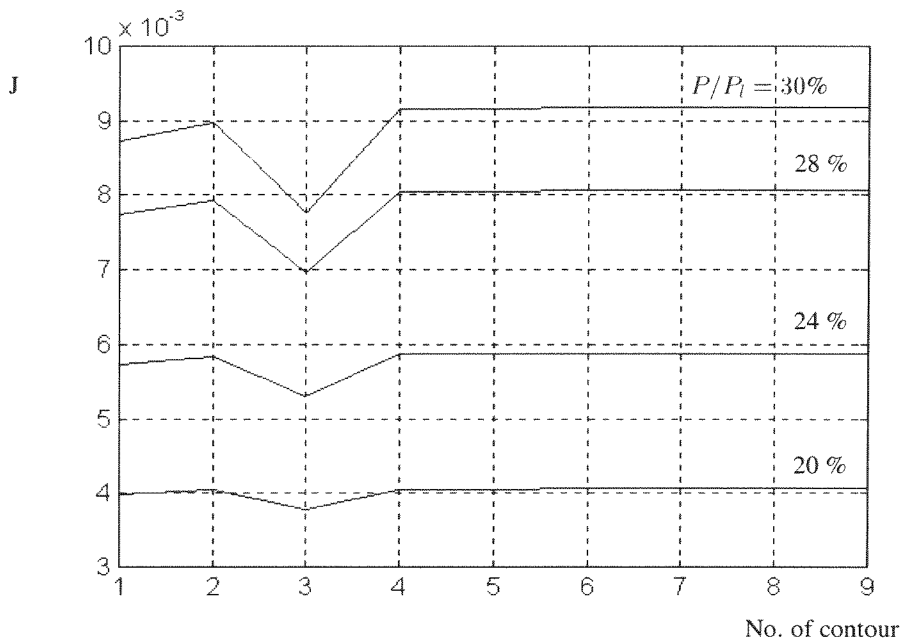

Figure 7.1: a) Path independence of J (loading up to 30% of limit load)

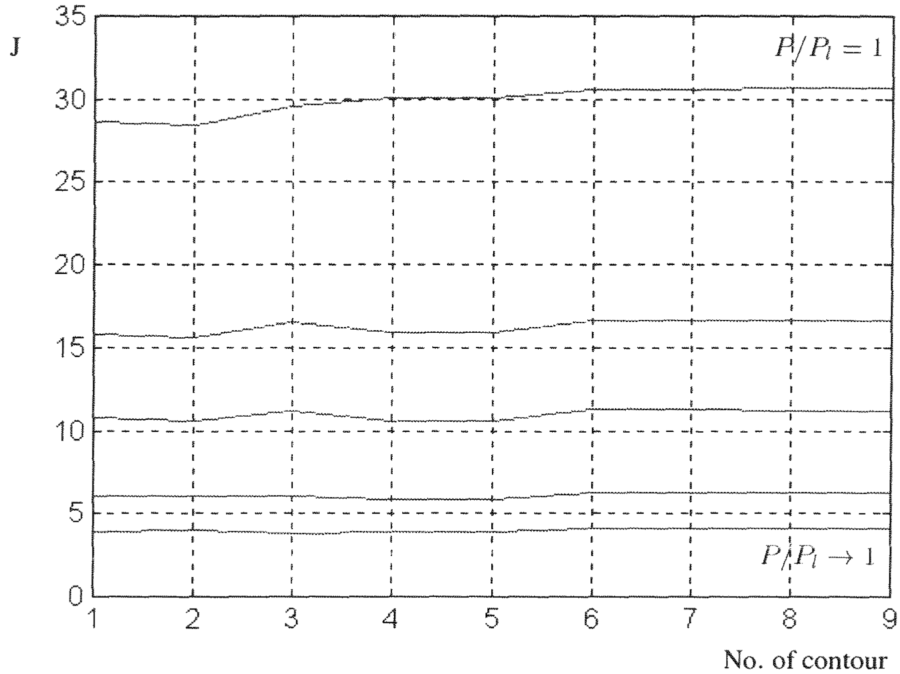

Figure 7.1: b) Path independence of J (last loading steps at nearly limit load)

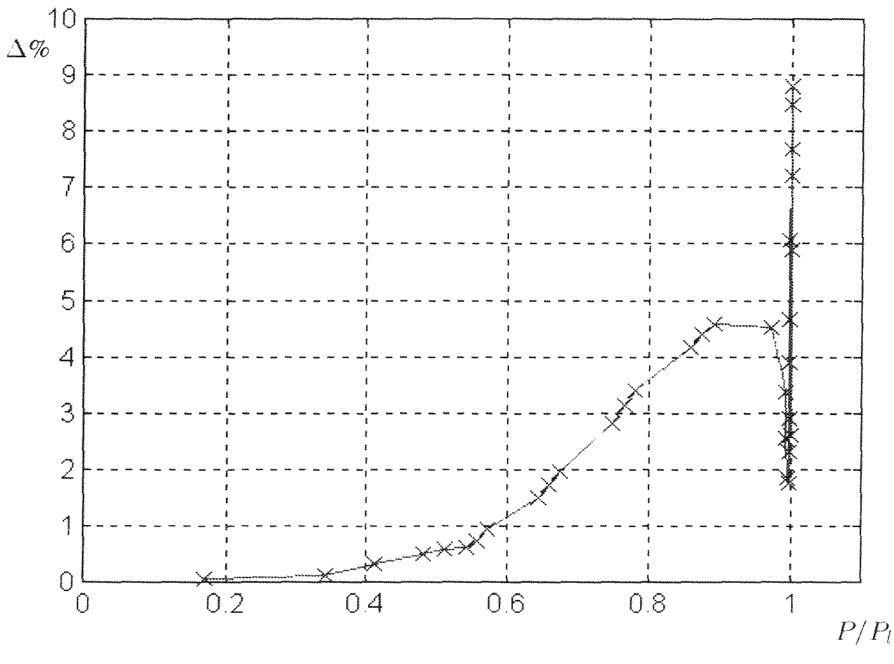

Figure 7.2: Maximum relative difference Δ of J integral on contours in all loading levels (homogeneous material $\sigma_y^W/\sigma_y^B = 1$)

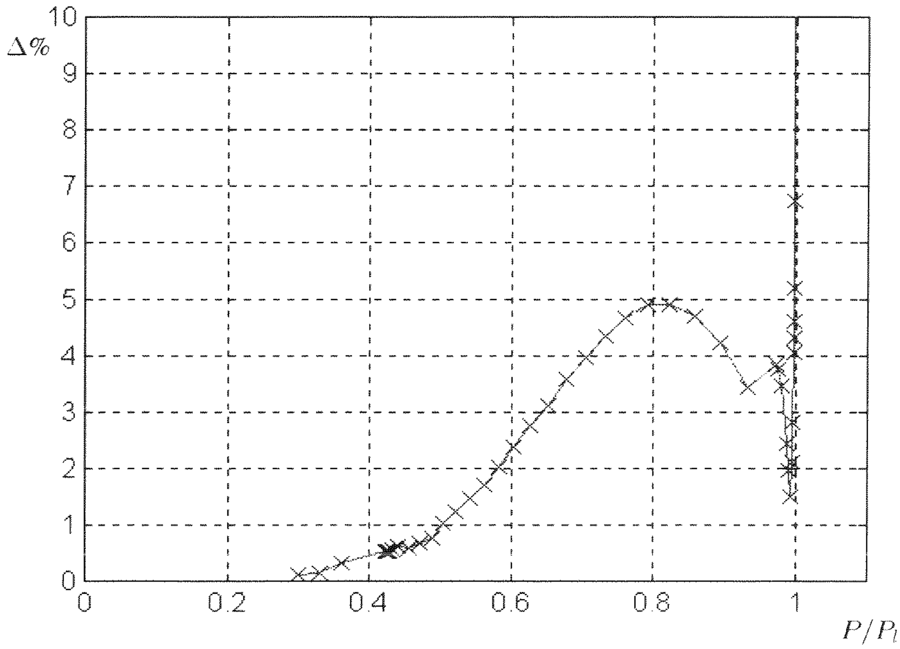

Figure 7.3: Maximum relative difference Δ of J integral on contours in all loading levels (undermatched material $\sigma_y^W/\sigma_y^B = 0.5$)

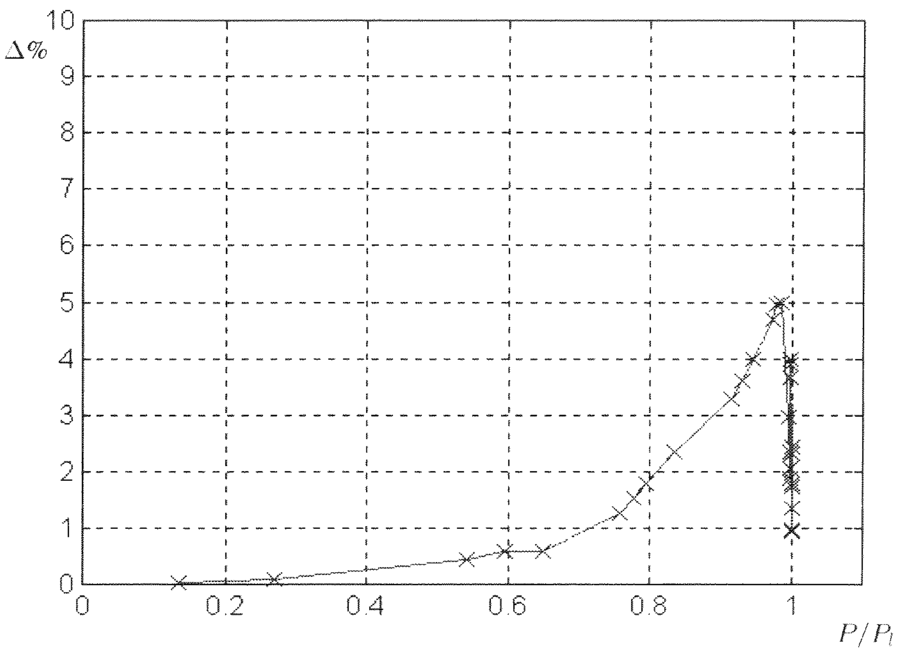

Figure 7.4: Maximum relative difference Δ of J integral on contours in all loading levels (overmatched material $\sigma_y^W/\sigma_y^B = 1.5$)

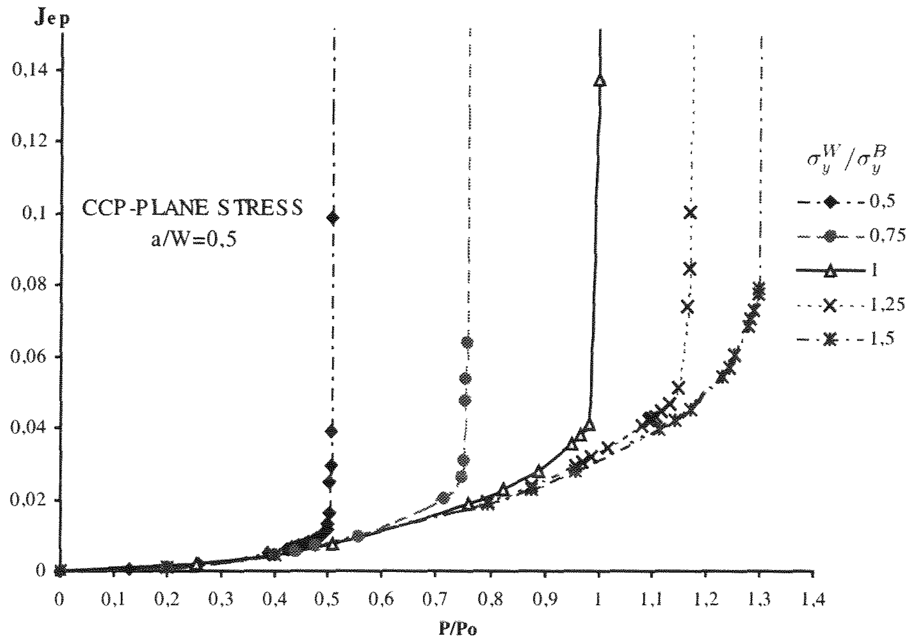

Figure 7.5: Integral J as function of load level (CCP-Plane stress state)

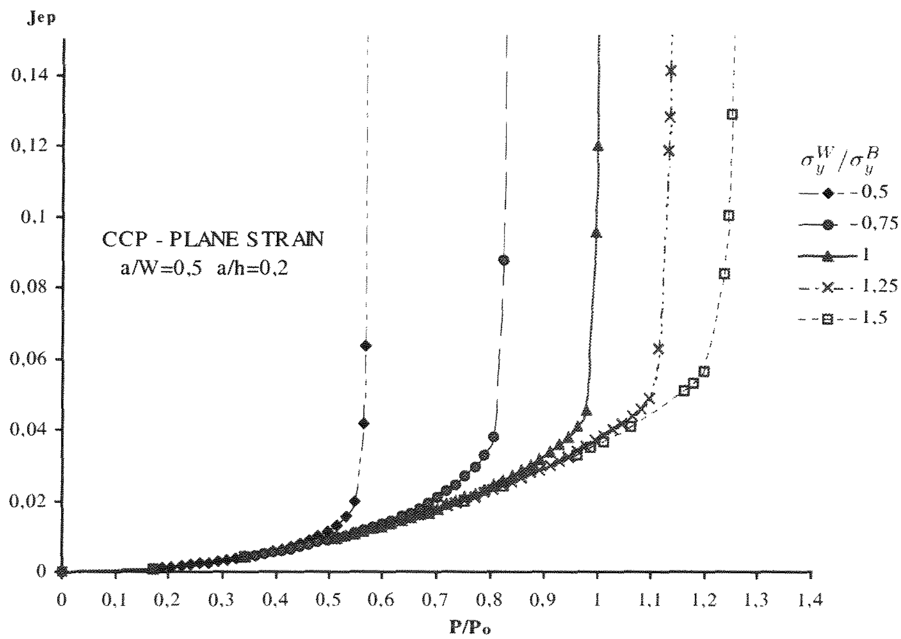

Figure 7.6: Integral J as function of load level (CCP-Plane strain state)

7.2 R6 Curves by elastic perfectly plastic finite element calculation

We consider first a center cracked plate in plane stress with homogeneous material. In Fig. 7.7 we compare the results between the theoretical R6 curve Eq.(2.13), approximate equation Eq. (2.15), the finite element solution with elastic perfectly plastic model, and Kumar et al. [36] with power hardening model. We see that with power hardening model a tail remains in the diagram where the assessment line approaches the L_r abscissa asymptotically. This tail has been suggested to be cut with different material. When hardening power n increases, failure assessment curve should approach to present elastic perfectly plastic model ($n \to \infty$). However, this does not happen for $L_r < 1$: present results with elastic perfectly plastic model is among that of hardening model of Kumar et. al. [36]. However, if we use flow limit of material instead of initial yield limit. Finite element solution will approach the theoretical one (when $S_r < 1$). On the other hand for strong hardening model ($n \to 1$), the curve approaches to the theoretical one of R6 when $S_r < 1$. Anyway, for this geometry, R6 (2.13) represents a lower bound for different material models.

The difference between plane stress and plane strain are noticed in both elastic - perfectly plastic model and power hardening one, see Fig. 7.8. Since R6 curve is based on a infinite plate, the finite element simulation of a small crack plate is nearer to the theoretical one of R6 than a large crack plate. This has be certified by Kumar et al. [36].

Now we consider the mis-matched material model. As example, we fix the parent metal having constant yield strength of $\sigma_y^B = 100$ Mpa with different weld strength σ_y^W. With a similar calculation as above, we could constitute a FAD with elastic perfectly plastic material model as Fig. 7.9 and Fig. 7.10.

It is seen that all FAD of mis-matched model have similar form. In plane stress condition the effect of mis-matched material model seems small. On the contrary, in plane strain this effect is not negligible. The undermatched weld plate (weld material has a lower strength than parent material) give a lower FAD curve although it is still over theoretical R6 curve. In fact in such situation the plasticity is more concentrated in cracked region. Therefore it may lead to be non-conservative even unsafe in some cases to carry out a safety assessment by using a FAD curve of usual homogeneous material for undermatched structures. To avoid this risk it has usually been recommended that the tensile property of the "weaker" material should be used for the evaluation of integrity for undermatched structures. The strength mismatch was a major task of the SINTAP project [73]). Much progress has been achieved which could not be considered here.

7.3 The load-dependence of η–factor of center cracked plate with mis-matched model

Limit load solutions could be used to find η factor that is useful in the estimation of fracture toughness of material. For mis-matched weld plate with centre crack under tension, Joch et. al. have provided an approximate analytic solution of limit load [35], [46]. Starting from this solution η factors for different mis-matched model are obtained and the solutions are examined by finite element calculation. However, our work shows the η factors obtained by Joch et al. seems not usable. In fact these factor are shown to be load-dependent.

Plastic η_{pl} factor may be defined by plastic collapse load solution:

$$\eta_{pl} = \frac{-1}{F_l}\frac{\partial F_l}{\partial a}l \tag{7.3}$$

By analytic limit load functions, Joch et al. [35] gave solutions η_{pl}. In the case of homogeneous material

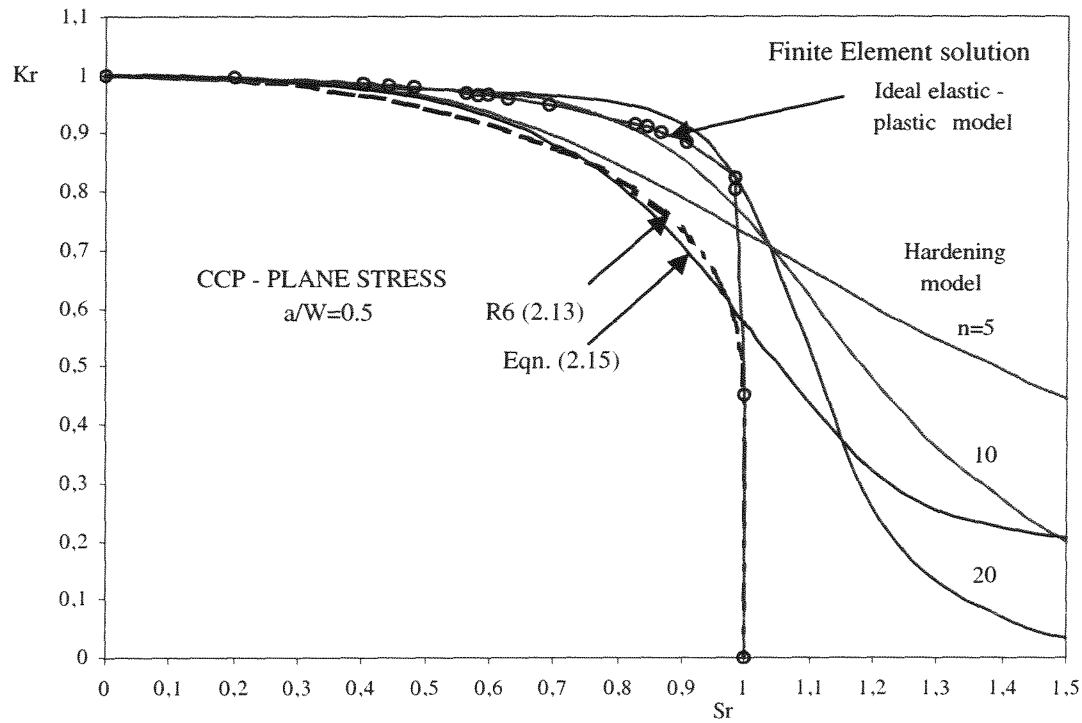

Figure 7.7: FAD of CCP specimen with different material models, for hardening material taken from [36], $M = 1$

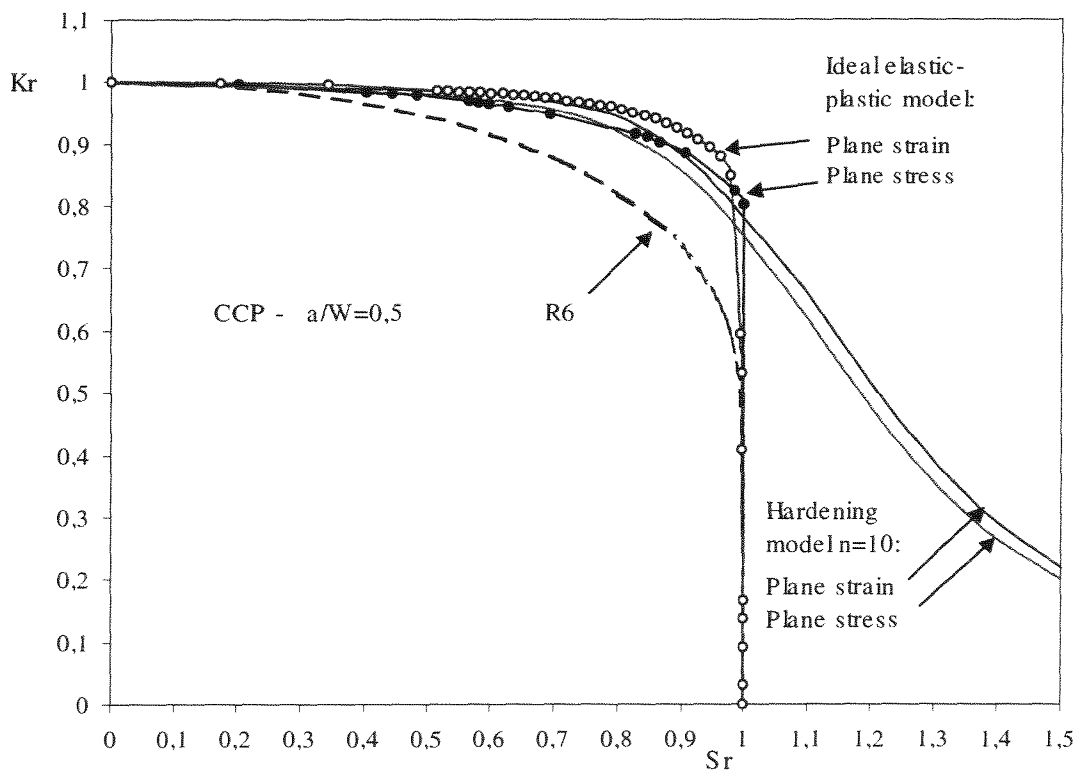

Figure 7.8: FAD of CCP specimen in plane stress or plane strain, curves for hardening material taken from [36], $M = 1$

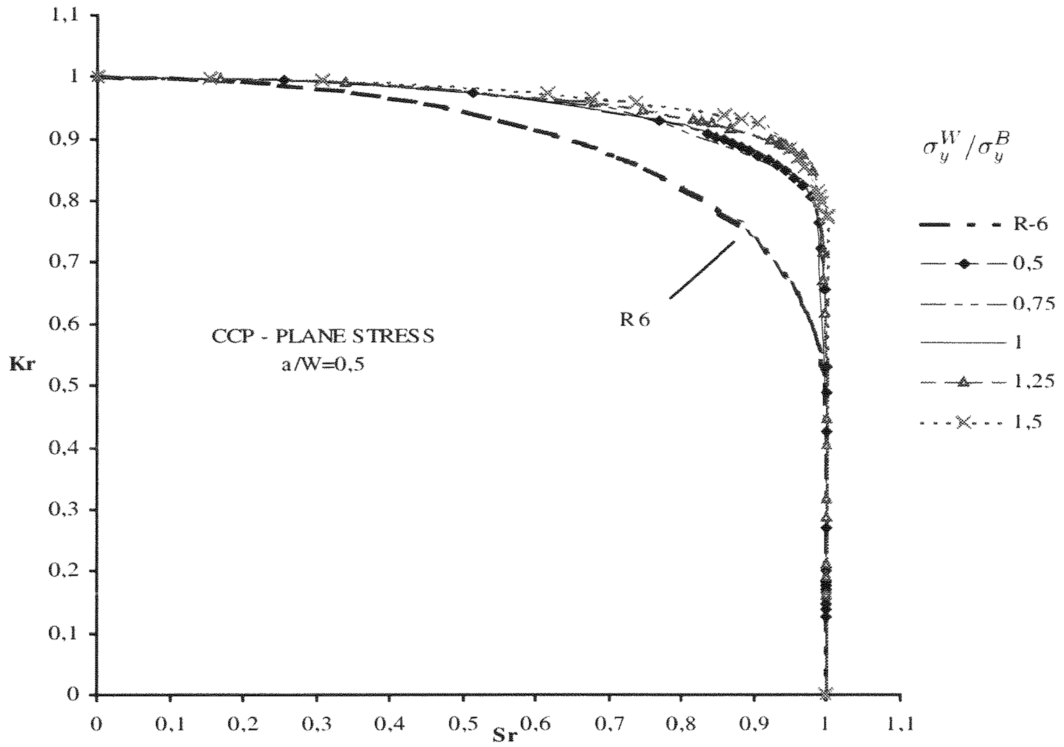

Figure 7.9: FAD of CCP weld plate (plane stress)- mismatched material model

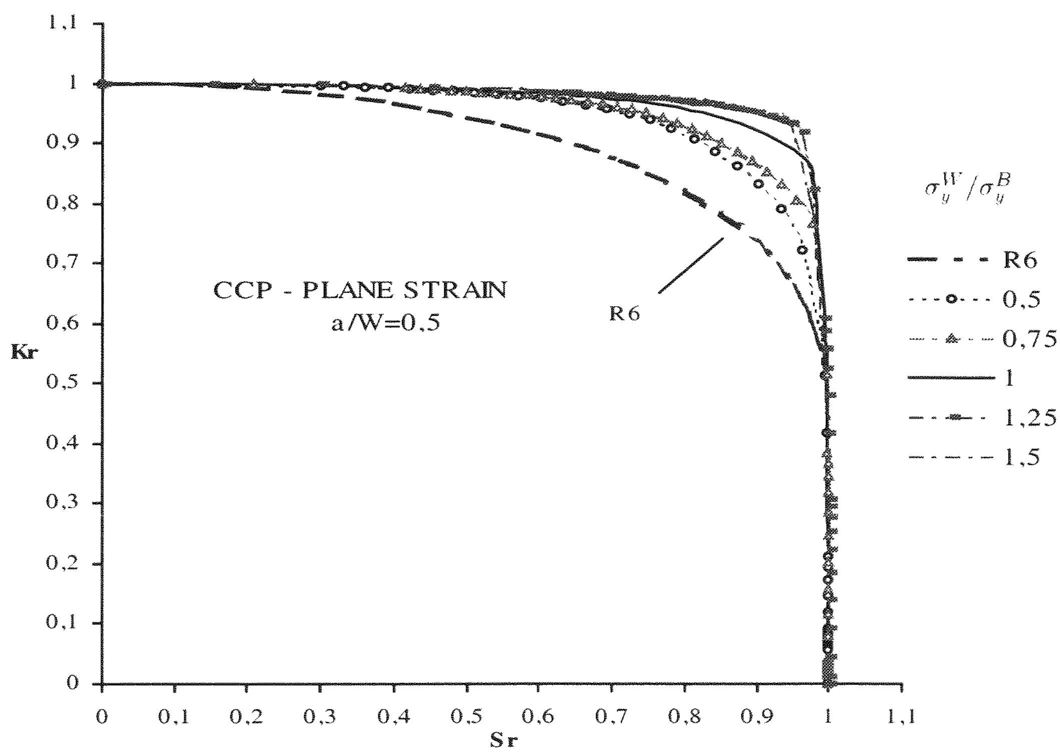

Figure 7.10: FAD of CCP weld plate (plane strain)- mismatched material model

we have $\eta_{pl} = 1$.

Now we examine this solution with finite element calculation. We express elastic plastic integral J in the following equation (see [35])

$$J = \eta_{el}\frac{U_{el}}{l} + \eta_{pl}\frac{U_{pl}}{l} \quad (7.4)$$

So it is easy to calculate η_{pl} at every load level by the following method:

$$\eta_{pl} = \frac{Jl}{U_{pl}} - \eta_{el}\frac{U_{el}}{U_{pl}} \quad (7.5)$$

where η_{el} is determined by an elastic calculation as below. It is independent of load level.

$$\eta_{el} = \frac{J_{el}l}{U_{el}} \quad (7.6)$$

Our finite element solutions are presented in Fig. 7.11 It is noticed that solution η_{pl} is in agreement with analytic one only at limit load level. In the case of homogeneous material we give the following approximate equation of η_{pl}

$$\eta_{pl} = 21.212x^5 - 47.019x^4 + 36.864x^3 - 10.654x^2 - 1.422x + 2.0178 \quad (7.7)$$

where $x = F/F_l$. We note that this approximate solution is useful because the fracture load is usually lower than the plastic limit load of the specimen.

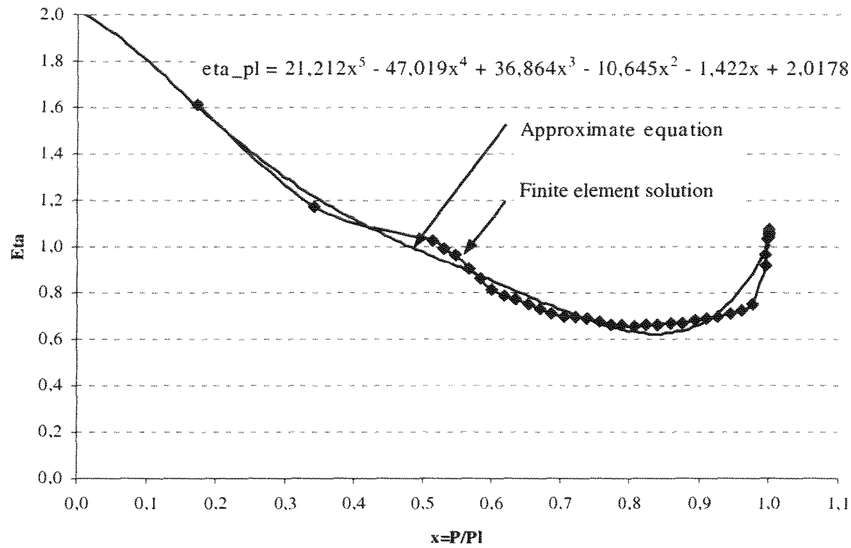

Figure 7.11: η_{pl} factor as function of loading level (homogeneous material $M = \sigma_y^W/\sigma_y^B = 1$)

Similarly, when we carry out experiments to assess the fracture toughness of mis-matched welded plates, we need to establish factor η_{pl} as function of the loading level. The FEM results are presented in Fig. 7.12 for undermatched model ($M = \sigma_y^W/\sigma_y^B = 0.5$) and in Fig. 7.13 for overmatched model ($M = \sigma_y^W/\sigma_y^B = 1.5$). The approximate fitting equations are also given in the figures. In comparison with the results of the homogeneous model, these curves have some similarities. The η_{pl} curve is like a dish bottom before arriving the final limit state. However, the load-dependence seems weaker for overmatched model. Anyway, the η_{pl} results of [35] given only at final limit state could not be used for practical experimental work. A complete work as above is necessary.

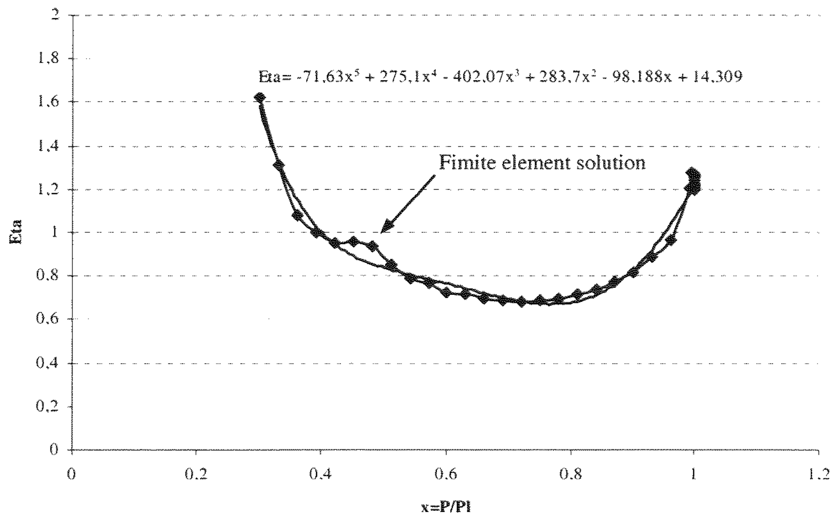

Figure 7.12: η_{pl} factor as function of loading level (undermatched model: $M = \sigma_y^W / \sigma_y^B = 0.5$)

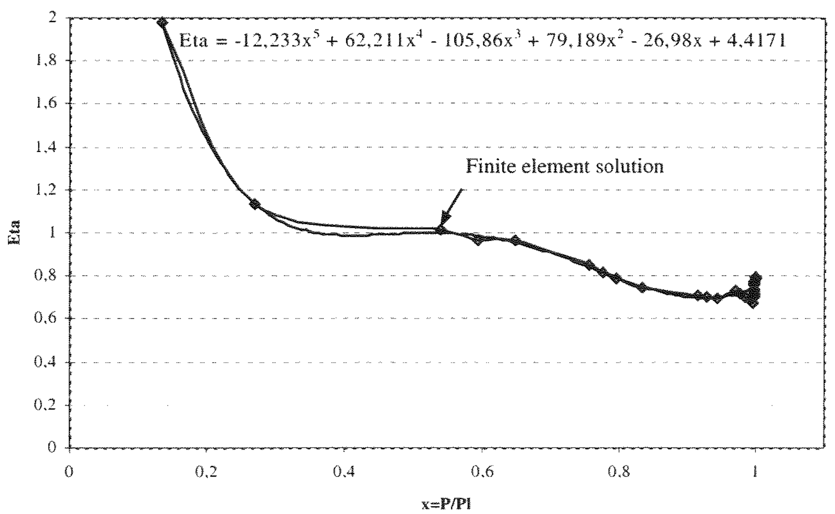

Figure 7.13: η_{pl} factor as function of loading level (overmatched model: $M = \sigma_y^W / \sigma_y^B = 1.5$)

8 Plastic limit and safety assessment of axially cracked cylinder

A long cylinder with extensive axial crack at internal wall is subjected to internal pressure. Plane strain state is considered. In this section we will study the limit load solution and R6 method with or without thermal loading. No hardening is assumed so that $S_r = L_r$.

8.1 Limit pressure of axially cracked cylinder

Consider one half symmetric structure that consist of rigid plastic material and is subjected on internal pressure on internal surface of cylinder. There exist not accurate analytic solution for this problem. However, we could obtain an approximate analytic solution by proposing an assumed mechanism as shown in Fig. 8.1

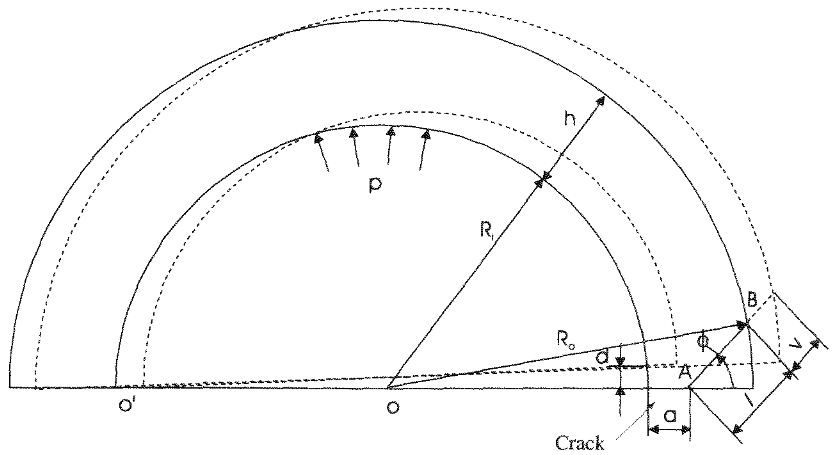

Figure 8.1: Assumed plastic slip mechanism of axially cracked cylinder under internal pressure

The assumed mechanism is to slip along line AB corresponding a rigid rotation around point O'. The length of assumed slip line l is determined from the geometric relation in ΔOAB.

$$R_0^2 = (R_i + a)^2 + l^2 - 2(R_i + a)l\cos(\pi - \phi) \tag{8.1}$$

Its solution is

$$l = -(R_i + a)\cos\phi + \sqrt{R_0^2 - (R_i + a)^2 \sin^2\phi} \tag{8.2}$$

The slipping velocity v as below

$$v = \frac{d}{\sin\phi} \tag{8.3}$$

According to this assumed mechanism, we find the external power of pressure:

$$\dot{W}_{ex} = \int_0^{\pi} \frac{1}{2} pR_i d \sin\theta(1 + \cos\theta)d\theta = pR_i d \tag{8.4}$$

Internally dissipated energy:

$$\dot{W}_{in} = k_v v l \tag{8.5}$$

So by upper bound theorem we have the following solution of limit pressure

$$p_l = \min_{\phi} p \tag{8.6a}$$

with

$$p = \frac{\sigma_y}{\sqrt{3} R_i R_0 \sin\phi}\left[\sqrt{R_0^2 - (R_i + a)^2 \sin^2\phi} - (R_i + a)\cos\phi\right] \tag{8.6b}$$

- The optimum solution is

$$p_l = \frac{\sigma_y}{\sqrt{3}} \frac{R_0^2 - (R_i + a)^2}{R_0 R_i} \tag{8.7}$$

corresponding to an optimized slip angle

$$\bar{\phi} = \arcsin\left(\frac{R_0}{\sqrt{R_0^2 + (R_i + a)^2}}\right) \tag{8.8}$$

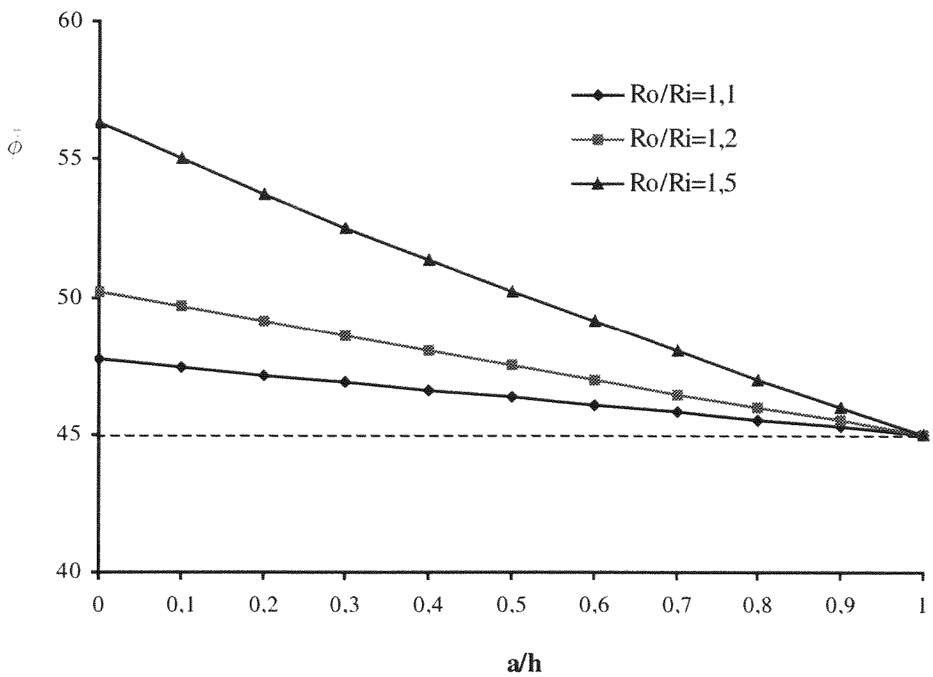

Figure 8.2: Slip angle of axially cracked cylinder under internal pressure

Now we consider a situation: the pressure is applied also on the crack surfaces. In this case the external pressure power:

$$\dot{W}_{ex} = p(R_i + a)d \tag{8.9}$$

By a similar procedure, we obtain an approximate analytic solution:

$$p_l = \frac{\sigma_y}{\sqrt{3}} \frac{R_0^2 - (R_i + a)^2}{R_0(R_i + a)} \tag{8.10}$$

This solution is a little lower than (8.7). The slip angle is the same as (8.8).

- It is easy to verify that a linear relation as below is between the above two solutions, respectively, without and with pressure on crack surfaces.

$$p_l = \left(1 - \frac{a}{h}\right) \frac{2\sigma_y}{\sqrt{3}} \ln \frac{R_0}{R_i} \tag{8.11}$$

  We note that this solution is only an approximate one and does not have strict upper bound property because the mechanism used is not completely compatible. Some other simple lower solutions were proposed as below

- Approximate bound of Chell [20]:

$$p_l = \frac{2\sigma_y}{\sqrt{3}} \frac{h - a}{R_i + a} \tag{8.12}$$

- Lower bound solution of Miller [37]

$$p_l = \frac{2\sigma_y}{\sqrt{3}} \ln \frac{R_0}{R_i + a} \tag{8.13}$$

  This solution is found to be very close to the above analytic solution (with pressure applied also on the crack surfaces).

In the following comparison, we consider that the crack surface free of pressure. We define a limit pressure factor as below

$$\alpha = \frac{p_l}{p_0} \tag{8.14}$$

with the thick tube solution in the absence of cracks [62]

$$p_0 = \frac{2}{\sqrt{3}} \sigma_y \ln \frac{R_0}{R_i}. \tag{8.15}$$

Fig. 8.3 shows the coarse finite element mesh (120 elements) for the present direct calculation. In fact, one notices in Fig. 8.3 that in limit state, the plastic deformation is concentrated around crack-tip region (net section region). Therefore, locally refined meshes and smooth transformation from the plastified region to the non-plastified region are important for the present method. We examine also these results with incremental elastic plastic calculation with a very refined mesh (2200 elements) as shown in Fig. 8.4. The predicted slip line verifies the assumed model. Numerical comparison is given in Table 8.1 for a special geometry. The analytic solution would be a lower bound due to the approximation of the proposed model. However, it approaches the accurate solution for a thin walled structure ($R_o/R_i \to 1$). A complete comparison is presented in Fig. 8.5 which shows good agreement.

Method	Approximate analyt. (8.7, 8.8)	Linear approx. (8.11)	Incremental (2200 ele.)	Upper bound (120 ele.)
Limit factor α_l	0.625	0.6	0.65	0.66
Slip angle $\phi(°)$	48	-	~ 48.2	~ 49

Table 8.1: Comparison of limit pressure and slip angle, $a/h = 0.4$

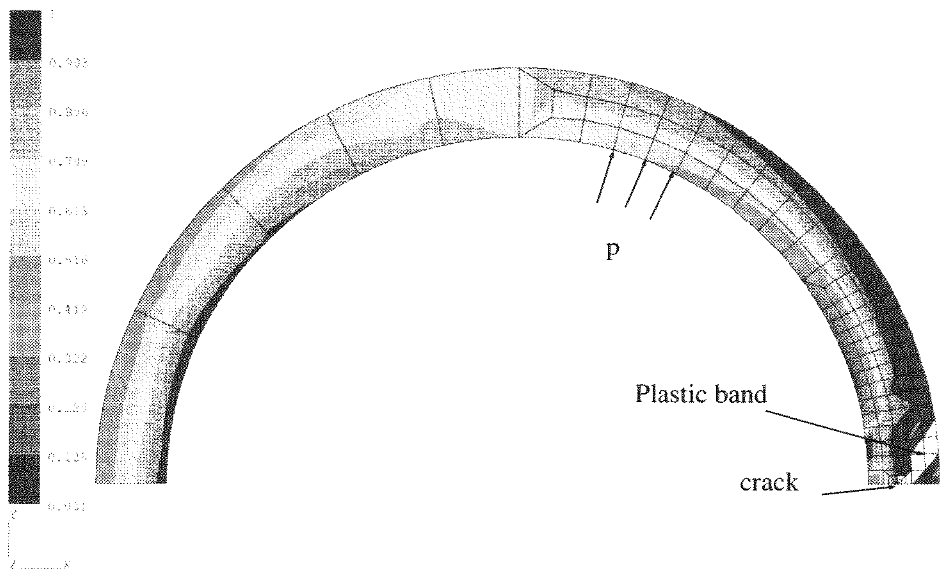

Figure 8.3: Finite element meshing and fictitious von Mises stress field in limit state (σ_{eq}/σ_y) (direct upper bound analysis)

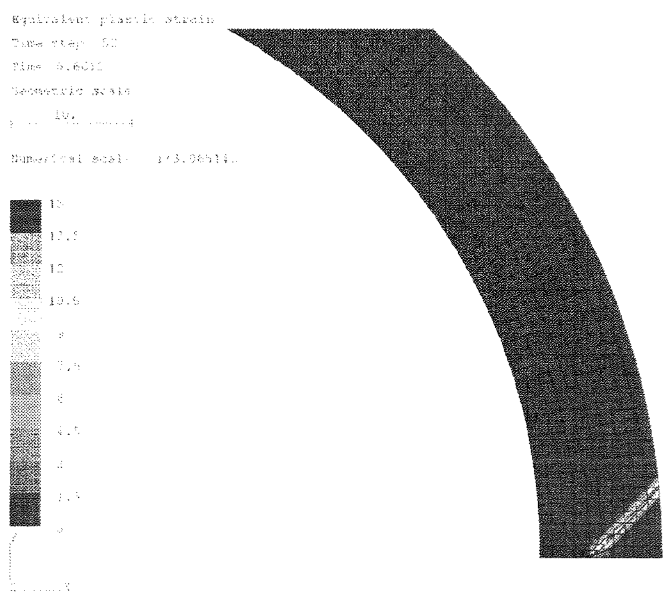

Figure 8.4: Finite element meshing and fictitious von Mises strain field in limit state $(\varepsilon_{eq}/\varepsilon_y)$ (incremental elastic-perfectly plastic analysis)

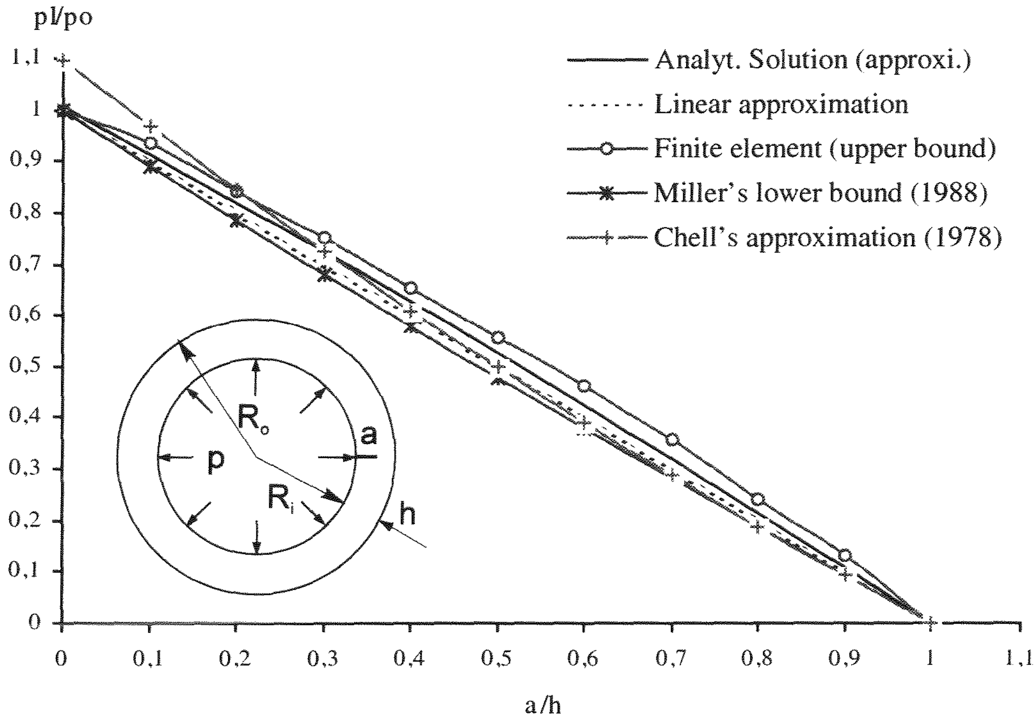

Figure 8.5: Limit pressure of axially-cracked cylinder ($R_0/R_i = 1.2$)

8.2 R6 curve of axially cracked cylinder under pressure

Elastic perfectly plastic finite element calculations are carried out as for the CCP specimens above. Three geometries and two types of material are chosen to take a comparison. In the calculation of elastic stress intensity factor, the finite element solution is compared with previous results, see [66], to obtain good agreement of 1%. Note that the solution of Yan & Nguyen Dang [66] corrected the errors in stress intensity factor handbook ([40]), for axially cracked cylinder under internal pressure.

The contour-independence of J integral is studied as in 7.1 for the weld centre cracked plate problem. Although similar results are obtained, it seems necessary to use a smaller crack tip elements to obtain stable results. In this case, the third layers of crack tip element are used to calculate the J integral. The contour-independence of integral J is shown in Fig. 8.6 and the maximum error of different contours at every loading step is shown in Fig. 8.7. This error of J is generally less than 10%. However, the maximum dependence happens at plastic limit state, which is a little different from CCP specimen.

Using the solution of integral J obtained by finite element calculation, FAD curves are constructed for several geometry with two groups of material data

- Material 1: $\sigma_y = 200$ Mpa, $E = 2.1 \times 10^5$ Mpa, $\nu = 0.3$, $\alpha_t = 1.2 \times 10^{-5}/K$
- Material 2: $\sigma_y = 100$ Mpa, $E = 2.1 \times 10^5$ Mpa, $\nu = 0.3$, $\alpha_t = 1.2 \times 10^{-5}/K$

The comparison between two type material data shows a good agreement. In Fig. 8.8 only the results for material 1 are presented. So we have verified that the obtained R6 curves are independent of material when one uses elastic perfectly plastic model.

It is seen in Fig. 8.8 that finite element results of FAD change with different geometry. Some of R6 curves (with small ratio of external and internal radius) are lower than theoretic curve of Eq. (2.13). The reason is still during investigation. Similar results were obtained by Kumar et al. [36] who showed that for both axially and circumferentially cracked cylinders of 304 stainless steel the finite element results are lower than theoretic R6 curve of Eq. (2.13). On the other hand, Kumar's results with A533B Cl.1 steel approach to theoretical R6 curve.

In comparison with the results of CCP in section 7, we have enough reason to point out that a more conservative FAD curve is necessary to be used for axially cracked cylinders under internal pressure.

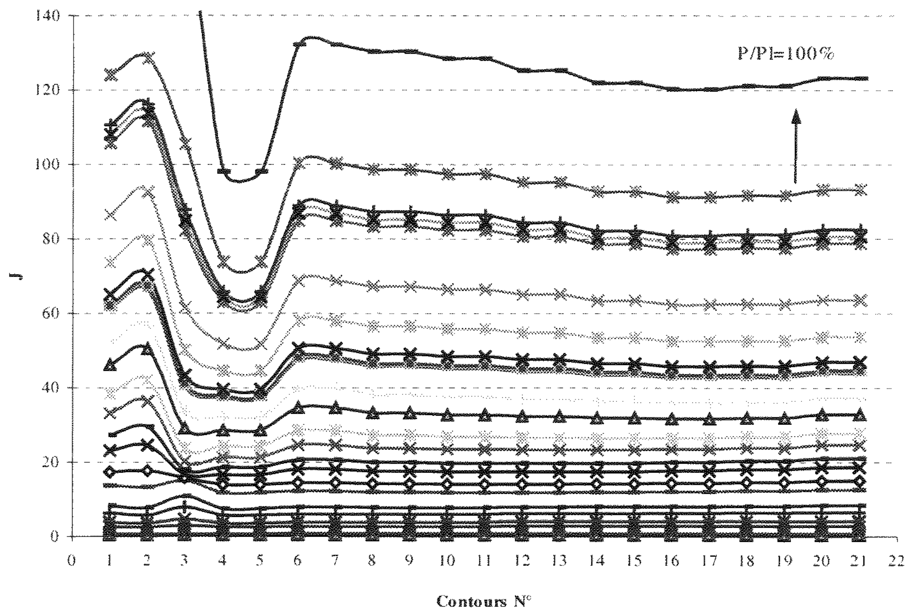

Figure 8.6: Independence of contour of J (axially cracked cylinder under pressure)

8.3 R6 curve of axially cracked cylinder under pressure and radial temperature gradient

The effect of thermal stress has been extensively discussed in R6 rule. If the stresses arising from thermal loads do not contribute to plastic collapse, they are categorized as secondary stress. It is this situation that will been studied in this section.

In integrity analysis with R6 method, the secondary stresses contribute only to the calculation of elastic stress intensity. Generally we have

$$K_r = K_r^p + K_r^s \tag{8.16}$$

The superscript p and s represent, primary and secondary stress, respectively. However, we will show as below the original R6 curve (without the effect of secondary stress) will be modified by the presence of secondary stress. This effect is recognized by a parameter ρ which takes account of plasticity correction required to cover interaction between σ^p and σ^s stresses, see R6 rule and [7]. In this section we investigate this problem by elastic perfectly plastic finite element calculation.

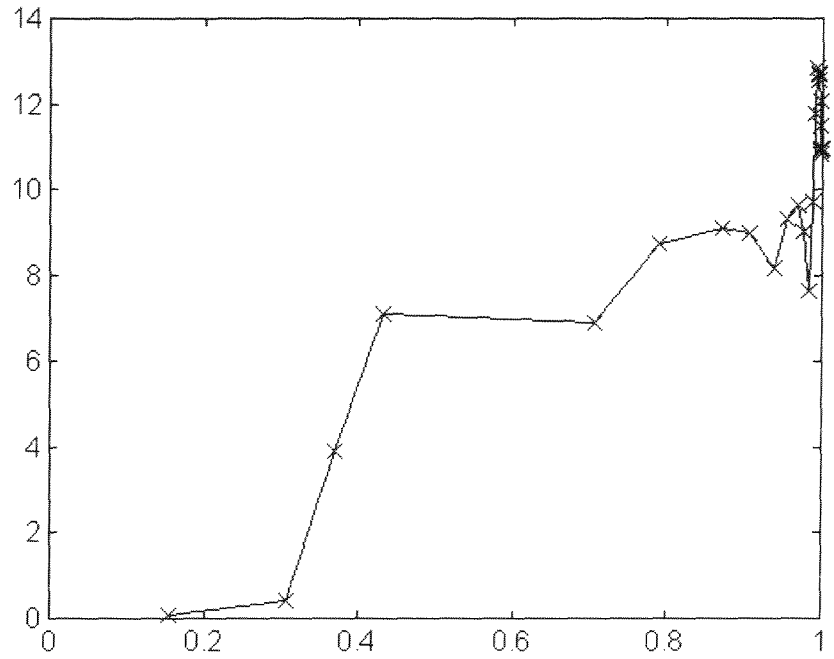

Figure 8.7: Maximum relative difference Δ of J integral on contours (axially cracked cylinder)

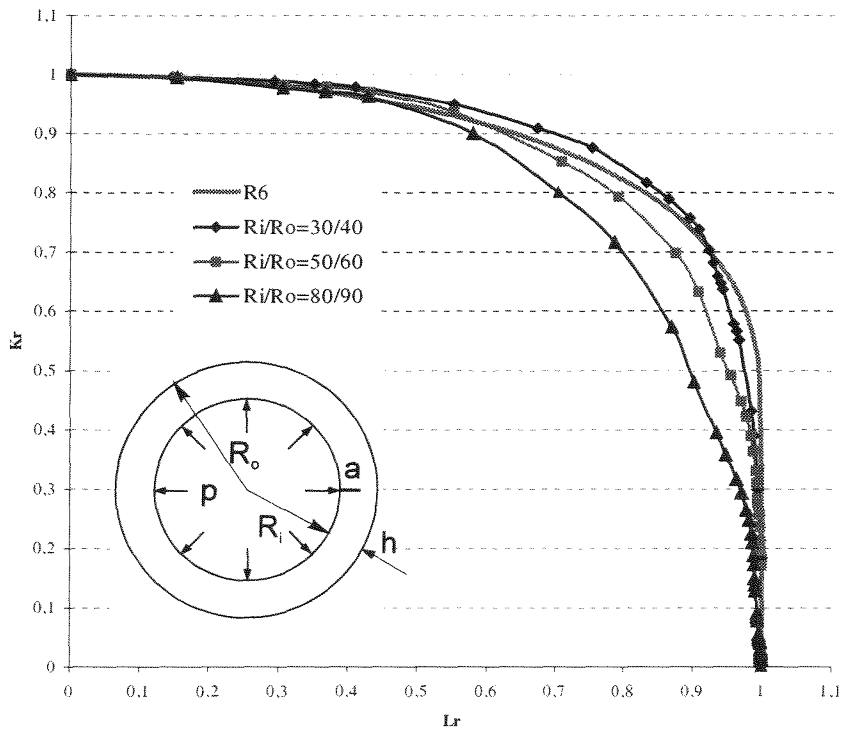

Figure 8.8: R6 curve of axially cracked cylinder under internal pressure (similar results are obtained for two material)

stress for large thermal stresses and the effect of stress redistribution seems great. In this case, the maximum reduction of R6 increases little. However, this reduction appears from very small to large mechanical loads.

Now we examine the effect of thermal loads in the cases of $dT \leq 200K$. The difference of R6 curves between the cases of $dT = 0K$ (without thermal loading) and $dT \neq 0K$ (with thermal loading) was explained as the plastic interaction between mechanical stresses and thermal (secondary) stresses in R6 rule, where this effect, identified as parameter ρ, is considered only when one uses R6 curve (without the effect of secondary stresses) for safety assessment. That means, one uses the following formula (8.17) instead of (8.16) to carry out safety assessments:

$$K_r = K_r^p + K_r^s + \rho \tag{8.17}$$

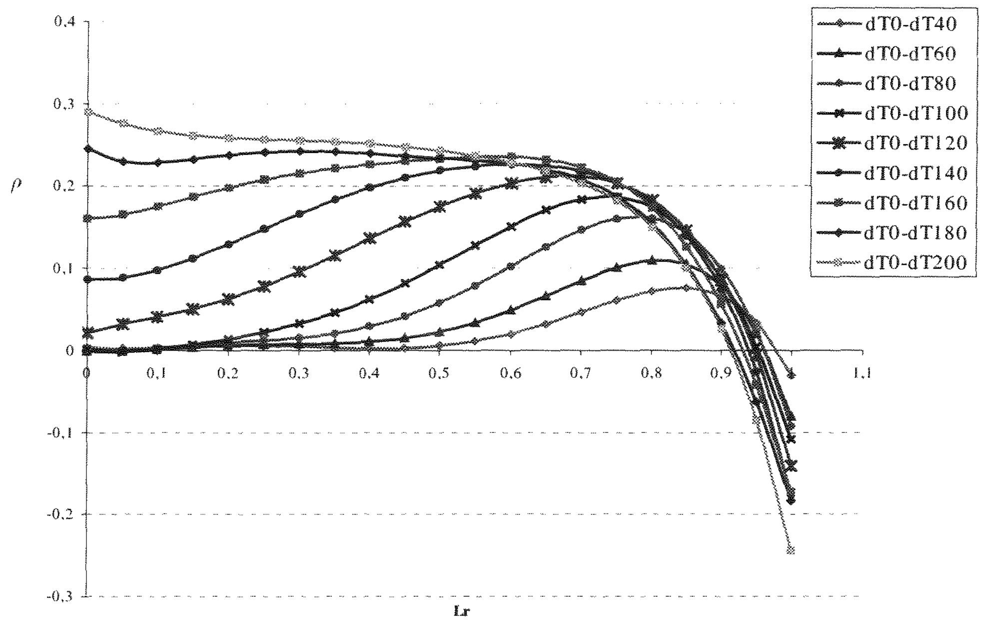

Figure 8.10: Plastic interaction parameter of axially cracked cylinder under internal pressure and thermal loading (temperature difference along thickness)

R6 rule recommends a series of procedures to estimate the parameter ρ based on the paper of Ainsworth [7]. In the following Fig. 8.10, we give the calculated ρ curves by present finite element results.

These ρ curves are similar in form to the results in [7], Fig. 4. The difference between the present results and in [7] may result from different geometry and material models. As it could be predicted, when temperature difference $dT \geq 120K$ the ρ curves is not zero when the mechanical load is absent. However, with a larger thermal loading, the maximum ρ increase little and the effect of stress redistribution becomes obvious. Originally ρ was restricted to non-negative values, but the possibility of negative values is seen in [11]. In order to take a comparison in quantity, we carry out a transformation by using a method similar to the one in [7]. The temperature difference is represented in corresponding elastic stress intensity factors. The maximum value of ρ in Fig. 8.10 is taken for every thermal loading (temperature difference) and then plotted in Fig. 8.11. In this comparison, two methods are used in estimation of abscissa of Fig. 8.11

1. The mean hoop stress in the position of crack of a non-cracked structure is used in calculation of K_I^s by $K_I^s = \sigma_\theta \sqrt{\pi a}$. The elastic SIF K_I^{pl} at plastic limit pressure is taken from [66].

2. The FEM is used in calculation of K_I^s. K_I^{pl} is as above.

The comparison in Fig. 8.11 shows that the present results are much higher than the results in [7]. The cause of difference is still being investigated. It seems to us that the different geometry and, particularly, the different material models lead to the different results. It is necessary to do more studies for this problem. According to the present results, we should be very prudent when we carry out a safety analysis using R6 rule for a cracked cylinder consist of a lower hardening material.

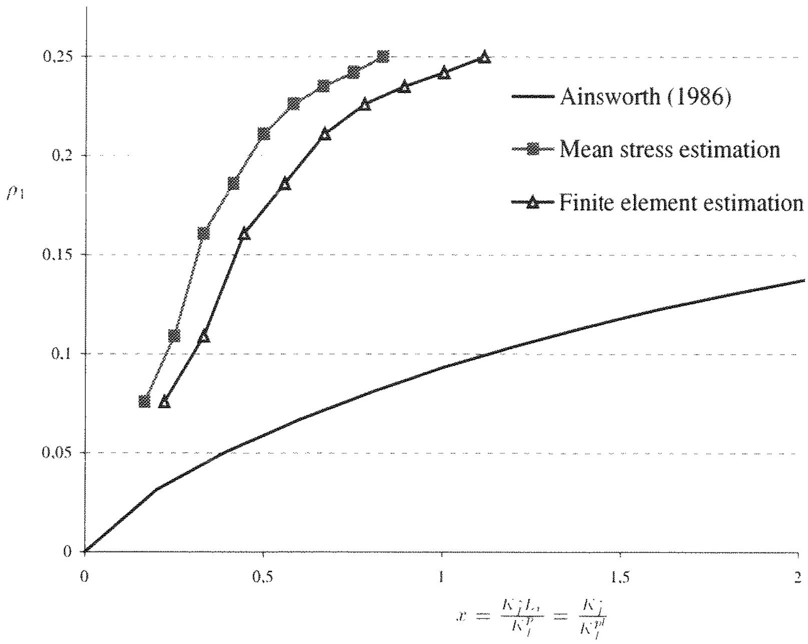

Figure 8.11: The values of ρ_1 for the defining K_r^s

9 Conclusions

This report presents various applications of limit analysis in ductile fracture mechanics. Examples are given for testing materials and for the assessment of structures including the strength mis-match of welds. The reported research is based on recent developments in upper and lower bound FEM-based limit analysis. It was intended to generate material to improve numerical methods and to demonstrate possible improvements of over-conservative limit load solutions.

Generally, numerical methods of direct limit analysis were shown to be reliable and numerically quite effective. However, from tests against known close bounds of limit loads some advise for higher accuracy could be given:

- Prefer underintegrated to fully integrated finite elements in plane strain analyses.
- Accuracy of upper bound can be improved in fracture mechanics by use of plastic strain singular crack-tip elements.

It remains to investigate, if all observed numerical errors can be addressed to the too stiff behaviour of fully integrated finite elements in the fully plastic deformation range.

The FEM-based limit analyses of CRB specimens showed that currently used limit load formulae could be improved to obtain safe but less conservative estimations. Some formulae for CT specimens are reliable but different to the FEM analyses. The formulae do not represent details like the side grooves. The use of ultimate stress gave closer best estimates of rupture loads of CRB and CT specimens for sufficiently ductile materials. But the mean value of yield and ultimate stress may be a more appropriate failure stress for assessment purpose. However, current practice is not without traps. Some limit loads have been adjusted to experiments. Then there may be no freedom to choose a different failure stress. In few cases handbooks give only the constraint solution which is unsafe for shallow cracks.

Generally the decision on the constraint is left to the engineer. For safe procedures the editors of handbooks could be advised:

- To classify the kind of limit loads into experimentally adjusted, exact, upper or lower bound.
- To indicate if another failure stress may be used.
- To give guidance on when to choose plane stress or plane strain (constraint).
- To give the application bounds if available.

A new limit load formula has been proposed and tested in a benchmark for an axisymmetrical tube with a circumferential crack under pressure and tension. Other formulae have been tested or modified.

The failure assessment diagram (FAD, R6 method) is applied to the non-standard problems of weld mis-match and thermal stress. It is shown that use of FAD for the latter still needs further research. Detailed FEM analyses for the mis-match problem showed that J-integral is path independent. The η–factor cannot be practically used for testing of such welds, because it is load dependent. The mis-match effect on the R6 curve is obvious in plane strain but not in plane stress state.

It may be concluded that FEM-based limit analysis is a valuable engineering method of ductile fracture mechanics. This would be more so if research could reduce the numerical error. The development of reliable limit load formulae for defect ductile piping and for other important crack-containing components is pending. Such formulae could be obtained from fits to numerical experiments on many cracked engineering structures. Further, FEM-based limit analysis may help improve handbooks in the required way. This will make current assessment practice more simple and less conservative with clear economic benefits. It is therefore recommended to initiate research extending the work in this report towards global validation, the development of new limit load solutions for further defect components and data for the indicated necessary handbook improvement.

References

[1] *Guidance on Methods for Assessing the Acceptability of Flaws in Fusion Welded Structures.* 1991. BSI Published Document PD6493:1991 British Standards Institution, London.

[2] *DINV ENV 1993-1-1: Eurocode 3, Teil1-1, Bemessung und Konstruktion von Stahlbauten, Allgemeine Bemessungsregeln, Bemessungsregeln für den Hochbau, Anhang C: Design against brittle fracture* 1993.

[3] *User Guide of R6-Code. Software for Assessing the Integrity of Structures Containing Defects* 1996. Version 1.4x, Nuclear Electric Ltd.

[4] *Assessment of the Integrity of Structures Containing Defects.* 1997. Nuclear Electric Procedure R/H/R6 - Revision 3.

[5] *Guide on Methods for Assessing the Acceptability of Flaws in Metallic Structures.* 2000. BSI Document BS7910:2000 British Standards Institution, London.

[6] R. A. AINSWORTH: The assessment of defects in structures of strain hardening material. *International Journal of Fracture* **6** (1984) R73–R77.

[7] R. A. AINSWORTH: The treatment of thermal and residual stresses in fracture assessments. *Engineering Fracture Mechanics* **24** (1986) 65–76.

[8] R. A. AINSWORTH:. *Private communication with R. Ainsworth, Nuclear Electric, UK, letter to M. Staat from 17th April* 1997.

[9] A. AL-LAHAM: *Stress Intensity Factor and Limit Load Handbook.* British Energy Report EPD/GEN/REP/0316/98, Issue 2 (1999).

[10] T. ANDERSON: *Fracture Mechanics. Fundamentals and Application.* CRC Boca Raton (1995).

[11] P. ANDERSSON, M. BERGMAN, B. BRICKSTAD, L. DAHLBERG, I. NILSSON, F. SATTARI-FAR: A Procedure for Safety Assessment of Components with Cracks – Handbook. SAQ/FoU-Report 96/08, The Swedish Plant Inspectorate, Stockholm 1996.

[12] BARSOUM: Triangular quarter-point elements as elastic and perfectly-plastic crack tip elements. *International Journal for Numerical Methods in Engineering* **11** (1977) 85–98.

[13] M. BELOUCHRANI, D. WEICHERT: An extension of the static shakedown theorem to inelastic cracked structures. *International Journal of Mechanical Science* **41** (1999) 163–177.

[14] J. P. BENTHEM, W. T. KOITER: Asymptotic approximations to crack problems in G. C. SHI (ed.):*Methods of analysis and solutions of crack problems.* Noordhoft International Publishing Groningen (1973) 131–178.

[15] M. BERGMAN: *User's manual SACC Version 4.0.* SAQ/FoU-Report 96/09, The Swedish Plant Inspectorate Stockholm (1996).

[16] J. BISHOP: On the complete solution to problems of deformation of a plastic-rigid material. *International Journal of Mechanical Science* **2** (1953) 43–53.

[17] A. BRÜCKNER-FOIT: Probabilistic Analysis of Crack Containing Structures with the PARIS Code. Technical Report, Kernforschungszentrum Karlsruhe KfK 4286 (1987).

[18] E. CAPURRO, F. ALICINO, A. CORVI, S. REALE: *Flaw acceptance criteria taking into consideration the NDT: radiographic and ultrasonic testing – Analysis through the fracture mechanics methods.* Report EUR 14698 EN, Commission of the European Communities Brussels (1993).

[19] A. J. CARTER: A library of limit loads of structures containing defects. CEGB Report TD/SID/REP/0032 1991.

[20] G. CHELL: A J estimation procedure for combined mechanical, thermal and residual stresses. *International Journal of Pressure Vessel & Piping* **23** (1986) 187–213.

[21] L. CIZELJ, H. RIESCH-OPPERMANN: ZERBERUS – the Code for Reliability Analysis of Crack Containing Structures. Technical Report, Kernforschungszentrum Karlsruhe KfK 5019 (1992).

[22] D. EWING, R. HILL: The plastic constraint of V–notched tension bars. *Journal of the Mechanics and Physics of Solids* **15** (1967) 112–124.

[23] D. EWING, C. RICHARDS: The yield–point loads of singly–notched pin–loaded tensile strips. *Journal of the Mechanics and Physics of Solids* **22** (1974) 22–36.

[24] D. GROSS: *Bruchmechanik.* Springer Berlin (1996).

[25] D. HARRIS, D. DEDHIA, S. LU: Theoretical and User's Manual for PC-PRAISE. A probabilistic Fracture Mechanics Computer Code for Piping Reliability Analysis. Technical Report, Report NUREG/CR-5864 (1992).

[26] M. HEITZER: Traglast– und Einspielanalyse zur Bewertung der Sicherheit passiver Komponenten. *Berichte des Forschungszentrums Jülich* **3704** (1999).

[27] M. HEITZER, M. STAAT: FEM–computation of load carrying capacity of highly loaded passive components by direct methods. *Nuclear Engineering and Design* **193** (1999) 349–358.

[28] M. HEITZER, M. STAAT: Traglastanalyse – ein strukturmechanisches Verfahren zur Beurteilung von gerissenen Bauteilen und Verbindungen. *DVM-Bericht 232: Festigkeits- und Bruchverhalten von F"ugeverbindungen* (2000) 183–192.

[29] R. HILL: On discontinuous plastic states, with special reference to localised necking in thin sheets. *Journal of the Mechanics and Physics of Solids* **1** (1952) 19–30.

[30] T. HOLLSTEIN, W. SCHMITT: An estimation procedure for the J-integral in the fully plastic range – experimental and analytical verifications. *International Journal of Fracture* **16** (1980) R195–R198, R255.

[31] Y. J. HUANG, E. STEIN: Shakedown of a CT specimen with St52 steel–experimental, analytical and numerical investigations. *Journal of Strain Analysis* **30** (1995) 283–289.

[32] N. D. HUNG, B. C. THANH, A.-M. YAN: Comparsion and numerical testing of limit analysis and shakedown computation of nuclear plant components. *Internal Report Nr. R96–21, LTAS, Université de Liège* (1993).

[33] J. HUTCHINSON: Plastic stress and strain field at a crack tip. *Journal of the Mechanics and Physics of Solids* **16** (1968) 13–31.

[34] L. ISSLER, H. RUOSS, P. HÄFELE: *Festigkeitslehre – Grundlagen*. Springer Berlin, Heidelberg (1995).

[35] J. JOCH, R. A. AINSWORTH, T. H. HYDE: Limit load and J–estimates for idealised problems of deeply cracked welded joints in plane–strain bending and tension. *Fatigue and Fracture of Engineering Materials and Structures* **16** (1993) 1061–1079.

[36] V. KUMAR, M. D. GERMAN, C. F. SHIH: *An engineering approach for elastic–plastic fracture analysis*. EPRI NP-1931, Project 1237-1 Topical Report New York (1981).

[37] A. G. MILLER: Review of limit loads of structures containing defects. *International Journal of Pressure Vessel & Piping* **32** (1988) 197–327.

[38] B. MORAN, S. SHIH: Crack tip and associated domain integrals from momentum and energy balance. *Engineering Fracture Mechanics* **27** (1987) 615–642.

[39] D. MUNZ: *Leck-vor-Bruch-Verhalten druckbeaufschlagter Komponenten*. VDI-Verlag Düsseldorf (1984).

[40] Y. MURAKAMI: Stress Intensity Factors Handbook. Technical Report, Pergamon Press Oxford (1987).

[41] B. A. MURTAGH, M. A. SAUNDERS:. *MINOS 5.1 - User's Guide*. Stanford University 1987. Technical Report SOL 83-20R.

[42] J. NAGTEGAAL, D. PARKS, J. RICE: On numerically accurate finite element solutions in the fully plastic range. *Computer Methods in Applied Mechanics and Engineering* **4** (1977) 153–177.

[43] B. NEALE: The fracture behaviour of a circumferentially cracked bar in tension. Technical Report, T.A.G.S.I Symposium: Advance in fracture mechanics, AEA Technology, Abington, Cambridge, UK, 9-10 January (1996).

[44] J. R. RICE, G. F. ROSENGREN: Plane strain deformation near a crack tip in a power law hardening material. *Journal of the Mechanics and Physics of Solids* **16** (1968) 1–12.

[45] J. ROYER, J. M. TISSOT, A. PELISSIER-TANON, P. LE POAC, D. MIANNAY: J–integral determinations and anlyses for small test specimens and their usefulness for estimating fracture toughness in *Elastic–Plastic Fracture*. ASTM STP 668 Philadelphia (1977) 522–533.

[46] K.-H. SCHWALBE, Y.-J. KIM, S. HAO, A. CORNEC, M. KOÇAK: EFAM ETM-MM 96 – the ETM Method for assessing the significance of crack-like defects in joints with mechanical heterogeniety (strength mismatch). Report GKSS 97/E/9, GKSS-Forschungszentrum Geesthacht 1997.

[47] K.-H. SCHWALBE, U. ZERBST, Y.-J. KIM, W. BROCKS, A. CORNEC, J. HEERENS, H. AMSTUTZ: EFAM ETM97 – the ETM method for assessing the significance of crack-like defects in engineering structures, comprising the versions ETM97/1 and ETM97/2. Report GKSS 98/E/6, GKSS-Forschungszentrum Geesthacht 1998.

[48] M. SCIBETTA: Fracture toughness evaluation of circumferentially-cracked round bars. Technical Report, Report of SCK.CEN, BLG-716, Mol, Belgium (1996).

[49] M. SCIBETTA: *Contribution to the evaluation of the circumferentially-cracked round bar for fracture toughness determination of reactor pressure vessel steels.* Thesis Université de Liège, Faculté des Sciences Appliquées (1999).

[50] M. SCIBETTA:. *Private communication with M. Scibetta, Studiecentrum voor kernenergie - Centre d'étude de l'énergie nucléaire (SCK-CEN), e-mail to M. Staat from 15th February* 2000.

[51] M. SCIBETTA, R. CHAOUADI: Fracture toughness derived from small circumferentially cracked bar in W. CORWIN, E. ROSINSKI, V. WALLE (eds.):*Small specimen test techniques.* ASTM STP 1329 (1997).

[52] M. SEIDENFUSS: *Untersuchungen zur Beschreibung des Versagensverhaltens mit Hilfe von Schädigungsmodellen am Beispiel des Werkstoffes 20 MnMoNi 55.* Thesis Techn.-wiss. Ber. MPA Heft 92-05, Universität Stuttgart (1992).

[53] M. SEIDENFUSS:. *Private communication with M. Seidenfuß, Staatliche Materialprüfungsanstalt, Stuttgart, e-mail to M. Staat from 22nd January* 1999.

[54] W. SHEN: *Traglast– und Anpassungsanalyse von Konstruktionen aus elastisch, ideal plastischem Material.* Thesis Universität Stuttgart (1986).

[55] A. SHERRY, B. NEALE, G. GAGE, D. SANDERSON: The use of circumferentially-cracked bars for the measurement of fracture toughness. Technical Report, FCF 11 -Mechanisms and Mechanics of damage and failure, Poitiers Sept. 96 (1996).

[56] J. E. SRAWLEY: Wide range stress intensity factor expressions for ASTM E 399 standard fracture toughness specimens. *International Journal of Fracture* **12** (1976) 475–476.

[57] M. STAAT: Problems and Chances for Probabilistic Fracture Mechanics in the Analysis of Steel Pressure Boundary Reliability. in *Technical feasibility and reliability of passive safety systems for nuclear power plants. Proceedings of an Advisory Group Meeting,IAEA-TECDOC-920* Jülich (1994) 43–55.

[58] M. STAAT, M. HEITZER: Limit and shakedown analysis for design. *Proceedings of* 7^{th} *German–Japanese Joint Seminar on Research in Structural Strength and NDE-Problems in Nuclear Engineering, Stuttgart* (1997) 4.3.1–4.3.19.

[59] M. STAAT, M. HEITZER: Limit and shakedown analysis for plastic safety of complex structures. *Transactions of SMiRT* **14** (1997) B02/2.

[60] M. STAAT, M. HEITZER: LISA, ein europäisches Projekt zur FEM– basierten Traglast– und Einspielanalyse. *25. MPA-Seminar, Stuttgart* (1999) 10.1–10.20.

[61] W. STOPPLER, D. STURM, P. SCOTT, G. WILKOWSKI: Analysis of the failure behaviour of longitudinally flawed pipes and vessels. *Nuclear Engineering and Design* **151** (1994) 425–448.

[62] I. SZABO: *Höhere Technische Mechanik.* Springer–Verlag, Berlin (1972).

[63] F. VOLDOIRE: Limit analysis by the Norton–Hoff–Friaâ regularising method. Internal Report, EDF 1998.

[64] F. VOLDOIRE: LISA Minutes of the Brite-EuRam Meeting (3.04.98): Validation and industrial applications (task 5.2). CR EDF/MMN 98-083 1998.

[65] A.-M. YAN: *Contribution to the direct limit state aalysis of plastified and cracked structures*. Thesis Université de Liège, Faculté des Sciences Appliquées (1999).

[66] A.-M. YAN, N. D. HUNG: Stress intensity factors and crack extension in a cracked pressurised cylinder. *Engineering Failure Analysis* **1** (1994) 307–315.

[67] A.-M. YAN, N. D. HUNG: A non–linear programming upper bound study of shakedown limit to structure under variable thermal loading. *Internal Report N° R96–4–1, LTAS, Université de Liège* (1996).

[68] A.-M. YAN, N. D. HUNG: Shakedown of structures by improved Koiter's theorem. *Proceeding of National Congress on Theoretical & Applied Mechanics* (1997) 449–452.

[69] A.-M. YAN, N. D. HUNG: A modified Koiter's shakedown formulation. *EUROMECH 385, Inelastic Analysis of Structures under Variable Loads: Theory and Engineering Applications, Aachen* (1998) 83–85.

[70] A.-M. YAN, N. D. HUNG: Limit state of cracked structures by direct mathematical programming technique in R. E. A. VAN KEER (ed.):*ACOMEN'98 Advanced Computational Methods in Engineering*. Shaker Publishing B.V. (1998) 187–194.

[71] A.-M. YAN, N. D. HUNG: Shakedown of structures under thermal and mechanical loading. Proceedings of Plasticity '99, Cancun, Mexico, 5.–13.1.1999 1999.

[72] A. ZAHOOR:. *Ductile Fracture Handbook* 1991. Novotech. GP & EPRI, Res. Proj. 1757–69, Palo Alto.

[73] U. ZERBST, C. WIESNER, M. KOÇAK, L. HODULAK: SINTAP: Entwurf einer vereinheitlichten europäischen Fehlerbewertungsprozedur – eine Einführung. Report GKSS 99/E/65, GKSS-Forschungszentrum Geesthacht 1999.

[74] G. ZHANG: *Einspielen und dessen numerische Behandlung von Flächentragwerken aus ideal plastischem bzw. kinematisch verfestigendem Material*. Thesis Universität Hannover (1991).

A Appendix: The singularity of strain singular elements

Substituting (4.5) in (4.4) and collecting terms we have the following results:

$$x = \frac{h}{2}(1+\xi) \qquad\qquad y = \frac{l}{4}(1+\xi)(1+\eta) \tag{A1}$$

For any point P on the radial line R, the distance r from the crack tip is

$$r = \sqrt{x^2+y^2} = (1+\xi)\sqrt{\frac{h^2}{4}+\frac{l^2(1+\eta)^2}{16}} \tag{A2}$$

Inverting (A2) we obtain

$$(1+\xi) = \frac{r}{\sqrt{\frac{h^2}{4}+\frac{l^2(1+\eta)^2}{16}}} = \frac{r}{\bar{r}} \tag{A3}$$

$\bar{r}$ is a constant for any point on the line R (η is constant). Using (A1), the JACOBIAN matrix of transformation $\mathbf{J}$ is given by

$$\mathbf{J} = \begin{bmatrix} \frac{\partial x}{\partial \xi} & \frac{\partial y}{\partial \xi} \\ \frac{\partial x}{\partial \eta} & \frac{\partial y}{\partial \eta} \end{bmatrix} = \begin{bmatrix} \frac{h}{2} & \frac{l(1+\eta)}{4} \\ 0 & \frac{l(1+\xi)}{4} \end{bmatrix} \tag{A4}$$

and its determinant

$$\det|\mathbf{J}| = \frac{hl}{8}(1+\xi) \tag{A5}$$

Inverting,

$$\mathbf{J}^{-1} = \begin{bmatrix} I_{11} & I_{12} \\ I_{21} & I_{22} \end{bmatrix} = \begin{bmatrix} \frac{h}{2} & -\frac{2(1+\eta)}{h(1+\xi)} \\ 0 & \frac{4}{l(1+\xi)} \end{bmatrix} \tag{A6}$$

The displacements (u, v) within the element are interpolated by the same functions $N_i(\xi, \eta)$ of equation (5.1) from the nodal displacements u_i, v_i

$$u = \sum_{i=1}^{8} N_i(\xi,\eta)u_i, \qquad\qquad v = \sum_{i=1}^{8} N_i(\xi,\eta)v_i \tag{A7}$$

The derivatives of u, v with respect to ξ, η, are

$$\begin{aligned} \frac{\partial u}{\partial \xi} &= \sum_{i=1}^{8}\frac{\partial N_i}{\partial \xi}u_i \qquad & \frac{\partial u}{\partial \eta} &= \sum_{i=1}^{8}\frac{\partial N_i}{\partial \eta}u_i \\ \frac{\partial v}{\partial \xi} &= \sum_{i=1}^{8}\frac{\partial N_i}{\partial \xi}v_i \qquad & \frac{\partial v}{\partial \eta} &= \sum_{i=1}^{8}\frac{\partial N_i}{\partial \eta}v_i \end{aligned} \tag{A8}$$

Substituting (5.1) into (A8) and collecting terms, the derivatives can be written in the form:

$$\begin{aligned} \frac{\partial u}{\partial \xi} &= a_0 + a_1(1+\xi) \qquad & \frac{\partial u}{\partial \eta} &= b_0 + b_1(1+\xi) + b_2(1+\xi)^2 \\ \frac{\partial v}{\partial \xi} &= c_0 + c_1(1+\xi) \qquad & \frac{\partial v}{\partial \eta} &= d_0 + d_1(1+\xi) + d_2(1+\xi)^2 \end{aligned} \tag{A9}$$

where

$$a_0 = \frac{u_1}{4}(-2+3\eta-\eta^2) + \frac{u_2}{4}(-2+\eta+\eta^2) + \frac{u_3}{4}(-2-\eta+\eta^2)$$

$$
\begin{aligned}
& + \frac{u_4}{4}(-2-3\eta-\eta^2) + u_5(1-\eta) + \frac{u_6}{2}(1-\eta^2) + u_7(1+\eta) + \frac{u_8}{2}(-1+b^2) \\
a_1 &= \frac{1-\eta}{2}(u_1+u_2-2u_5) + \frac{1+\eta}{2}(u_3+u_4-2u_7) \qquad (*) \\
b_0 &= u_1(\eta-\frac{1}{2}) + u_4(\eta+\frac{1}{2}) - 2u_8\eta \\
b_1 &= u_1(\frac{3}{4}-\frac{1}{2}\eta) + u_4(\frac{1}{4}+\frac{\eta}{2}) - u_3(\frac{1}{4}-\frac{\eta}{2}) - u_4(\frac{3}{4}+\frac{\eta}{2}) - u_5 - u_6\eta + u_7 + u_8\eta \\
b_2 &= \frac{1}{4}(-u_1-u_2+u_3+u_4+2u_5-2u_7)
\end{aligned}
$$

The coefficients c_0, c_1, d_0, d_1, d_2 of derivatives $\partial v/\partial\xi, \partial v/\partial\eta$ are exactly the same to those a_0, a_1, b_0, b_1, d_2 of $\partial u/\partial\xi, \partial u/\partial\eta$ except for replacing every u_i by the corresponding v_i. They are all constant for any given set of nodal displacements, and along the line θ = constant (η =constant). Therefore, equation (A9) will depend only on ξ. The strains are given by

$$
\begin{Bmatrix} \epsilon_x \\ \epsilon_y \\ \epsilon_{xy} \end{Bmatrix} = \begin{Bmatrix} \frac{\partial u}{\partial x} \\ \frac{\partial v}{\partial y} \\ \frac{\partial u}{\partial y} + \frac{\partial v}{\partial x} \end{Bmatrix} \qquad \text{(A10)}
$$

The derivative of u and v with respect to x and y above are obtained by multiplying $\mathbf{J}^{-1}$ by their derivatives with respect to ξ and η.

$$
\frac{\partial u}{\partial x} = I_{11}\frac{\partial u}{\partial \xi} + I_{12}\frac{\partial u}{\partial \eta}, \qquad \frac{\partial u}{\partial y} = I_{21}\frac{\partial u}{\partial \xi} + I_{22}\frac{\partial u}{\partial \eta} \qquad \text{(A11)}
$$

The derivatives for v are completely similar, we get finally:

$$
\begin{aligned}
\frac{\partial u}{\partial x} &= A_0 + A_1 r + \frac{A_2}{r}, & \frac{\partial u}{\partial y} &= B_0 + B_1 r + \frac{B_2}{r}, \qquad \text{(A12)} \\
\frac{\partial v}{\partial x} &= C_0 + C_1 r + \frac{C_2}{r}, & \frac{\partial v}{\partial y} &= D_0 + D_1 r + \frac{D_2}{r}
\end{aligned}
$$

where

$$
\begin{aligned}
A_0 &= \frac{ha_0}{2} - \frac{2b_1(1+\eta)}{h}, \quad A_1 = \frac{ha_1}{2\bar{r}} + \frac{2b_2(1+\eta)}{h\bar{r}}, \quad A_2 = -\frac{2b_0\bar{r}(1+\eta)}{h} \qquad \text{(A13)} \\
B_0 &= \frac{4b_1}{l}, \quad B_1 = \frac{4b_2}{l\bar{r}}, \quad B_2 = \frac{4b_0\bar{r}}{l} \\
C_0 &= \frac{hc_0}{2} - \frac{2c_1(1+\eta)}{h}, \quad C_1 = \frac{hd_1}{2\bar{r}} + \frac{2d_2(1+\eta)}{h\bar{r}}, \quad C_2 = -\frac{2d_0\bar{r}(1+\eta)}{h} \\
D_0 &= \frac{4d_1}{l}, \quad D_1 = \frac{4d_2}{l\bar{r}}, \quad D_2 = \frac{4d_0\bar{r}}{l} \\
\bar{r} &= \sqrt{\frac{h^2}{4} + \frac{l^2(1+\eta)^2}{16}}
\end{aligned}
$$

A_i, B_i, C_i, D_i $(i = 0, \ldots, 2)$ are all constants independent of r. It is clear that as $r \to 0$, then all strain component express a singularity of $1/r$. This singularity just satisfies the requirement of perfectly plastic analysis.

B Appendix: Analytical lower bound for benchmark LA4

Benchmark LA4 is an axisymmetrical infinite tube with a circumferential edge crack (cf. Figure 6.6). This tube is loaded by tension F following the (Oz) axis, combined with an inner pressure P. The loading vector is defined by: $\alpha(\kappa F, (1-\kappa)P)$ where $\kappa \in [0,1]$. We are looking for the limit load factor for different values of κ to determine the admissible (F, P) domain. We build with the static approach a lower bound of the limit load factors. We take the following stress field, defined by strips (This field is a partial statically admissible solution, which can be completed by a special admissible one near the boundary condition, following Bishop [16]:

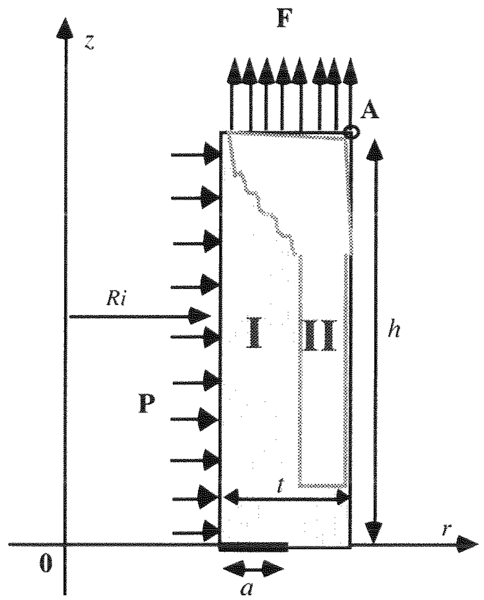

$$\text{Strip I :} \quad \sigma^I = \begin{pmatrix} \sigma_{rr}(r) & & \\ & \sigma_{\theta\theta}(r) & \\ & & 0 \end{pmatrix}$$

$$\text{Strip II :} \quad \sigma^{II} = \begin{pmatrix} \sigma_{rr}(r) & & \\ & \sigma_{\theta\theta}(r) & \\ & & \lambda\kappa F \end{pmatrix}$$

$$\lambda = \frac{\text{tube section area}}{\text{strip II section area}} = \frac{R_o^2 - R_i^2}{R_o^2 - (R_i + a)^2}$$

Figure B1: Statical approach for the LA4 test

We define an admissible radial stress field (linearly increasing from -P to 0 through the thickness):

$$\sigma_{rr}(r) = \frac{(1-\kappa)P}{R_o - R_i}(r - R_o) \tag{B1}$$

Using the equilibrium equations $r\sigma_{rr,r} - \sigma_{\theta\theta} + \sigma_r = 0$ we get the hoop stress :

$$\sigma_{\theta\theta}(r) = \frac{(1-\kappa)P}{R_o - R_i}(2r - R_o). \tag{B2}$$

<u>σ^I stress field:</u>

The strip I is only loaded by pressure. The von Mises yield criterion

$$\Phi(\boldsymbol{\sigma}) = \sqrt{\sigma_{rr}^2 + \sigma_{\theta\theta}^2 - \sigma_{rr}\sigma_{\theta\theta}} = \sigma_y \tag{B3}$$

applied to σ^I leads to the limit value for the strip I (the extremum is reached for $R_f = R_i + a$, the inner radius of the strip II) :

$$(1-\kappa)P_{\mathrm{I}}^{lim} = \frac{\sigma_y(R_o - R_i)}{\sqrt{3R_f^2 + R_o^2 - 3R_f R_o}}. \tag{B4}$$

σ^{II} stress field:

The strip II is loaded by both tension and pressure ($F = 1, P = 1$). The yield criterion (B3) applied to σ^{II} for the whole loading factor α leads to the limit value depending on the κ parameter. It is obtained as the minimum for $R_f \leq r \leq R_o$ of the equation:

$$\alpha_{\mathrm{II}}^{lim} = \min_r \left(\frac{\sigma_y(R_o - R_i)}{\sqrt{(1-\kappa)^2(3r^2 + R_o^2 - 3rR_o) + (\lambda\kappa(R_o - R_i))^2 - \lambda\kappa(1-\kappa)(R_o - R_i)(3r - 2R_o)}} \right) \tag{B5}$$

This minimum is reached either for R_f or for R_o depending on the parameter $\kappa \leq K$. The parameter K depends on the geometry data a, t, R_i. For the benchmark LA4 it holds $K = 0.88$ such that

If $\kappa \leq K$ then

$$\alpha_{\mathrm{II}}^{lim} = \frac{\sigma_y(R_o - R_i)}{\sqrt{(1-\kappa)^2 R_o^2 + (\lambda\kappa(R_o - R_i))^2 - \lambda\kappa(1-\kappa)(R_o - R_i)R_o}} \tag{B6}$$

If $\kappa \geq K$ then

$$\alpha_{\mathrm{II}}^{lim} = \frac{\sigma_y(R_o - R_i)}{\sqrt{(1-\kappa)^2(3R_f^2 + R_o^2 - 3R_fR_o) + (\lambda\kappa(R_o - R_i))^2 - \lambda\kappa(1-\kappa)(R_o - R_i)(3R_f - 2R_o)}} \tag{B7}$$

Then we get from $\alpha_{\mathrm{II}}^{lim}$ the values of P_{II}^{lim} and F_{II}^{lim}. The extremum is always reached within the strip II.

Remark: if $\kappa = 0$ (pure pressure), we get:

$$P^{lim} = \frac{2t\sigma_y}{2R_m + t} = \frac{t}{R_o}\sigma_y (= 9.0909 \text{ MPa here}), \tag{B8}$$

to compare with the exact usuall better lower bound:

$$P_*^{lim} = \sigma_y \ln\frac{2R_m + t}{2R_m - t} = \sigma_y \ln\frac{R_o}{R_i} (= 9.531 \text{ MPa here}). \tag{B9}$$

Remark: if $\kappa = 1$ (pure tension), we get:

$$F^{lim} = \frac{\sigma_y}{\lambda} (= 75.89 \text{ MPa here}), \tag{B10}$$

to compare with the lower bound [36], which includes plastic constraint of deep cracks:

$$F_*^{lim} = \frac{2}{\sqrt{3}}\frac{\sigma_y}{\lambda} (= 87.63 \text{ MPa here}). \tag{B11}$$

The numerical results for benchmark LA4 are shown in Tab. 6.2 and Fig. B2.

Remark: If we try the elastic Lamé solution for the stresses σ_{rr} and $\sigma_{\theta\theta}$ in the strips I and II, we get a lower bound of the limit load factor.

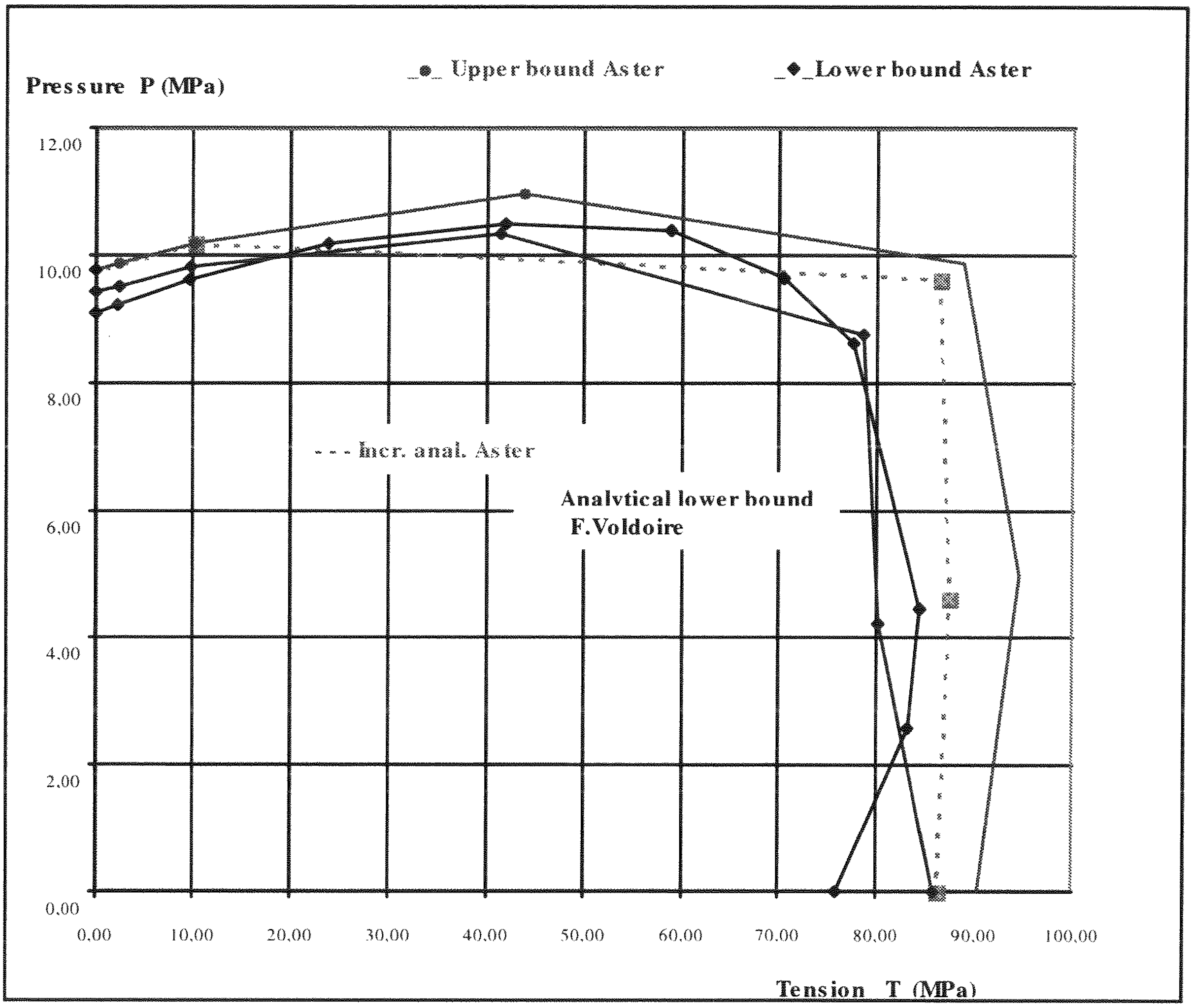

Figure B2: Comparison of (F, P) curves for the LA4 test, analytical solution by F.Voldoire.

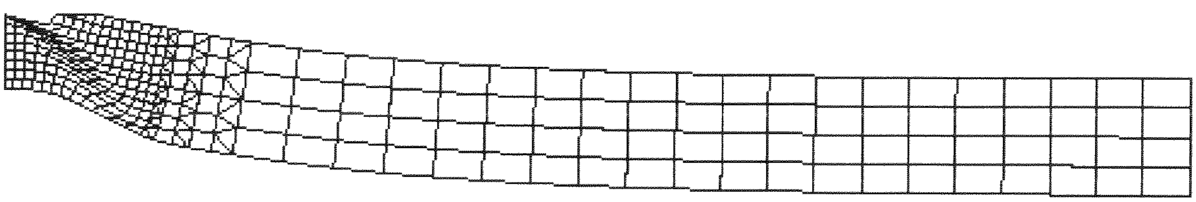

Figure B3: Collapse mode for the La4 test in pure tension (limit analysis computation with Code_Aster®).

Forschungszentrum Jülich

Jül-3746
March 2000
ISSN 0944-2952